MAGNETOELECTRIC THIN FILM HETEROSTRUCTURES AND ELECTRIC FIELD MANIPULATION OF MAGNETIZATION

Yue Zhang

Thesis submitted to the faculty of the
Virginia Polytechnic Institute and State University
in partial fulfillment of the requirements for the degree of

Master of Science
In
Materials Science and Engineering

Dwight D. Viehland (Chair)
Jiefang Li
Alex O. Aning

April 28, 2015
Blacksburg, VA

Keywords: magnetoelectric, multiferroic, thin film, magnetostriction, piezoelectricitiy, magnetization, lead magnesium niobate-lead titanate, iron-gallium

MAGNETOELECTRIC THIN FILM HETEROSTRUCTURES AND ELECTRIC FIELD MANIPULATION OF MAGNETIZATION

Yue Zhang

ABSTRACT

The coupling of magnetic and electric order parameters, i.e., the magnetoelectric effect, has been widely studied for its intriguing physical principles and potentially broad industrial applications. The important interactions between ferroic orderings—ferromagnetism, ferroelectricity and ferroelasticity—will enable the manipulation of one order through the other in miniaturized materials, and in so doing stimulate emerging technologies such as spintronics, magnetic sensors, quantum electromagnets and information storage. By growing ferromagnetic-ferroelectric heterostructures that are able to magneto-electrically couple via interface elastic strain, the various challenges associated with the lack of single-phase multiferroic materials can be overcome and the magnetoelectric (ME) coupling effect can be substantially enhanced. Compared with magnetic field-controlled electric phenomena (i.e., the direct magnetoelectric coupling effect), the converse magnetoelectric effect (CME), whereby an electric field manipulates magnetization, is more exciting due to easier implementation and handling of electric fields or voltages. CME also affords the possibility of fabricating highly-efficient electric-write/magnetic-read memories.

This study involved two avenues of inquiry: (a) exploring the strain-mediated electric field manipulation of magnetization in ferroelectric-ferromagnetic heterostructures, and (b) investigating coupling and switching behaviors at the nanoscale. Accordingly,

a series of magnetoelectric heterostructures were prepared and characterized, and their electric field tunability of magnetic properties was explored by various techniques and custom-designed experiments. Firstly, the relevant properties of the individual components in the heterostructures were systematically investigated, including the piezoelectricity and ferroelectric/ferroelastic phase transformations of the ferroelectric substrates, lead magnesium niobate-lead titanate, or $Pb(Mg_{1/3}Nb_{2/3})O_3$-$PbTiO_3$ (PMN-PT). This investigation revealed significant information on the structure-property relationships in crystals oriented at <110>, as well as shed light on the effect of ferroelectric phase transformation on magnetoelectric coupling. This investigation of electric field controlled strain, in contrast to many prior studies, enables a more rational and detailed understanding of the magnetoelectric effect in complex ferroelectric-ferromagnetic heterostructures.

The magnetoelectric thin film heterostructures were fabricated by depositing ferromagnetic iron-gallium (Fe-Ga) or cobalt ferrite ($CoFe_2o_4$ or CFO) films on top of differently-oriented ferroelectric PMN-PT substrates. Through significant electric field-induced strain in the piezoelectric substrate, the magnetic remanence and coercive field, as well as the magnetization direction of the ferromagnetic overlayer, can be substantially tuned. These goals were achieved by the interfacial strain modification of the magnetic anisotropy energy profile. The observation and analysis of the electric field tunability of magnetization and the establishment of novel controlling schemes provide valuable directions for both theoretical development and future application endeavors.

ACKNOWLEDGEMENTS

I cannot express enough thanks to my advisors, Dr. Dwight D. Viehland and Dr. Jiefang Li, for providing this great learning opportunity and unwavering faith and encouragement during my master's research.

I would like to express my deepest gratitude and respect to Dr. Viehland, whose professional knowledge, research passion and great wisdom have inspired me throughout the course of my study. I have benefited enormously from his scientific attitude, inspiring discussions, and intelligent suggestions on my research. His patience and guidance on my paper writing and presentation preparation have been of great importance for my growth as a scientific researcher. The experience and advice he shared with me have become invaluable resources for my life.

I would also like to give my sincere appreciation to Dr. Li, without whose great support and insightful guidance my research would not have been accomplished. Her profound knowledge in materials science and rich experience in experimental methodology have been essential for my study and research.

My sincere gratitude also belongs to my committee member, Dr. Alex O. Aning, for his support, guidance and encouragement.

I would also like to thank Dr. Guo-Quan Lu, Dr. David Clark and all the faculty and staff in MSE for great help, advice and guidance.

In particular, I would like to thank Dr. Zhiguang Wang and Dr. Yaojin Wang, who have provided countless help and valuable discussions on my research. I would also like to thank Chengtao Luo, Yanxi Li and all the previous members in our research group for help in experiments and sharing of life experience.

Finally, I am especially grateful to my loving parents who have nurtured and supported me all my life. Their unconditional love is my momentum forever.

TABLE OF CONTENTS

LIST OF TABLES

LIST OF FIGURES

CHAPTER 1: INTRODUCTION

1.1 Multiferroic materials and magnetoelectric coupling effect

The ever-increasing volume of data generated by today's consumer electronics is linked to challenging demands for denser, faster and more reliable storage technologies with improved energy consumption. Contemporary memory technologies such as FeRAMs (ferroelectric random access memories) and MRAMs (magnetic random access memories) use polarization and magnetization to encode binary information, respectively. But FeRAMs suffer from slow readability due to destructive read operations and subsequent reset demands, and MRAMs are handicapped by elevated writing energy consumption due to the large magnetic field that is generated, which switches the magnetization states in the writing process. To overcome such limitations, coupling between ferroelectric and magnetic order parameters are highly desirable and could, in principle, permit data to be written electronically and read magnetically—thereby achieving high reading speed and reduced energy consumption simultaneously. Additionally, electronic devices such as laptops, smartphones and electromagnetic motors are considered high-impact inventions that continue to change the way we live. Despite ongoing advances, these devices could be further improved or even revolutionized through advances in multiferroic materials research. Such promising applications and the pursuit of multifunctionalities provide a foundation for improved multiferroic materials and heterostructures that take advantage of the strong correlation and coupling between ferroelectric and magnetic orders [1-2].

1.1.1 Multiferroic materials: definition, significance and historical aspects

Multiferroic materials, by definition, refer to a group of crystals where two or more of the primary ferroic properties (ferromagnetism, ferroelectricity, ferroelasticity, etc.) are united in the same phase [3]. This definition has been extended to multi-phase composites and also includes anti-ferroic forms of ordering. Among these, the most attractive and intensively studied interaction is the coupling between ferroelectric and (anti-) ferromagnetic order parameters—known as the magnetoelectric coupling effect [1-2, 4-7]. In ferroelectric materials, spontaneous and stable dielectric polarization exists even in the absence of external electric fields; moreover, polarization can be switched hysteretically by an electric field. Similarly, ferromagnetic materials possess spontaneous magnetization that can be reversed by a magnetic field, while ferroelasticity describes the spontaneous strain that is switchable by a given stress (Fig. 1.1). Whereas the ferroic property of a material is usually tuned by its conjugate field, multiferroic enables modification of the electric polarization by a magnetic field and/or manipulation of the magnetization by an electric field [8], which provide additional degrees of freedom in the tailoring of properties.

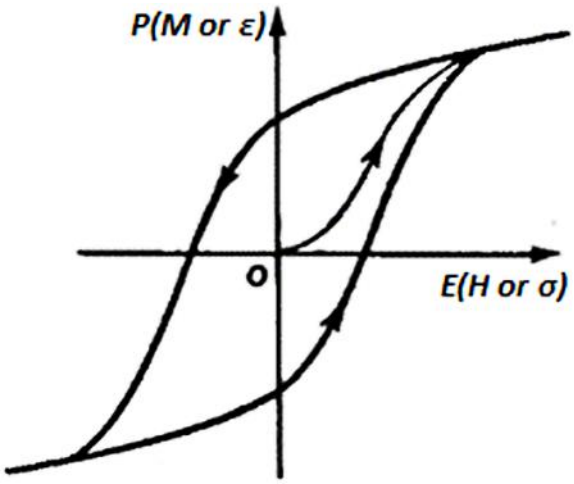

Figure 1.1 Spontaneous, switchable internal alignment (electric polarization *P*, magnetization *M* or strain *ε*) versus external stimuli (electric field *E*, magnetic field *H*, or stress field *σ*).

The fact that many ferroelectrics are also ferroelastic results in a coupled shape/dimension change when their electric polarization is changed. Moreover, the combination of ferroelectricity and ferroelasticity leads to so-called "piezoelectricity," which has important implications for a wide range of industrial products such as sonar detectors, actuators, sensors, etc. The corresponding coupling between magnetization and strain in ferromagnets results in magnetostriction, which can also be exploited in transducer applications such as magneto-mechanical actuators. Magnetoelectric (ME) coupling, on the other hand, focuses on the cross-coupled responses of electric and magnetic fields. Specifically, it refers to the induction or modification of polarization via a magnetic field (direct ME effect) or magnetization by an electric field (converse ME effect). These cross-coupled phenomena arise intrinsically from the interaction and coupling between charge, spin and the lattice order parameters, as shown in Fig. 1.2.

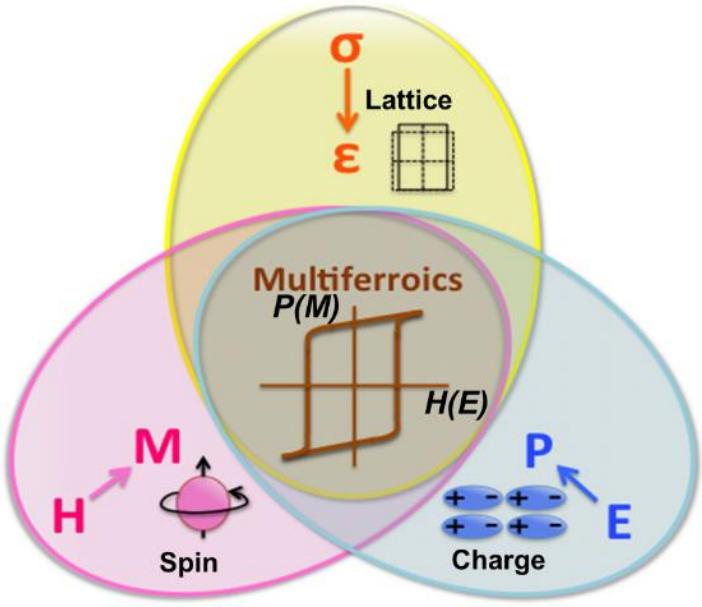

Figure 1.2 Schematic illustration of coupling of order parameters: piezoelectricity, magnetoelasticity and magnetoelectricity. Coupling between

electric and magnetic orders results in magnetoelectric materials and enables magnetic (electric) field manipulation of polarization (magnetization).

The quest to understand the interaction between magnetism and electricity has fascinated scientists, researchers and engineers alike for centuries; this search culminated in the 1860s when the famous Maxwell's equations unified the theory. Later in the nineteenth century, the existence of coupling between electric and magnetic fields in a solid was presumed by Pierre Curie[9], but was only substantiated in the second half of the twentieth century when Dzyaloshinskii and Moriya described the physical mechanisms of bilinear ME coupling (known as the Dzyaloshinskii-Moriya interaction)[10]. They predicted that single phase ME materials should exhibit ME coupling, whereby electrically-induced magnetization or magnetically-induced polarization exist. Shortly thereafter in 1960, the first experimental observation of ME coupling was achieved by Astrov in Cr_2O_3[11] and subsequently by Folen and Rado in 1961[12]. Other families of materials were successively discovered to possess linear ME coupling, including nickel-iodine boracide $Ni_3B_7O_{13}I$ reported by Hans Schmid in 1966[13], and some fluorides reported by Astrov and co-workers[14]. Despite the initial flurry of research interest, the field of ME effect basically languished and remained overshadowed by major solid state research for several decades. It was not until the beginning of the twenty-first century that the situation changed dramatically and ME coupling research was revitalized[2, 15]. This was in part stimulated by the discovery of large multiferroic properties in perovskite oxides $BiFeO_3$[16] and $TbMnO_3$[17], not to mention by the fabrication of improved experimental machinery and techniques to study the synthesis and performance of high quality samples.

The enthusiasm for multiferroic materials stems both from advances in the technical knowledge of the physical spin-charge ordering in these materials, as well as their potential application in pioneering devices. The theory and principles behind magnetoelectric multiferroics will be discussed in Section 1.1.2, including some important potential applications of these materials. The potential for the development of advanced technologies using multiferroics is virtually limitless, but primarily includes magnetic field sensors, electrically switchable permanent magnets, spin field effect transistors, microwave devices, and novel information storage technologies. Moreover, switchable electric polarization and magnetization are likely to be important for recording binary code. It should also be noted that the magnetic/electric field tunability of these ordering states presents even more opportunities to devise novel memory structures or improve the density and efficiency of existing ones.

1.1.2 Principles and prospects for magnetoelectric multiferroic

The linear coupling between electric and magnetic fields first suggested by Pierre Curie presents an immediate challenge to conform to the scalar transformation properties required of a free energy. Since electric fields break time-reversal symmetry, and magnetic fields break spatial-inversion symmetry, they can be coupled to first order via Maxwell's equations through the incorporation of time and spatial derivatives, which also have non-trivial transformation properties under time reversal and spatial inversion, respectively[18-19].

Magnetoelectricity is the cross-coupling between electric polarization and magnetism in a material. Specifically, it is the induction of magnetization with the application of

an electric field, or the induction of polarization with the application of a magnetic field. Some literature reports consider this coupling as a linear magnetoelectric effect, while others propose a more inclusive definition for magnetoelectric coupling to be any coupling between magnetic and electric order parameters. From an applications point of view, the real interest in multiferroic materials lies in the possibility of creating new functionalities in materials. The polarization and magnetism of the crystal may be remanent (as in magnetoelectric multiferroic) or field-induced, and the symmetry aspects are expressed in Fig.1.3[5].

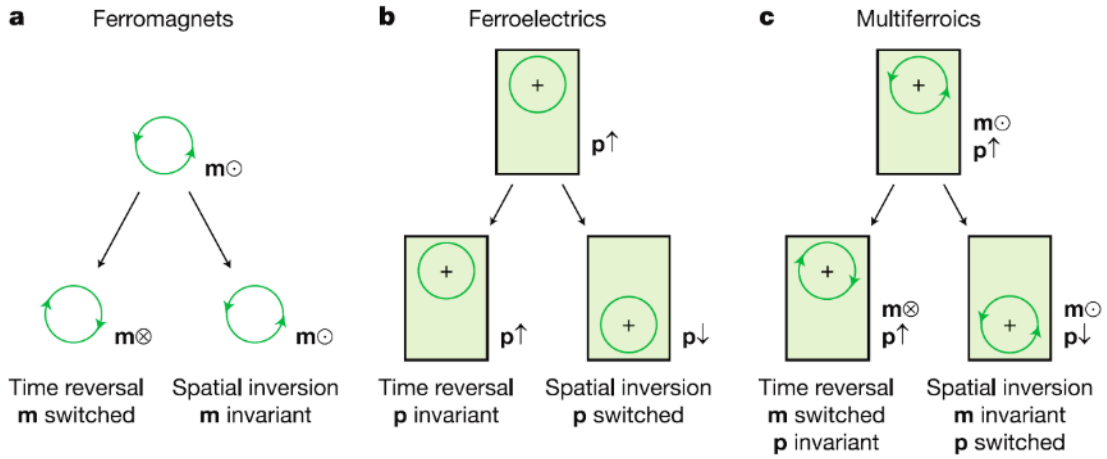

Figure 1.3 Time-reversal and spatial-inversion symmetry required of ferromagnets and ferroelectrics, respectively. In multiferroics, neither symmetry is preserved. ([5] Eerenstein, W.; Mathur, N. D.; Scott, J. F., Multiferroic and magnetoelectric materials. *Nature* 2006, *442* (7104), 759-765.) Used under fair use, 2015.

According to the Landau theory, the magnetoelectric effect is conventionally described by writing the free energy F of the system in terms of an applied magnetic field H and an electric field E. Since the magnetic field H and electric field E are vectors, the coupling parameters will be tensors in the most general expression.

Thermodynamically, by writing F under the Einstein summation convention, the following expression is derived:

$$-F(E,H) = \frac{1}{2}\varepsilon_0\varepsilon_{ij}E_iE_j + \frac{1}{2}\mu_0\mu_{ij}H_iH_j + \alpha_{ij}E_iH_j + \frac{1}{2}\beta_{ijk}E_iH_jH_k + \frac{1}{2}\gamma_{ijk}H_iE_jE_k + \frac{1}{6}\delta_{ijkl}E_iE_jH_kH_l \cdots \quad (1.1)$$

The first two terms on the right-hand side in equation (1.1) describe the contribution of electrical and magnetic responses to an electric field and a magnetic field, respectively. The third term in the free energy expansion describes the most-studied linear magnetoelectric coupling where α_{ij} denotes the linear magnetoelectric coefficient. The fourth and fifth terms contain the third-rank tensors β_{ijk} and γ_{ijk}, which represent the high-order linear-quadratic magnetoelectric coupling coefficients. In addition, the sixth term presented is the biquadratic coupling, which is allowed for all crystal symmetries and leads to greater magnetoelectric voltages than linear coupling. However, it is generally less common to find crystals that allow the other coupling terms where spatial inversion symmetry and/or time reversal symmetry need to be broken. Fortunately it was recognized that these other magnetoelectric coupling terms can be non-zero in crystals having certain transformation properties[20].

To obtain the expression for magnetically-induced polarization P and electrically-induced magnetization M, one needs to minimize the free energy by differentiating F with respect to E_i (H_i), and then setting E_i (H_i) to zero. These operations result in:

$$P_i = \alpha_{ij}H_j + \frac{1}{2}\beta_{ijk}H_iH_j + \cdots \quad (1.2)$$

$$\mu_0 M_i = \alpha_{ij} E_j + \frac{1}{2}\gamma_{ijk} E_j E_k + \cdots \quad (1.3)$$

In practice, ferroic properties are best described by resultant rather than applied fields; thus, the resultant electric and magnetic fields may be approximated by polarization and magnetization indicators, respectively. In terms of the unit, α_{ij} has dimensions of time divided by space, and is typically given by ps·m^{-1}. Additionally, magnetoelectric coupling is usually described in terms of magnetically-induced voltage (rather than magnetically-induced polarization), since voltage can be measured directly. Therefore, the corresponding unit of mV·Oe^{-1}·cm^{-1} is typically adopted. Note that linear magnetoelectric coupling coefficient α_{ij} is bounded by the geometric mean of the permittivity and permeability of the material, i.e., $\alpha^2 \leq \varepsilon\mu$ in simple notation. Therefore, a multiferroic that is both ferromagnetic and ferroelectric would probably deliver larger linear magnetoelectric coupling effect since ferromagnets and ferroelectrics often possess large permittivity and permeability values. Currently, the search for intrinsic linear magnetoelectric coupling is advancing steadily, but the most promising and commonly exploited coupling is the biquadratic (strain mediated) coupling because of its ubiquity and the lack of constraints on symmetry, as well as the size of the coupling.

1.1.3 Magnetoelectric effect in single phase materials

The number of candidate materials exhibiting multiferroic properties in a single phase is limited; moreover, their magnetoelectric effects are typically too small at room temperature to be applicable to device applications. Existing classes of single phase multiferroics cover several different materials categories and crystal structures,

including perovskite oxides, hexagonal manganites, orthorhombic fluorides, boracites, and others, as shown in Table 1.1[21-22]. However, the most versatile family is a group called perovskite oxides whose unit cell is shown in Fig. 1.4. With an ABO_3 structure that can accommodate nearly all elements of the periodic table, perovskite oxides exhibit a wide range of properties that are of interest to many functional applications, ranging from insulators, semiconductors, conductors, superconductors, ferroelectrics, ferrimagnets, (anti)ferromagnets, multiferroics to colossal magnetoresistance. Therefore, the preponderance of reports on multiferroics is concerned with oxides, or even perovskite oxides. While most multiferroic perovskites only exhibit multiferroicity at very low temperatures, the ferroelectric-antiferromagnetic $BiFeO_3$ is to date the only unambiguous room temperature, single-phase multiferroic material[23]. Nevertheless, $BiFeO_3$ is far from ideal—mostly because (a) its magnetization is too small, (b) its dielectric loss and leakage current are too large, and (c) the applied *H* does not significantly affect polarization. These shortcomings drive the ongoing quest to identify room temperature, single-phase multiferroic materials.

Table 1.1. Single-phase multiferroic materials and their electric/magnetic ordering types, as well as the transition temperatures. (A)FE, (A)FM, WFM represent (anti)ferroelectric, (anti)ferromagnetic and weak ferromagnetic, respectively.

Classes	**Material examples**	**Electric order**	**Magnetic order**	**T_C (K)**	**T_N (K)**
Relaxor	$Pb(Fe_{2/3}W_{1/3})O_3$	FE	AFM	178	363
	$Pb(Fe_{1/2}Nb_{1/2})O_3$	FE	AFM	387	143
	$Pb(Fe_{1/2}Ta_{1/2})O_3$	FE	AFM	233	180
Bismuth compound	$BiFeO_3$	FE	AFM	1103	643
	$BiMnO_3$	AFE	FM	450	100

Rare earth (RE) manganites (RE = Sc, Y, Tb, Ho-Lu)	$YMnO_3$	FE	AFM	913	80
	$YbMnO_3$	FE	AFM/WFM	983	87
$REMn_2O_5$ (RE = Y, Nd-Lu)	$TbMn_2O_5$	FE	AFM	25-39	45
Phosphates ($LiMPO_4$, M = Ni, Co, Fe, Mn)	$LiFePO_4$	FE	AFM/WFM	–	–
Boracites ($M_3B_7O_{13}X$, M = Ni, Cu, Cr, Mn, Fe, Co; X = Cl, Br, I)	$Ni_3B_7O_{13}I$	FE	AFM/WFM	62	62
Fluorides (BaMF4, M = Mg, Mn, Fe, Co, Ni, Zn)	$BaMnF_4$	FE	AFM/WFM	–	–
Spinel Chalcogenides	$ZnCr_2Se_4$	–	AFM	–	21
Delaffosite structure	$CuFeO_2$	–	AFM	–	–

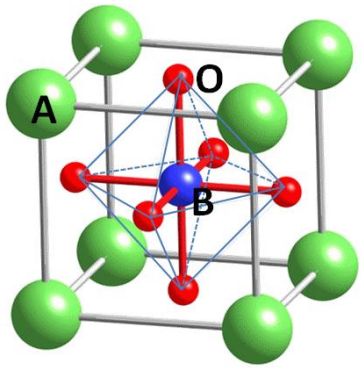

Figure 1.4. Schematic showing the unit cell structure of perovskite oxide ABO_3.

For perovskite oxides, the common mechanism for ferroelectricity is a non-centrosymmetric distortion caused by the off-centering of the B-site ion with an empty d-shell (e.g. transition metals Ti^{4+}, Zr^{4+}, Nb^{5+}, Ta^{5+}, W^{6+}). In contrast, for magnetic perovskites, the existence of magnetism requires B-site ions with a partially filled d-shell (for transition metals) or a f-shell (for rare-earth ions), such as V^{4+} (d^1), Cr^{3+} (d^3), Mn^{3+} (d^4), Fe^{3+} (d^5), since spins in completely filled shells sum to zero and do not participate in magnetic ordering[4]. This incompatibility of B-site ions in ferroelectric and magnetic perovskites was revealed by Hill[4] in explaining the scarcity of multiferroicity.

The incompatibility between traditional ferroelectricity and magnetism has, in turn, shed light on new routes to combine the two in a single phase. The most straightforward method to synthesize room temperature multiferroic materials is via the incorporation of two different cation types. By mixing d^0 and d^n ($n \neq 0$) B-site ions, $A(B_{1-x}B'_x)O_3$ structures are formed, which are expected to exhibit coexistence and coupling of ferroelectric and magnetic orders[24]. In addition, it is also known that the presence of easily polarized A-site ions (e.g. Pb^{2+}) favors the appearance of electric dipoles, making $Pb(B_{1-x}B'_x)O_3$ even more promising. Pioneering research in Russia[25] on such double perovskites did indeed show multiferroicity—for example in $Pb(Fe_{1/2}Nb_{1/2})O_3$ (PFN) and $Pb(Fe_{1/2}Ta_{1/2})O_3$ (PFT)—but the coupling between ferroelectric and magnetic orders tends to be very weak and exists only at very low temperatures, probably due to the dilution of the sublattices. Another more intriguing mechanism for multiferroicity relates to the fact that noncentrosymmetric magnetic ordering results in polarization, even if the atomic structure itself is centrosymmetric. This phenomenon was observed in $TbMnO_3$[17] and $TbMn_2O_5$[26], where the magnetoelectric coupling was shown to result from weak spin-orbit interactions[7, 27] or strong superexchanges[28-29], respectively. In addition, geometric ferroelectrics, in which layered anionic sublattice adopt unusual polar tilts and rotations, provide another route to mutiferroicity; related examples include rare-earth manganites[30-31] and barium nickel fluoride[32]. A different approach for tackling the incompatibility of the *d* orbitals rule is to exploit epitaxial strain as a knob to introduce desired properties[33].

Despite ongoing efforts and the continuous appearance of new magnetoelectric phenomena in single-phase materials, the research on single-phase multiferroicity tends to produce weak coupling (α being on the order of 1-20 $mV \cdot Oe^{-1} \cdot cm^{-1}$) and unacceptably challenging working conditions; in fact, some only detectable at extremely high magnetic fields and others only manifested as a minute change in electric/magnetic susceptibility at magnetic/electric transition temperatures (T_N, T_C). In a word, despite the fact that many single-phase ME materials have been explored and various kinds of interactions between electric and magnetic orders have been proposed, up to now no single-phase material has yet to be identified that has a measurable ME coefficient at room temperature and at low magnetic fields that meets application requirements.

1.1.4 Magnetoelectric effect in composite materials

Due to the contraindication between magnetism and ferroelectricity in single-phase multiferroics—where conventional mechanisms for cation off-centering in ferroelectrics (which requires formally empty d orbits) is incompatible with the formation of magnetic moments (which usually results from partially filled d orbits)—composite materials have been developed to overcome these limitations. The greater design flexibility for magnetoelectric multiferroics in composites has also benefited from the rapid development of synthesizing and characterization techniques, which enable the realization of various types of high quality composite architectures, and even *in-situ* control of the growth process. Multiferroic composites are usually synthesized by combining piezoelectric and magnetic substances together, where large piezoelectric and large magnetostrictive coefficient are desired and able to interact through the interface strain. The coupling between two such phases in

piezoelectric-magnetostrictive composites produces large magnetoelectric responses—usually orders of magnitude higher than in single-phase multiferroics at room temperature. Such strong couplings provide opportunities for the development of multifunctional devices such as magnetic sensors, transducers, etc.

The ME effect in composite multiferroics is a "product property" that results from the product of the magnetostrictive effect in the magnetic phase and the piezoelectric effect in the piezoelectric phase; it is mediated by the elastic interaction, as illustrated in the following general equations:

$$\mathrm{ME}_H \text{ effect} = \frac{\text{magnetic}}{\text{mechanical}} \times \frac{\text{mechanical}}{\text{electric}} \qquad (1.4)$$

$$\mathrm{ME}_E \text{ effect} = \frac{\text{electric}}{\text{mechanical}} \times \frac{\text{mechanical}}{\text{magnetic}} \qquad (1.5)$$

For the ME_H effect, a magnetic field induces a shape change in the magnetic phase via magnetostriction. The strain is then passed along to the intimately correlated piezoelectric phase, resulting in an electric polarization via the piezoelectric effect (Fig.1.5 (a)). The ME_E effect follows a similar coupling mechanism, even though an electric field is applied and provokes the inverse piezoelectric effect and, subsequently, the magnetostriction of the magnetic phase (Fig.1.5 (b)).

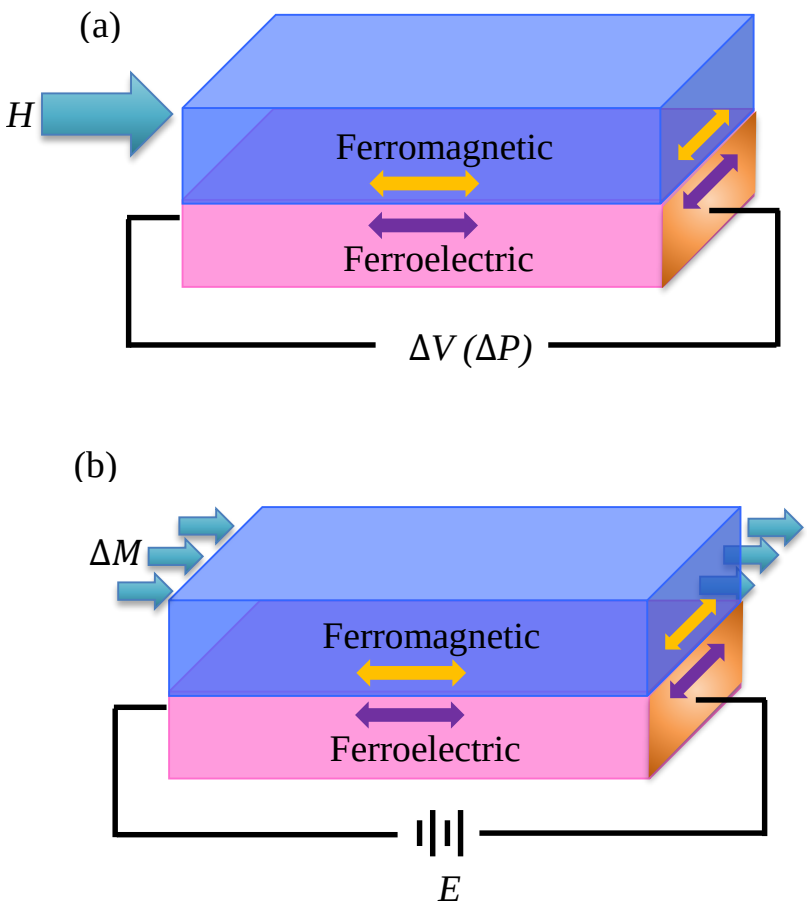

Figure 1.5. Magnetoelectric coupling in composite multiferroics comprising of a ferromagnetic and a ferroelectric phase. (a) An applied magnetic field induces a strain in the ferromagnetic phase and the strain is transferred to the ferroelectric phase, which results in a voltage output/polarization change. (b) A change in magnetization is induced by an electric field.

Unlike multiferroic phenomena in single-phase materials, the magnetoelectric coupling in composite multiferroics is extrinsic via strain mediation, and is dependent on the connectivity, microstructure and interface interactions of the piezoelectric and magnetic components. In recent years various ME composite systems have been developed and strong ME coupling responses have been observed above room temperature, which can be roughly divided into bulk ME composites and thin film

(nanostructured) ME composites. According to their connectivity of the respective phases, multiferroic composites can be classified into (0-3)-, (3-3)-, (2-2)- and (1-3)-type structures. For example, a (2-2)-type composite denotes a layer-by-layer structure and a (1-3)-type composite means one-phase pillars (denoted by 1) embedded in the matrix of another phase (denoted by 3).

In terms of the magnetoelectric coupling effect in bulk ME composites, the concept was proposed as early as 1972[34], but it was not until early 2000s that research into bulk ME composites experienced a tremendous upsurge[35]. In particular, laminate structures have proven to be the most successful design for obtaining accurate ME effect measurements, as well as sizable ME coefficient larger than 1 $V \cdot Oe^{-1} \cdot cm^{-1}$[36-40], where a thin layer of epoxy can be used to bond the constituents together. In terms of the types of constituents suitable for the ferroelectric and ferromagnetic phases in bulk ME composites, they can be generally categorized as ceramic ME composites, ceramic-alloy composites and polymer-based composites—the most representative examples of which include $Pb(Zr,Ti)O_3$ (PZT)/$NiFe_2O_4$ (NFO)[41], Terfenol-D/PMN-PT[42], and PZT-PVDF or Terfenal-D-PVDF[43].

Researchers continue to actively pursue device miniaturization and integration using ME composites in nanostructured thin films. Thus far, a great deal of different composite ME thin films have been investigated, where ferroelectric (e.g. BTO, PTO, PZT, PMN-PT, etc.) and magnetic (e.g. CFO, NFO, Fe_3O_4, LSMO, metals and alloys, etc.) phases are combined with different nanostructures (e.g. 0-3-, 2-2-, and 1-3-type heterostructures as shown in Fig. 1.6 [44]) via a wide range of synthesizing techniques (e.g. pulsed laser deposition or PLD, molecular beam epitaxy, sputtering, sol-gel, etc.).

Compared with bulk ME composites, thin film ME composites possess the advantages of atomic scale coupling and precise control of lattice matching, as well as more promising prospects for device applications. However, the main hurdle for this type of ME thin film is the substrate clamping effect, which must be overcome to enhance the ME coupling coefficients. One scheme is to eliminate the use of non-functional single-crystal substrates and substitute them with high-quality piezoelectric single crystal substrates, which not only act as a support for the thin-film heterostructures, but also serve as the electric field-induced strain mediation. The present work is based on this design, and details about the experiment and its implementation strategy will be discussed in the following chapters.

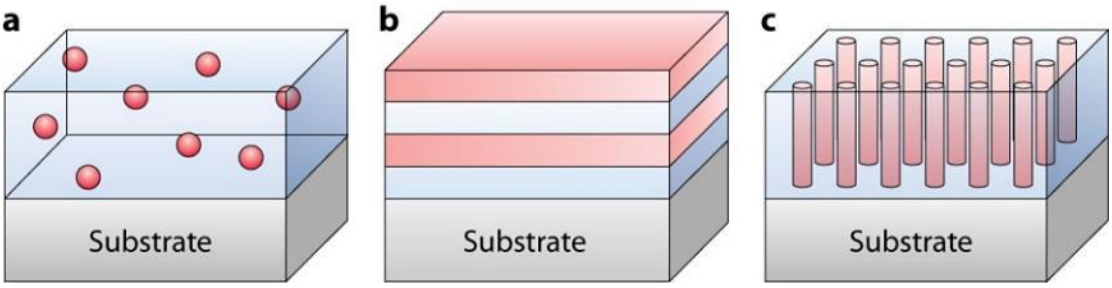

Figure 1.6. Schematic illustration of the three typical connectivity structures in ME thin films: (0-3)-type particulate films, (2-2)-type layered heterostructures and (1-3)-type vertical heterostructures. ([44] Wang, Y.; Hu, J.; Lin, Y.; Nan, C.-W., Multiferroic magnetoelectric composite nanostructures. *Npg Asia Materials* 2010, *2* (2), 61-68.) Used under fair use, 2015.

1.2 Materials studied in this thesis

1.2.1 Ferroelectric materials studied in this thesis –PMN-PT

Ferroelectricity describes the property of some materials that have a spontaneous electric polarization, which can be reversed by applying an external electric field. A crystal is said to be ferroelectric when it possesses at least two equilibrium orientations of the spontaneous polarization in the absence of an external electric field, and the spontaneous polarization can be switched between the orientations by an applied electric field. Parameters of importance here include coercive field (E_C), saturate polarization (P_S) and remanent polarization (P_r). Since the discovery of ferroelectricity, ferroelectric materials that have large piezoelectric and electrostrictive properties have been widely used in actuators, sensor and transducers. The perovskite ferroelectric $BaTiO_3$ was initially used in these applications, but was found to have insufficient magnitudes of the longitudinal piezoelectric (d_{33}) and electromechanical coupling (k_{33}) coefficients. In subsequent years, the piezoelectric ceramics $Pb(Zr,Ti)O_3$ (PZT) have enjoyed an almost total monopoly on transducer applications due to much higher d_{33} and k_{33} values that result from the proximity to a compositional morphotropic phase boundary (MPB). The MPB is an almost-temperature-independent phase boundary in the composition spectrum that separates tetragonal (P4mm) and rhombohedral (R3c) ferroelectric phases, where dielectric and piezoelectric anomalies are often observed. An alternative electromechanical material—namely, $Pb(Mg_{1/3}Nb_{2/3})O_3$ (PMN)—was developed in the late 1980s[45]. Although it provides a larger piezoelectric coefficient (d_{33}>800pC/N), it is limited in device applications due to its relatively low dielectric breakdown strength.

The most exciting breakthrough in high performance piezoelectric materials was the development of large $Pb(Mg_{1/3}Nb_{2/3})$-$xPbTiO_3$ (PMN-PT) and $Pb(Zn_{1/3}Nb_{2/3})$-$xPbTiO_3$ (PZN-PT) single crystals[46], which were reported to possess extreme

piezoelectric properties in the vicinity of MPB (d_{33}>2500pC/N, d_{15}>5000pC/N, k_{33}>94% and strain >1.7% for PMN-xPT ($0.30 \leq x \leq 0.33$) that was domain engineered[47-48]). The structural origin of the ultra-high electromechanical responses in relaxor-based ferroelectrics near the MPB has been intensively studied and several milestones were established: (i) the electric-induced ferroelectric phase transition from rhombohedral (R) to tetragonal (T) or R→T proposed by Park and Shrout[46]; (ii) the discovery of various bridging monoclinic phases[49-50]; (iii) the polarization rotation theory emphasized by Fu and Cohen[51]; and (iv) a theory of adaptive ferroelectric nanotwins[52-53]. Single crystal piezoelectric materials such as PMN-PT show significant reversible strain under an external electric field during the electrical polarization switching process, as shown in Fig.1.7. In many previous studies, single-crystal piezoelectric substrates have been used to grow magnetostrictive thin films on top, thus forming monolithic ME structures. The advantages of such ferromagnetic-ferroelectric heterostructures lie in the fact that during the electrical polarization switching process, the piezoelectric single-crystal experiences a reversible strain; this strain can then be transferred to the ferromagnetic thin film, where a magnetic strain anisotropy-controlled magnetic easy axis rotation will occur.

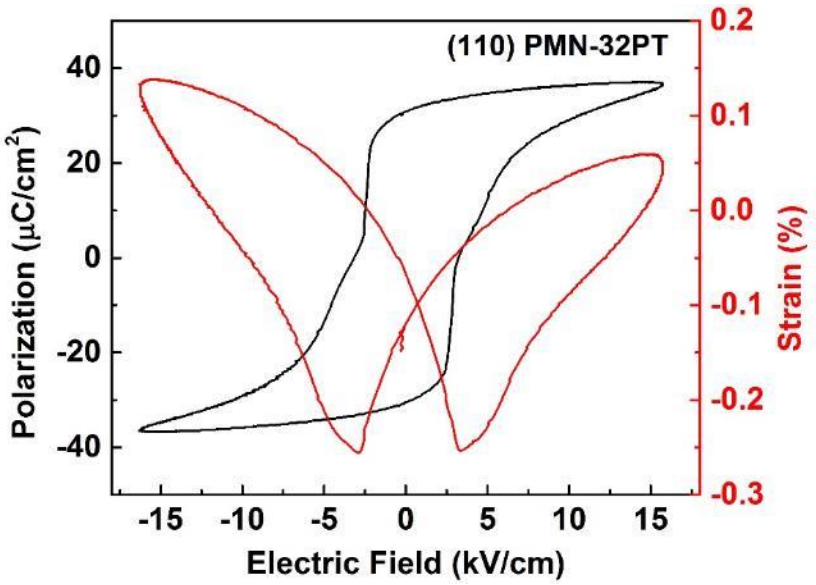

Figure 1.7. Typical electrical polarization hysteresis loop as a function of external electric field in piezoelectric single-crystal (black curve) and corresponding strain hysteresis loop as a function of electric field in the same single-crystal piezoelectric substrate (red curve).

1.2.2 Ferromagnetic materials studied in this thesis – Fe-Ga and $CoFe_2O_4$ (CFO)

The criterion for the occurrence of magnetism is quite different in comparison to those required for ferroelectricity. Whereas a ferroelectric requires off-center displacements of the ions, in a ferromagnet the constituent electrons must have a net angular momentum, either from the orbital component of the angular momentum, or the spin component, or both. As a strong driving force, the quantum-mechanical exchange energy leads to the parallel alignment of electron spins. Two phenomenological theories of ferromagnetism are recognized for successfully explaining many of the properties of ferromagnets: the Localized Moment Theory (LMT) of Curie and Weiss, and the Stoner Band Theory of ferromagnetism[54]. In LMT, local magnetic moments exist on the ions in the solid at all temperatures.

Below the Curie temperature the moments align to give a ferromagnetic state; above the Curie temperature they are disordered by thermal energy and there is no net magnetization, which is depicted in equation 1.6,

$$\chi = \frac{C}{T - T_C} \qquad (1.6)$$

where C is a material-specific Curie constant, T is absolute temperature, and T_C is the Curie temperature. The distinct feature of ferromagnetic materials is a spontaneous magnetization, M_s, that is stable, and that can be switched hysteretically by an applied magnetic field below the Curie temperatures T_C. Ferromagnetic materials adopt a domain structure where magnetic moments within the same domain align to the same direction and form a net magnetization. However, these domains orient randomly with respect to each other and the magnetization averages to zero for the entire ferromagnet in its initial state. Domains form so as to minimize the total energy of the material. However, when a magnetic field is applied to the ferromagnetic material, the domains will realign to the external field's axis and result in a net magnetization.

The magnetic domain responses to the applied magnetic field not only lead to the formation of a net magnetization, but also result in a shape/dimension change of the ferromagnetic material, which is referred to as magnetostriction. Specifically, when a magnetic field is applied, the boundaries between the domains shift and the domains rotate, both of which cause a change in the material's dimensions (Fig.1.8). Magnetostriction has it origin in a coupling between the direction of the spin moment of an atom and the orientation of its anistropically-shaped electron cloud—i.e., the spin-orbit coupling[55]. One can distinguish between volume (isotropic) and Joule (anisotropic) magnetostriction. In general, volume magnetostriction is far smaller than Joule magnetostriction (which was named after James Joule who first identified this

phenomenon in 1842), so the main concentration here is on Joule magnetostriction. Joule magnetostriction refers to the shape change of a ferromagnetic material increased with a change in magnetization. The value measured at magnetic saturation is called the saturation magnetostriction or λ_s. It can be quantified by the fractional change in length as the magnetization of the material increases from zero to the saturation value: $\lambda_s = \Delta l/l$, where l represents the sample length.

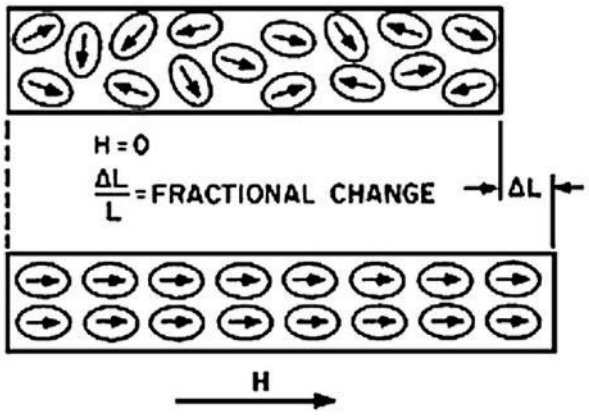

Figure 1.8. Magnetostrictive effect in ferromagnets. The realignment of ferromagnetic domains under external magnetic field results in elongation or shrinkage of the ferromagnetic material.

Although some degree of magnetostriction is observed in all ferromagnetic materials, those that exhibit large Joule magnetostriction at low field are of particular interest for use as acoustic sensors and generators, linear motors, actuators, damping devices, torque sensors, positioning devices, speakers, and microphones[56]. Magnetostriction, which is present in a range of different material categories, is especially important for specific engineering applications that rely on elemental metals such as cobalt, iron and nickel, oxides like ferrite, and alloys such as Terfenol-D ($Tb_xDy_{1-x}Fe_2$) and Metglas ($Fe_{81}Si_{3.5}B_{13.5}C_2$). The magnetostriction coefficient, λ, measured along

different crystallographic axis of a single crystal will vary; therefore, λ is anisotropic. For a polycrystalline, untexturized, cubic material, the saturation magnetostriction coefficient, $\lambda_{S,}$ can be written as:

$$\lambda_S = \frac{2}{5}\lambda_{100} + \frac{3}{5}\lambda_{111} \qquad (1.7)$$

The values of magnetostrictive coefficient of pure elements range from -34ppm for nickel to ~60ppm for cobalt, but a much higher magnetostrictive value is found in Terfenol-D, which exhibits over 2000ppm in a field of 2kOe at room temperature and is, therefore, the most commonly-used engineering magnetostrictive material. However, Terfenol-D alloys are brittle, require large fields for saturation, and are expensive due to the high costs of Tb and Dy. On the other hand, amorphous Metglass alloys require low fields for saturation, but also have a low saturation magnetostriction of about 30ppm.

Magnetostriction in Fe-Ga alloys

Since first developed by researchers associated with the Magnetic Materials Group at the Naval Surface Warfare Center (NSWC), Fe-Ga alloys have been a topic of ongoing interest due to a combination of their relatively large magnetostriction, low saturation fields, high mechanical strength, good ductility and low cost[57-61]. It has been reported that Fe-19%Ga alloys (i.e., galfenol) have a high magnetostriction of ~350 ppm at low coercive fields of ~100Oe near room temperature[62-63]. The saturation magnetostriction, $\lambda_{100,}$ is over tenfold compared to that of pure Fe (33ppm at room temperature[64]). The previously-investigated saturation magnetostriction (3/2) λ_{100} as a function of Ga concentration x is presented in Fig. 1.9(a)[58], where a maximum is reached at x~19% and a second peak appears at x~27%. The origin of such unusual magnetostrictive properties in Fe-xGa alloys was attributed to the

diversity of crystal phases and structural inhomogeneity introduced by the addition of Ga atoms to the bcc α-Fe phase. The maximum magnetostriction in Fe-Ga alloys occurs for x≈19at%, when a mixed-phase region of disordered body-centered-cubic α-Fe (A2) and $D0_3$ (ordered bcc) structures co-exists, which has been analogized to electrostriction of ferroelectrics near their morphotropic phase boundaries (MPB)[65]. Fig.1.9 (b) show the Fe-Ga phase diagram by Ikeda[66], as well as the different crystal structures for the various phases in the diagram.

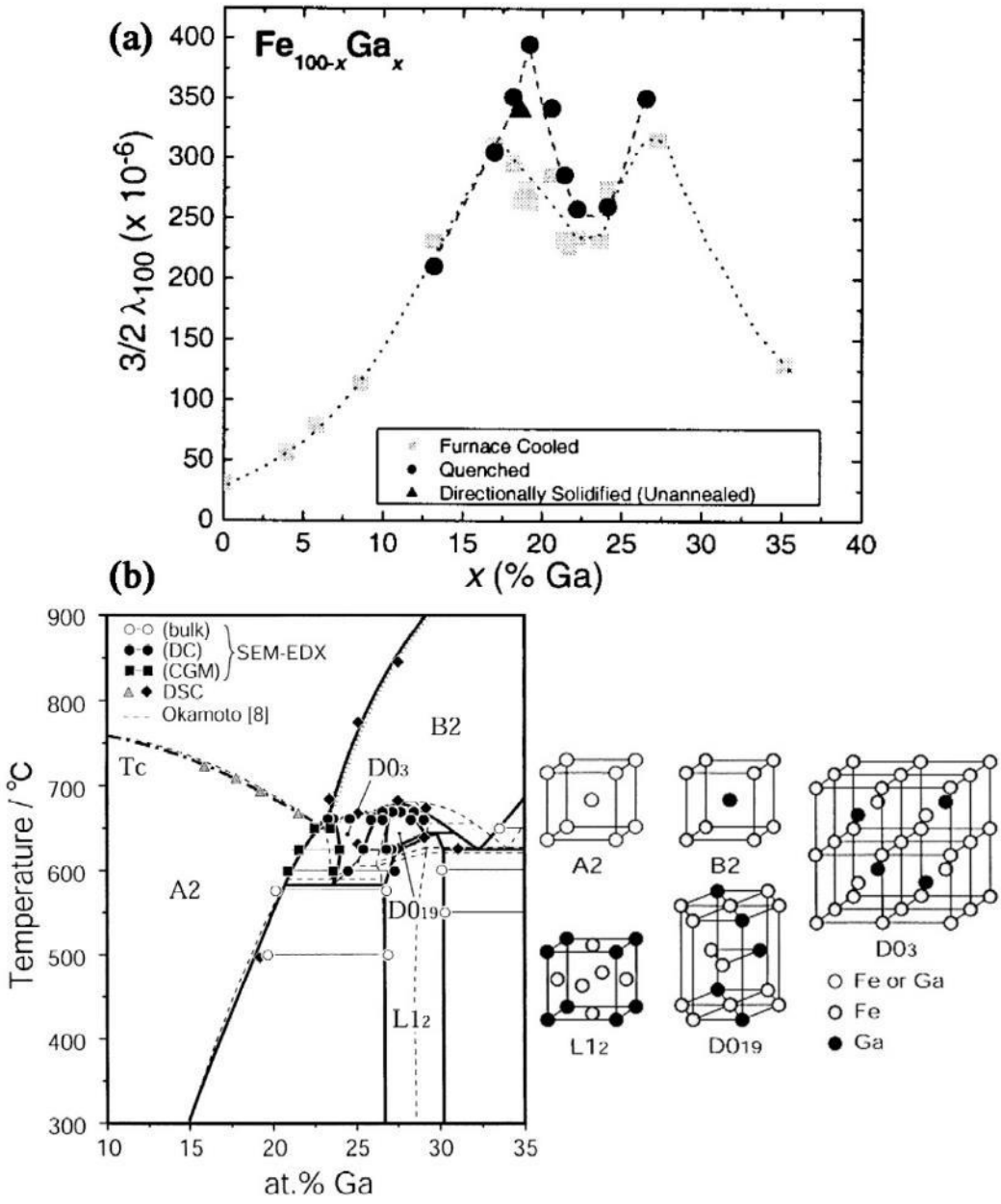

Figure 1.9. (a) Saturation magnetostriction (3/2) λ_{100} as a function of Ga concentration measured at room temperature. ([58] Clark, A. E.; Hathaway, K. B.; Wun-Fogle, M.; Restorff, J. B.; Lograsso, T. A.; Keppens, V. M.; Petculescu, G.; Taylor, R. A., Extraordinary magnetoelasticity and lattice softening in bcc Fe-Ga alloys. *Journal of Applied Physics* 2003, *93* (10), 8621-8623.) Used under fair use, 2015. (b) Phase diagram of Fe-Ga alloy and the crystal structures for phases of A2, B2, $D0_3$, $L1_2$, $D0_{19}$. ([66] Ikeda, O.; Kainuma, R.; Ohnuma, I.;

Fukamichi, K.; Ishida, K., Phase equilibria and stability of ordered b.c.c. phases in the Fe-rich portion of the Fe–Ga system. *Journal of Alloys and Compounds* 2002, *347* (1–2), 198-205.) Used under fair use, 2015.

Magnetostriction in $CoFe_2O_4$ (CFO)

Ferrites represent a well-established and important class of magnetic materials. They are typically comprised of mixed transition metal oxides and iron oxide. Spinel ferrite is a class of ferrite whose structure is derived from the mineral spinel (Fig.1.10); their physical properties are generally governed by the choice of the cations and their distribution between the tetrahedral and octahedral sites of the structure. The material of interest in our study—namely, cobalt ferrite ($CoFe_2O_4$)—belongs to the inverse spinel structural family. In this particular structure, the 32 divalent oxygen ions form a closed-packed FCC arrangement with 64 tetrahedral interstitial A sites and 32 octahedral B sites. Out of these, the divalent (Co^{2+}) and trivalent (Fe^{3+}) cations occupy one-eighth of A-sites and half of the B sites [67-68].

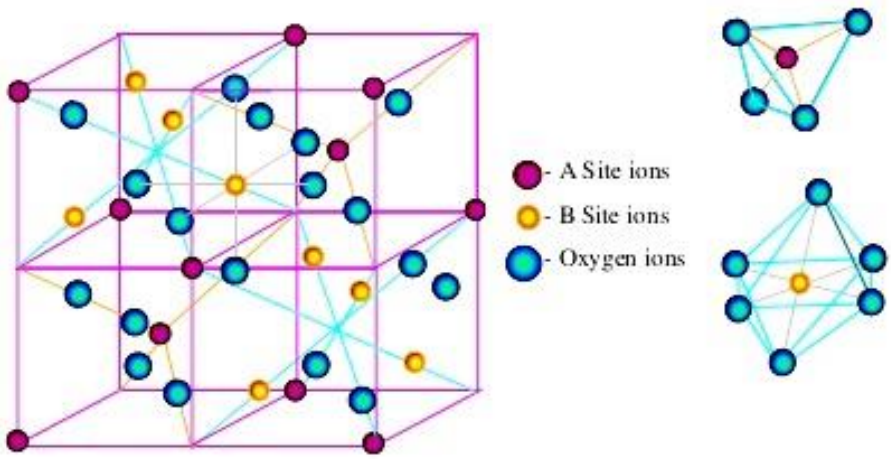

Figure 1.10. Crystal structure of spinel ferrite composed of tetrahedrally coordinated A-sites and octahedrally coordinated B-sites. ([68] Behera, C.;

Choudhary, R. N. P.; Das, P., Size effect on electrical and magnetic properties of mechanically alloyed CoFe2O4 nanoferrite. *J Mater Sci: Mater Electron* 2015, *26* (4), 2343-2356.) Used under fair use, 2015.

Among all the spinel ferrites known today, cobalt ferrite is of particular interest because of its relatively high saturation magnetization, excellent chemical stability, mechanical hardness, and high cubic magneto-crystalline anisotropy [69-73]. These properties make CFO a promising candidate for many applications in commercial electronics such as video, audiotapes, high-density digital recording media, and magnetic fluids [74-75]. The Curie temperature of CFO is 793 K, and it shows a relatively large magnetic hysteresis. The material parameters of CFO are summarized in Table 1.2 below (values reported in Ref. [76]).

Table 1.2. Material parameters of CFO: stiffness coefficient c_{ij} (GPa), magnetocystalline coefficients K_i (MJ/m^3), magnetostrictive constant λ (ppm), and saturation magnetization M_S (10^5 A/m). ([76] Hu, J.-M.; Nan, C. W., Electric-field-induced magnetic easy-axis reorientation in ferromagnetic/ferroelectric layered heterostructures. *Phys. Rev. B* 2009, *80* (22), 224416.) Used under fair use, 2015.

c_{11}	c_{12}	c_{44}	K_1	λ_{100}	λ_{110}	λ_{111}	λ_S	M_S
286	173	97	0.1	-590	-60	120	-110	3.5

1.3 Significance and objectives of this study

Magnetic and ferroelectric materials are of significant importance in modern science and technology. Ferromagnetic materials with switchable magnetization that are driven by an external magnetic field are increasingly indispensable in today's data-storage industries. Additionally, sensing industries rely heavily on ferroelectric materials with spontaneous polarization that is reversible upon application of an external electric field. Magnetoelectric (ME) multiferroic materials combine the favorable properties of ferromagnetism and ferroelectricity. In addition, they play essential roles in certain new phenomena such as magnetoelectric coupling effect, thus opening new possibilities for developments in modern electronic devices and intelligent systems.

As thin-film growth techniques and analytical tools progress, multiferroic thin films are becoming increasingly important in both fundamental and applied research—in part because high-quality thin-film materials possess many novel characteristics that exceed the capabilities of traditional bulk materials. Moreover, these films provide more freedom in tailoring material properties due to the interactive strain at thin film interfaces.

As reported in this thesis, the magnetic and ferroelectric materials of interest were thoroughly investigated and the different magnetoelectric thin film heterostructures were synthesized and analyzed—both from a fundamental physics perspective, as well as from an engineering technological standpoint. PMN-xPT crystals with compositions near the morphotropic phase boundary (MPB) were used as substrates for the fabrication of magnetoelectric heterostructures. Both the individual phase properties, as well as the magnetoelectric coupling phenomena of the ferroelectric-

ferromagnetic heterostructures, were explored in order to understand the physical principles underlying the coupling and provide insights for application possibilities. In addition, different ME-controlling schemes were proposed and investigated. Finally, careful assessment of their ME properties were undertaken using a variety of macroscopic and microscopic probes.

Specifically, the following goals were pursued in this investigation:

(1) To understand the relationship between phase transformations in ferroelectric substrates, i.e., PMN-PT and the corresponding strain transfer and ME effects in the ferromagnetic overlayer.

(2) To establish the relationship between microstructure and macroscopic behaviors, such as dielectric, piezoelectric properties and structural phase transitions in ferroelectric PMN-PT.

(3) To investigate ME coupling effects in ferromagnetic-ferroelectric Fe-Ga/PMN-PT and CFO/PMN-PT heterostructures and determine effective and strong E-field manipulation of magnetic orders.

(4) To propose novel implementation schemes for ME thin film heterostructures for the requirements of different potential applications.

CHAPTER 2: EXPERIMENT METHODS

2.1 Sample Preparation and Manufacturing Techniques

2.1.1 Polishing techniques

The PMN-PT crystals in this study required surface treatment prior to being used. Samples capable of delivering satisfactory experimental results generally have very smooth surfaces with a nanometer finish, or a specific surface termination according to different experiment requirements.

Fine polishing techniques

In order to prepare the PMN-PT substrates for thin film deposition, the surface of the PMN-PT had to be well polished with fine polishing techniques. The desired surface finish of these substrates had to be within nanometer range in order to ensure the conformal growth and epitaxial correlation of the deposited films.

The grinding-polishing method we utilized to reach ultrahigh smoothness relied on diamond lapping films and a soft cloth in the mechanical polishing (grinding) phase, and a vibratory polisher in the final chemo-mechanical polishing step. First of all, the PMN-PT sample being polished was mounted on a Pyrex wedge polishing stub with crystal bond adhesive or super glue, and then clamped on a Tripod polisher (Fig. 2.1), which can accurately perform level correction and thickness control of the sample.

Figure 2.1. Picture of Tripod Polisher® from South Bay Technology. (http://www.southbaytech.com/shop/590.shtml) Used under fair use, 2015.

Once the sample was mounted and level corrected, a Grinder-Polisher was used with a series of diamond lapping films to grind the sample. The tripod with the sample facing downwards was loaded on the spinning platen, and the water flow nozzle was adjusted to the vicinity of sample to flush out particles and debris. The process and expected results are summarized in the table below.

Table 2.1 Grinding steps before vibratory polishing and the expected results.

Step	Diamond lapping film grade (μm)	Platen speed (rpm)	Tripod push in distance (μm)	Expected results
1	15	50	−	Thinning and even removal of materials
2	6	40	30	Mirror-like surface with visible artifacts
3	3	30	20	Mirror-like surface with little artifacts
4	1	10	10	Mirror-like surface without artifacts

After these mechanical polishing steps, the sample surface was both flat and scratch free, reaching a smoothness of ~1μm. It was then further polished with a 0.05 μm soft

cloth in 50nm colloidal silica (SiO_2) suspension. The final step involved an eight-hour automatic polishing using a vibratory polisher, which was key to achieving nanometer finish surfaces (Fig. 2.2). Together with a napped cloth and non-crystallizing colloidal silica polishing suspension, the horizontal vibratory motion was able to remove any minor deformations remaining after mechanical polishing, leading to a stress-free surface. After these fine polishing steps, the surface smoothness of the PMN-PT samples was typically within a few nanometers or even better.

Figure 2.2. Picture of the vibratory polisher used for the eight-hour final polishing step. (https://shop.buehler.com/equipment/auxiliary-support-equipment/products/vibromet-2-vibratory-polisher) Used under fair use, 2015.

After fine polishing, the PMN-PT crystals were imaged using piezo-response force microscopy (PFM) and their surface topography and ferroelectric domains were simultaneously revealed.

Relief polishing techniques

Relaxor ferroelectric single crystals often exhibit exceptional electromechanical properties such as high piezoelectric coefficient, high dielectric constant, and improved capacity for high strain. Since Park and Shrout's seminal work in 1997 [46], research has suggested that the origins of these extraordinary electromechanical properties lie in the domain rotation via stress-induced phase changes. Among the various techniques employed to investigate the ferroelectric domain arrangements, piezo-response force microscopy (PFM), acid etching, and birefringence imaging are the most commonly used techniques due to their easy implementation and ability to provide detailed feedback information. In order to reveal surface domains in ferroelectric PMN-PT crystals, relief-polishing techniques were utilized. Relief polishing is a well-established technique in mineralogy and metallurgy for revealing grain boundaries or other microstructural details[77]. In terms of the PMN-PT crystals in our study, surface domains were preferentially removed according to their polarization orientation, resulting in an extremely flat surface with a topography matching the appearance of the domain structures.

The grinding and relief polishing were performed on a MiniMet® 1000 Grinder/Polisher. After mounting the PMN-PT crystal on an adjustable sample holder and finishing a preliminary polishing step using 600-grit sandpaper, the sample holder was mounted onto the polishing head and relief polishing was performed following the steps described in Table 2.2 below.

Table 2.2 Basic relief polishing steps for ferroelectric crystals performed in our lab.

	Process	Base	Abrasive	Grade (μm)	Speed (rpm)	Pressure (lb)	Time (min)
1	Lapping	Chem cloth	Diamond suspension	3	50	5	15
2	Polishing	Nylon cloth (synthetic napless cloth)	Diamond suspension	1	50	5	15
3	Fine polishing	Final finishing cloth (synthetic short nap cloth)	Colloidal silica	0.04	50	5	1

After relief polishing with colloidal silica, the sample surface was reduced to nanometer finishes. A final water rinse and ultrasonic cleaning step was needed to remove remaining polishing media and prevent colloidal silica particles from surface recrystallization. Figure 2.3 shows the AFM topography and phase images of a PMN-30PT sample after the three relief polishing steps described in Table 2.2; results showed that the average surface roughness of a 10μm× 10μm region was reduced from 8.14nm to 6.83nm and finally to 3.1nm. Figure 2.3 confirms that the surface pits and scratches visible in the first two steps were completely removed in the final step.

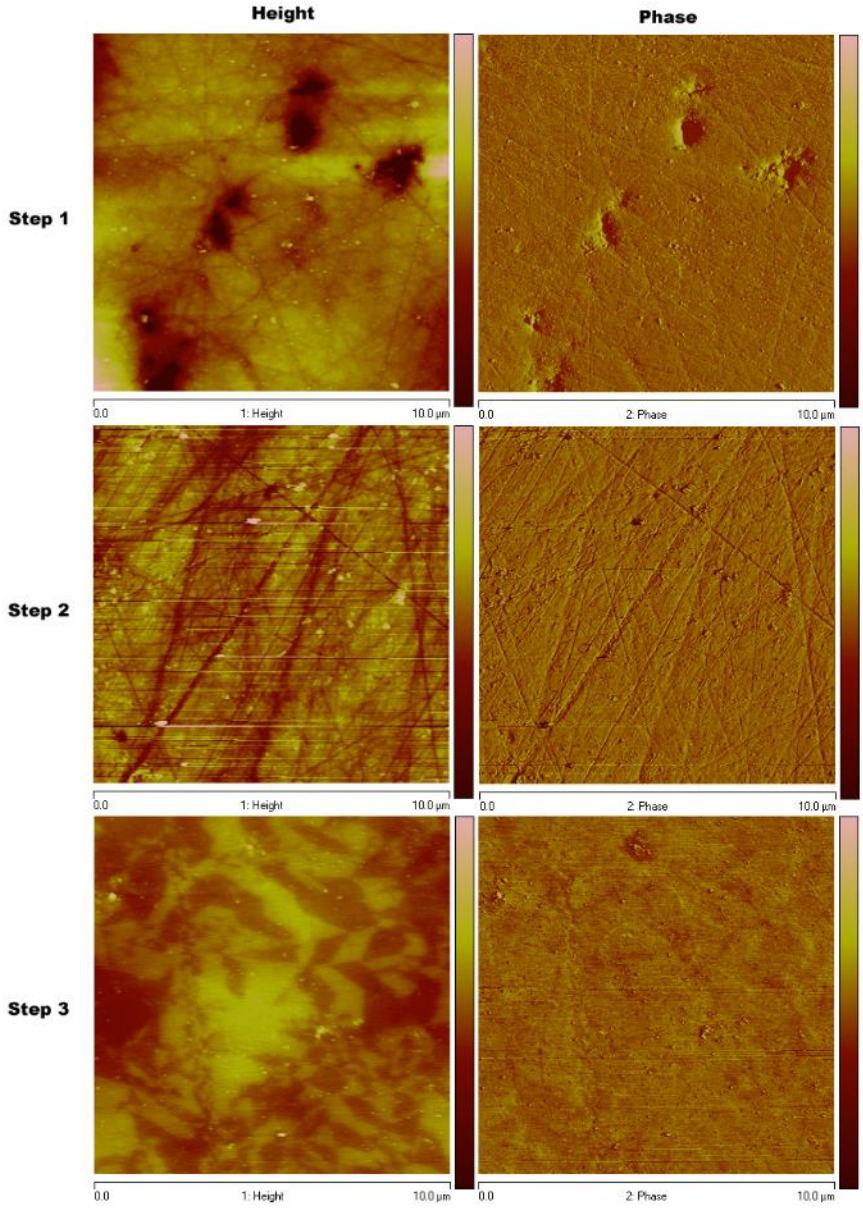

Figure 2.3. AFM topography and phase images of a PMN-30PT sample after each step of the relief polishing method. The imaging size is 10µm× 10µm.

2.1.2 Pulsed Laser Deposition (PLD) Technique

The magnetoelectric thin film samples in this study were fabricated using the pulsed laser deposition (PLD) technique. Pulsed laser deposition is a type of physical vapor deposition (PVD) that has been extensively used for thin film fabrication due to its

combination of stoichiometry transfer between target and substrate, as well as its versatile capability of depositing all kinds of materials in both ultrahigh vacuum (UHV), as well as ambient gas environment[78]. A basic set-up of PLD system is schematically shown in Fig. 2.4 (a).

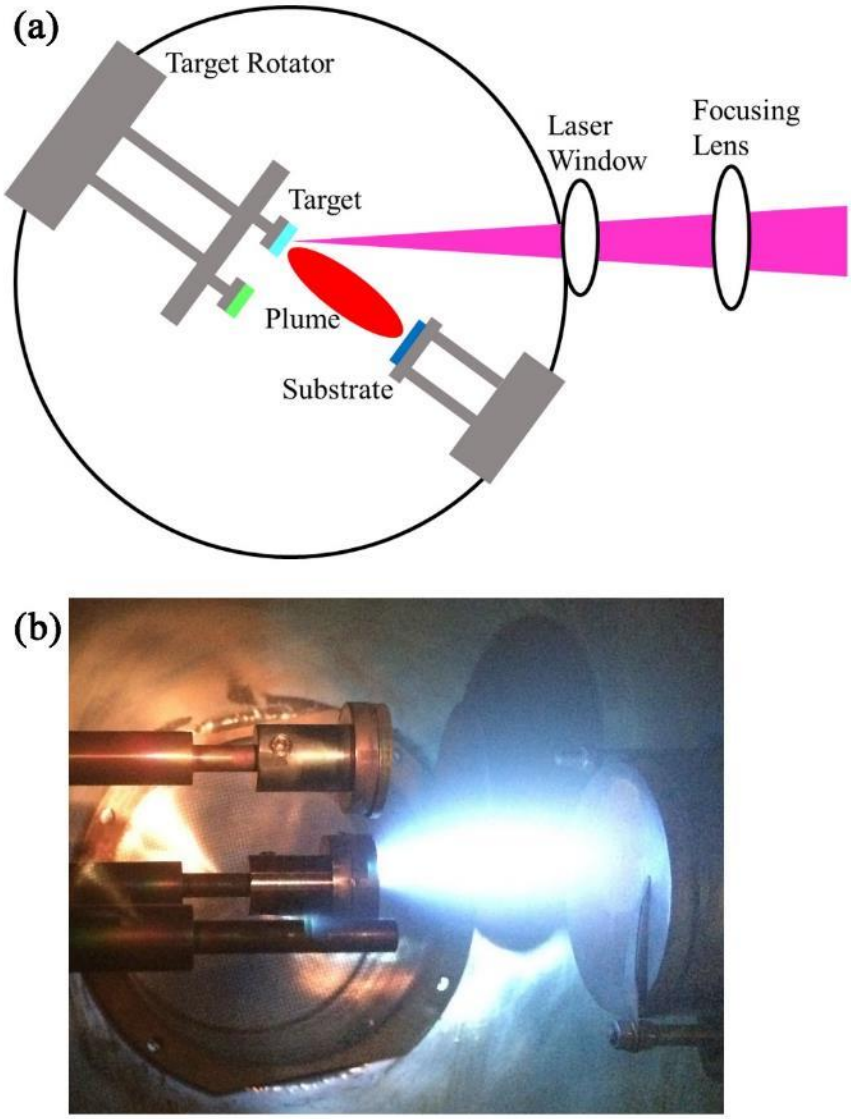

Figure 2.4. (a) Schematic diagram demonstrating the configuration of a basic PLD set-up. (b) Picture of a plume ejected from a $BiFeO_3$ target during pulsed laser deposition.

A PLD system typically includes a high-energy laser, a chamber and vacuum system, as well as target and substrate holders with a heating system. In our case, an excimer laser LPX305i (Lambda Physik) with KrF radiation was used. The wavelength of the laser was fixed to 248nm, and the pulse duration as 30ns. The energy and pulse frequency utilized were typically between 100mJ~500mJ and 1Hz~10Hz, respectively. While the basic setup was relatively simple compared to many other deposition techniques, the physical phenomena of laser-target interaction and film growth were quite complex. Specifically, a high-energy pulsed laser beam was focused inside the vacuum chamber, and a target deposited material was then struck by the pulsed and focused laser at an angle of 45°. This target material is essentially vaporized into atoms and ions and forms a plasma plume (Fig. 2.4. (b)), which is then deposited as a thin film on the substrate. The substrates are mostly attached to the surface parallel to the target surface at a target-to-substrate distance of typically 2-15cm. To summarize, the PLD mechanisms include the ablation process of the target material by laser irradiation, the development of a plasma plume with high energetic ions, electrons, as well as neutrals, and the crystalline growth of the film itself on the heated substrate.

For this investigation, the substrate was first attached on the substrate heater and settled in the sealed chamber. Then, a mechanical pump and a turbo pump connected to the chamber were turned on to pump the chamber down to a background vacuum pressure of 10^{-5}~10^{-6} Torr. The substrate was then heated to the designated temperature according to the heating program of the substrate heater. After the laser had warmed up, the chamber was filled with an oxygen atmosphere of 20~150 mTorr for the growth of oxide compounds. Next, the laser beam with desired energy and pulse frequency was directed and focused to the target through several lenses. The

target was rotated during the entire deposition process in order to obtain a steady ablation rate from the target. The laser-target interaction generated a plasma plume that delivered the target materials to the substrate, which then enabled the subsequent bombardment, condensation, interface bonding, nucleation and growth process of the ablated species on the substrate. Depending on the selection of target and substrate materials, as well as deposition parameters, epitaxial thin films can be grown on single-crystal substrates that have small lattice mismatch and consistent crystal orientations.

2.2 Characterization, Measurement and Analysis Techniques

2.2.1 X-ray diffraction (XRD) technique

X-ray diffraction (XRD) is the most commonly used technique to study crystal structure, symmetry and lattice parameters. In a crystalline material, the atoms and molecules can cause an incident X-ray with a fixed wavelength to diffract into many specific directions. The diffracted X-rays add constructively at certain directions, which is specifically related to the regular arrangement of atoms in the crystal. This X-ray diffraction phenomenon is governed by the famous Bragg's Law:

$$2d \sin\theta = n\lambda \qquad (2.1)$$

where d is the spacing between diffracting planes, θ is the incident angle, n is any integer, and λ is the wavelength of the beam. By measuring the angles and intensities of these diffracted beams, the structure of the crystal material can be determined. In this study, two sets of XRD systems—a PANalytical X'Pert Powder XRD and a Philips X'Pert high-resolution XRD—were utilized. The high-resolution XRD system was equipped with a two-bounce hybrid monochromator and an open three-circle

Eulerian cradle. The analyzer was a Ge (220) cut crystal with a 2θ-resolution of 0.0068°. The x-ray unit was operated at 45kV and 40mA with a wavelength of 1.5406Å (Cu Kα). During measurement, the sample can be tilted (Ψ) by ±90° or rotated (Φ) by 360° to find the corresponding crystal faces. Both line scans and mesh scans can be done to determine the epitaxial features of the thin films and extract structural information such as lattice parameters, stress of thin films and distortions of the crystals.

2.2.2 AFM, PFM and MFM techniques

The techniques described in this section all belong to a broader group of nanotechnology—namely, scanning probe microscopy (SPM). Invented in 1981, SPM technique with its versatile variants has become a most powerful tool for obtaining spatially-resolved information about the surface. In SPM, the image is formed by the interaction of a small physical probe with a solid surface. By changing the tip and set-up, a wide range of forces can be imaged in different scanning mode, including atomc force microscopy (AFM) mode, piezoresponse force microscopy (PFM) mode and magnetic force microscopy (MFM) mode. AFM is used to obtain topography information, whereas PFM and MFM are used to image and manipulate ferroelectric and ferromagnetic domains, respectively. The basic working principle of SPM follows that the small probe (tip) is raster scanned with respect to the sample, and the interaction is monitored. The spatial position of the monitored interaction is combined with the interaction information to construct a map of the probe-sample interactions.

AFM measurements

AFM was developed when researchers tried to extend the scanning tunneling microscopy (STM) technique to investigate electrically non-conductive materials[79-80]. An AFM can measure both long- and short-range interatomic and intermolecular forces between the sample and the tip. Some of the more common forces encountered in AFM include Van der Waals, capillary, electrostatic, friction and adhesion. Figure 2.5 depicts a simplified diagram of the basic AFM configuration. The basic components of an AFM include a cantilever, a probe tip, a piezoelectric scanner, a position sensitive photodetector and a feedback loop, all of which can easily be incorporated into one control electronics box, controlled by a computer.

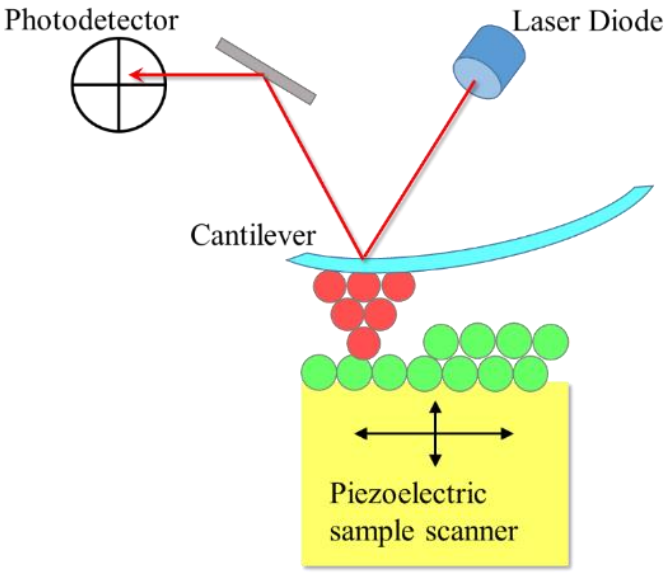

Figure 2.5. Simplified diagram of an AFM configuration.

A cantilever with a sharp tip at the end is used to detect the top surface of the sample. The cantilever is mounted at the end of a piezo-ceramic tube, which precisely controls the position of the tip (x, y). The piezo-tube has two sets of orthogonal electrodes. When an electric field is applied to the two sets of electrodes in the piezo-tube, the end of the tube is able to bend in the x or y direction. After careful calibration, the position of the tip (x, y) is able to be readout by the voltage applied to the piezo-tube.

During an AFM scan, the tip zigzags on top of the sample surface and the position is recorded in a data file. A laser beam is reflected by the backside of the cantilever to a position sensitive photo-detector. When the laser dot is in the middle of the photo-detector, the voltage output of the photo-detector is 0V; when the laser dot is off-center of the photodetector, the voltage output of the photo-detector is positive (+) or negative (-). When the tip is scanned on a smooth surface, the reflected laser dot is at the center of the photo-detector; if the tip encounters a small bump or pit, the end of the cantilever will bend up or down, consequently reflecting the laser spot up or down in the photo-detector. Therefore, the height (z) of the defection is able to be measured by a voltage output from the photo-detector. By combining the position (x, y) and the height (z) of the tip, a map of the top surface of the sample can be obtained.

In addition to height information, the phase information of the sample is equally important. In order for phase information to be extracted, the tip is driven at the resonance frequency. If the surface of the sample is uniform and flat, the vibration of the tip is constant and stable. If the tip encounters an uphill gradient or an elastically stiffer region, the vibration period of the tip is decreased. If the tip encounters a downhill slope or a softer material, the vibration period of the tip is correspondingly increased. The shift of the vibration period is given by phase. Because phase signals are sometimes stronger than height signals, phase maps of the top surface of a sample can provide important information.

There are three basic scanning modes for AFM: contact, tapping, and lift. In contact mode, the tip is always in direct contact with the surface of the sample, typically experiencing a predominantly repulsive force. The deflection of the cantilever is kept

constant and the contours of the surface are measured by the feedback signal required to keep the cantilever at a constant position. In this mode tips wear out quickly; moreover, the surface of the sample may also be damaged. However, through constant contact with the sample surface, the friction force between the tip and the sample can be obtained; the contact mode also enables samples to be imaged in a native fluid environment. Importantly, in AFM contact mode the tip can apply an electric field to the sample, which can be used to obtain PFM measurements. In the tapping mode, the tip is tapped on the sample surface at the resonance frequency, which eliminates fictional forces and prevents the tip from being trapped by adhesive forces. In this mode, the tip wears out more slowly, thereby providing high resolution images without the risk of damaging the sample surface. This is the most widely-used mode for studying sample topography. In the lift mode, the tip is lifted to about 10 to 100nm off the surface and a constant tip-sample distance is kept. While tips do not wear out in lift mode, the downside of this approach is that the resolution of the map is decreased. However, a magnetic cantilever can detect a magnetic signal in lift mode, thereby enabling an MFM image to be obtained.

PFM measurements

A basic vertical PFM measurement setup is shown in Fig. 2.6. PFM measurement works in piezo-response mode, which is based on contact. The bottom electrode of the sample is connected to the chuck, and the conductive tip is in contact with the top surface of the sample. When an electrical field is applied to the tip (top) or sample (bottom), the piezoelectric materials generate a strain. The tip responds to both the height and piezo-response signals that are induced by the applied AC electrical field. By using two internal lock-in amplifiers, which work at two different frequencies, the

height and piezo-response signals can be measured simultaneously. Also, by applying a DC electrical field to the top of sample, the polarization direction of the piezoelectric material can be switched. Similarly, lateral PFM results can be obtained by recording the rotation of the tip induced by the in-plane movement of the ferroelectric domains, instead of the height of the tip. In this way, one can map ferroelectric domains in the in-plane direction.

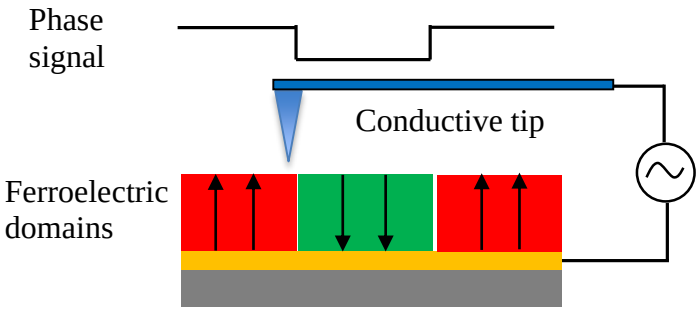

Figure 2.6. Schematic illustration of the basic setup and mechanism of a PFM.

MFM measurements

The MFM measurement technique is shown in Fig. 2.7. This approach works in an interleave mode, which means the tip initially scans the surface in tapping mode, after which it scans the same surface in lift mode. In tapping mode, the topography of the sample is recorded; in the lift mode, the topography information is subtracted from the data. Only the response of the magnetic tip to the magnetic signal is recorded in lift mode. If the magnetic tip is scanned over a magnetic material, the vibrational frequency of the tip will be changed due to the magnetic force between the tip and sample. Accordingly, the phase changes of the tip in lift mode reflect the magnetic signal of a given material. The phase map of the lift mode in interleave is used for MFM results.

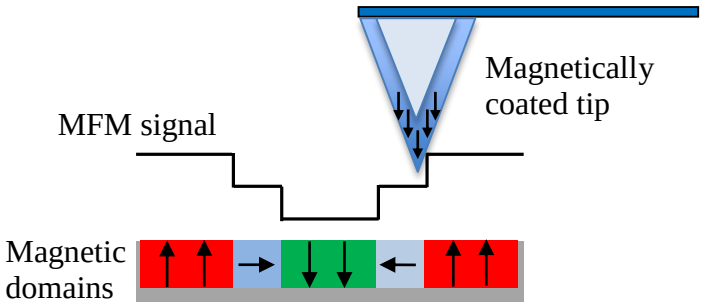

Figure 2.7. Schematic illustration of the MFM measurements.

2.2.3 SEM/EDS, TEM

A scanning electron microscope (SEM) produces images of a sample by scanning it with a focused beam of high-energy electrons. The electrons interact with atoms in the sample, generating various signals that can be detected and that contain information about the sample's surface topography and composition. The commonly used signals in SEM are secondary electrons and characteristic X-rays, which are capable of providing nanometer-resolution surface images and surface compositional analysis (EDS analysis), respectively.

The mechanism of a transmission electron microscopy (TEM) is quite different from that of a SEM, although the incident source is also a focused electron beam. In a TEM, a beam of electrons with very high energy is transmitted through ultra-thin specimens; the beam then interacts with the specimen as it passes through. An image of the specimen is formed from the transmitted electrons on a CCD array detector. Obtaining high-quality TEM images is heavily dependent on the quality of the

ultrathin specimen; therefore, ion milling and focused ion beam (FIB) are necessary for lifting out and revealing smaller regions of a sample.

2.2.4 Dielectric, piezoelectric and ferroelectric properties measurements

In this study, the dielectric, piezoelectric and ferroelectric properties of the samples were of primary interest. Therefore, we carefully measured these properties through the use of an impedance analyzer (HP4192A), a Sinocera d_{33} METER (S5865), a custom-built strain/polarization gauge, and a thin film polarization measurement setup based on the Sawer-Tower circuit. The impedance analyzer (HP4192A) was equipped with a temperature chamber and electric bias components, which we used to measure the temperature and the E-field dependence of the relative permittivity. Ferroelectric properties were measured using a polarization measurement setup based on a Sawer-Tower circuit, including a signal generator, a voltage amplifier, an oscilloscope and a reference capacitor, as shown in Fig. 2.8. AC voltage was cycled by the signal generator and its direction was reversed at high frequency. The voltage across the reference capacitor was then measured. As noted, the capacitance of the reference capacitor was about 100 times larger than that of the thin films. However, the charge on the reference capacitor must be the same as the charge over the ferroelectric film, since they are in series. This relationship means that the charge on the ferroelectric can be determined by the following equation: $Q=C\times V$, where C is the capacitance of the reference capacitor, and V is the voltage measured over this capacitor. Therefore, we were able to determine the polarization of our materials in an oscillating electric field by plotting the voltage applied to the material on the x-axis of the oscilloscope, and the surface charge on the y-axis. This was possible because the capacitance of the

reference capacitor is much higher than the capacitance of the ferroelectric; thus, most of the voltage lies over the ferroelectric.

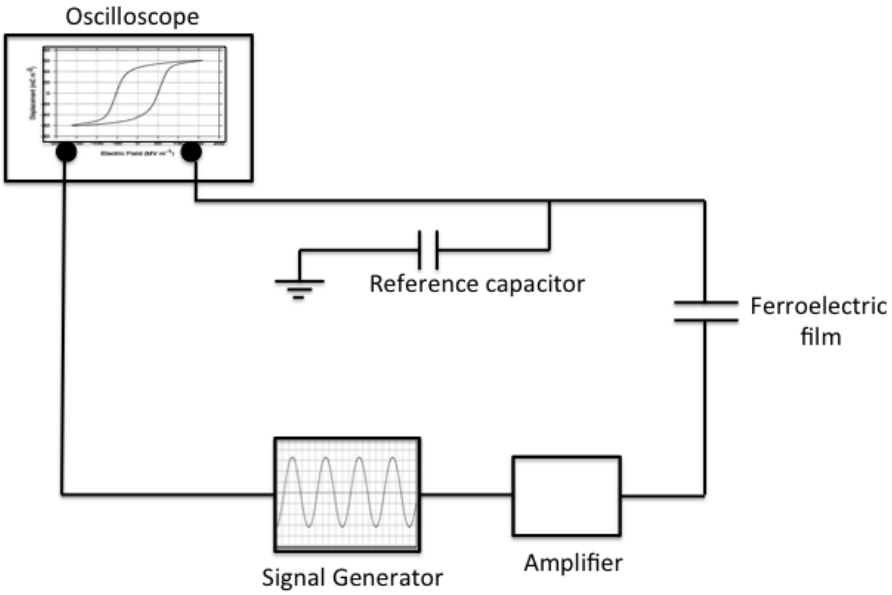

Figure 2.8. Schematic illustration of the dielectric polarization measurement set-up based on the Sawyer-Tower circuit.

2.2.5 Magnetic properties measurements

A vibrating sample magnetometer measures the magnetic moment of a sample when it is vibrated perpendicularly to a uniform magnetizing field[81]. In this study, the magnetic properties were measured using a Lakeshore 7300 VSM at room temperature. The basic setup and detection mechanism of the VSM is illustrated in Fig. 2.9 below.

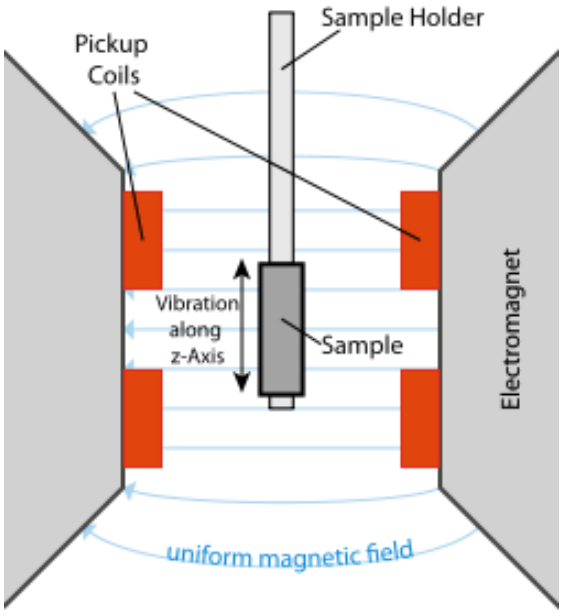

Figure 2.9 Schematic illustration of the VSM setup and mechanism.

Each of our samples was placed inside a uniform magnetic field generated by the electromagnets. It was then vibrated sinusoidally at certain amplitudes and frequencies—typically through the use of a piezoelectric material. The vibration induced a magnetic flux change through the sample, which subsequently resulted in a voltage in the pick-up coils. The induced voltage in the pickup coil was observed to be proportional to the sample's magnetic moment, but was not dependent on the strength of the applied magnetic field. In a typical VSM setup, the induced voltage is measured through the use of a lock-in amplifier, with the piezoelectric signal serving as its reference signal. The magnetic moment measured by the VSM can be related to the magnetization of the sample.

CHAPTER 3: STUDIES OF THE FERROELECTRIC PHASE OF PMN-PT IN MULTIFERROIC HETEROSTRUCTURES

3.1 Overview

Emerging electronic designs based on voltage-control of strain-sensitive order parameters have been shown to exhibit a wide variety of intriguing phenomena and higher energy efficiencies, including voltage-tuning of electronic states (i.e., "mottronics"[82]), and voltage modulation of magnetic states (i.e., the converse magnetoelectric effect [83-86]). Magnetoelectric coupling between magnetic and electric properties exhibits many intriguing phenomena and has potential for use in a wide variety of industrial applications. For example, single-phase ME materials only exhibit very weak coupling effects. In contrast, ME composites comprised of ferromagnetic and ferroelectric subsystems provide much stronger coupling and additional degrees of freedom in the control of polarization or magnetization through ferroelastic strain at the interface. The use of single-crystal piezoelectric materials as substrates for growing magnetostrictive thin films eliminates the clamping effect from the non-functioning paraelectric substrates. Their use also enables large ME effects, as well as viable controlling schemes due to the large electromechanical strain generated when subjected to an electric field. A great deal of prior research into the magnetoelectric effect in composite heterostructures have employed epitaxial strain imposed by a substrate as a kind of knob for tuning the electrical and magnetic properties of overlaying films, such as $La_{0.67}Sr_{0.33}MnO_3/BaTiO_3$ [87], $La_{0.7}A_{0.3}MnO_3$/PMN-PT(001) (A=Sr,Ca) [88], $Sr_2CrReO_6/BaTiO_3$ [89], Ni/(011)(PMN-PT) [90], $CoFe_2O_4$/(011)PMN-PT [85], and Fe-Ga/(011)PMN-PT [91] heterostructures. These studies have revealed significant applications potential,

including electric-write magnetic memory and electric field tunable microwave devices.

In such complex ferromagnetic/ferroelectric systems, the manipulation of film properties are realized through the epitaxial growth of functional films on piezoelectric/ferroelectric substrates, whose lattice parameters experience noticeable changes during polarization reorientations or phase transitions caused by an electric field. A number of researchers have utilized a phenomenological approach to calculate strain-induced magnetic easy-axis reorientation in various ferromagnetic thin films under electrical fields along different directions [76, 92-93]. Their predictions suggest the possible application of a strain-mediated ME random access memory with ultra-high storage capacity. However, the electric field-induced strain in ferroelectric materials involves complex physical processes where polarization rotation and reorientation coexist. Whereas the linear piezoelectric strains are only tunable in modest electric-field ranges, non-180° domain reorientations and polarization rotations (i.e., monoclinic phase transitions) can induce significant changes in crystal lattice parameters, thereby inducing a large strain. Additionally, considering the efficiency of strain transfer between ferromagnetic thin films and piezoelectric substrates, one should note that only in-plane strain can be effectively transferred—not the out-of-plane component. In view of these characteristics, some piezoelectric substrates (e.g., (001) PMN-30PT) are only capable of providing a large longitudinal piezoelectric response and a small reversible in-plane strain under E-fields. However, other piezoelectric substrates such as $BaTiO_3$ generate a sufficiently large, but irrecoverable (one-time), strain effect that cannot be reversed by E-field alone. In contrast, (011)-oriented $Pb(Mg_{1/3}Nb_{2/3})O_3$-x at%$PbTiO_3$ (PMN-xPT, $x \approx 0.3$)

single crystals are more interesting due to their large transverse piezoelectric response that enables larger converse ME effects in comparison to the aforementioned crystals[94]. More importantly, recent reports have shown the possibility of inducing both volatile and non-volatile strains in (011)-PMN-PT, which can be repeatedly addressed by electric field[95].

3.2 Structure and phase transition sequences of PMN-PT crystals

X-ray diffraction and neutron scattering studies have confirmed strong associations of $PbTiO_3$ content with the initial phase configuration and spontaneous polarization (P_S) directions of PMN-xPT solid solution systems at room temperature [96]. For PMN-xPT with low $PbTiO_3$ content ($x<0.3$), the stable phase is a rhombohedral (R) phase with P_S aligned along <111> directions. A complex phase mixture of monoclinic (M)—coexisting with rhombohedral (R), tetragonal (T) and/or orthorhombic (O) phases—was identfied for $0.3<x<0.38$, which is in the morphotropic phase boundary (MPB) range. Higher $PbTiO_3$ content ($x>0.38$) leads to stable tetragonal phase with P_S along the <001> direction (Fig.3.1 (a)). In other words, the spontaneous polarization direction can be tailored by the amount of $PbTiO_3$ content. In addition, phase transformation and polarization direction rotation in PMN-PT crystals are closely related to E-field and temperature histories (Fig.3.1 (b)).

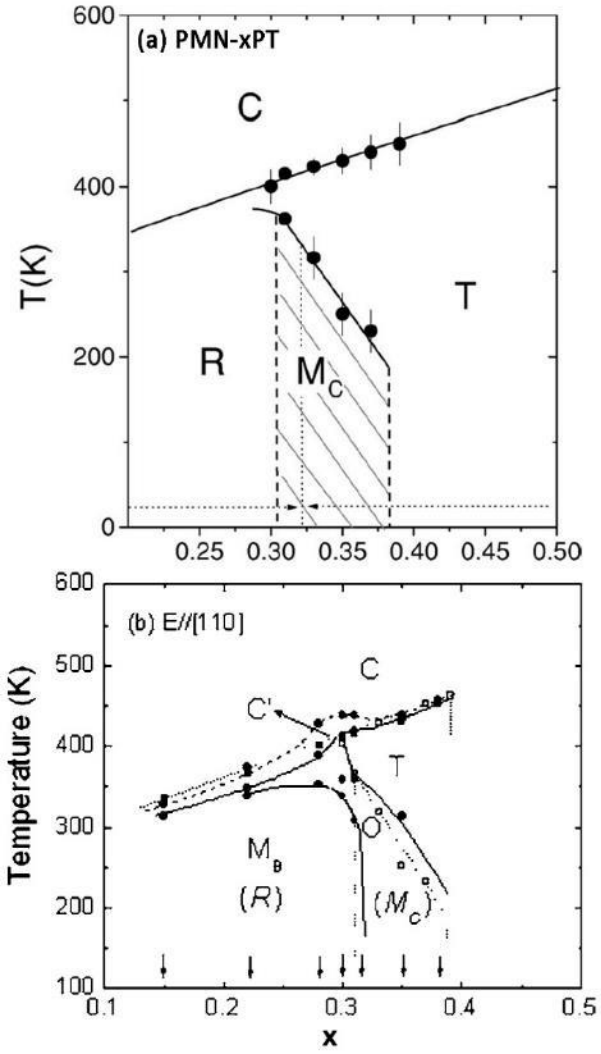

Figure 3.1. (a) Modified phase diagram of PMN-xPT around the MPB. ([96] Noheda, B.; Cox, D. E.; Shirane, G.; Gao, J.; Ye, Z. G., Phase diagram of the ferroelectric relaxor (1-x)PbMg1/3Nb2/3O3-xPbTiO3. *Physical Review B* 2002, *66* (5).) Used under fair use, 2015. (b) Modified phase diagram of [110] electric-field-cooled PMN-xPT crystals. ([97] Cao, H.; Li, J. F.; Viehland, D.; Xu, G. Y., Fragile phase stability in (1-x)PbMg1/3Nb2/3O3-xPbTiO3 crystals: A comparison of 001 and 110 field-cooled phase diagrams. *Physical Review B* 2006, *73* (18).) Used under fair use, 2015.

Specifically, for (011)-oriented PMN-30%PT crystals, the initial unpoled phase is rhombohedral with eight equivalent polarization directions (8R), which then evolves to monoclinic B (M_B) with two ($2M_B$) domain states upon application of an out-of-plane electric field E along [011]—and with further increase of E—to a mono-domain O (1O) phase. This R → M_B → O phase transition sequence has been widely recognized and confirmed by dielectric, piezoelectric, and structural measurements [98-100]. However, recent results show that the electrically-induced strain due to polarization rotation can be volatile or nonvolatile, given that the intermediate M and O phases have different stabilities on removal of E for crystals with different compositions [95, 101], as shown in Fig. 3.2 below.

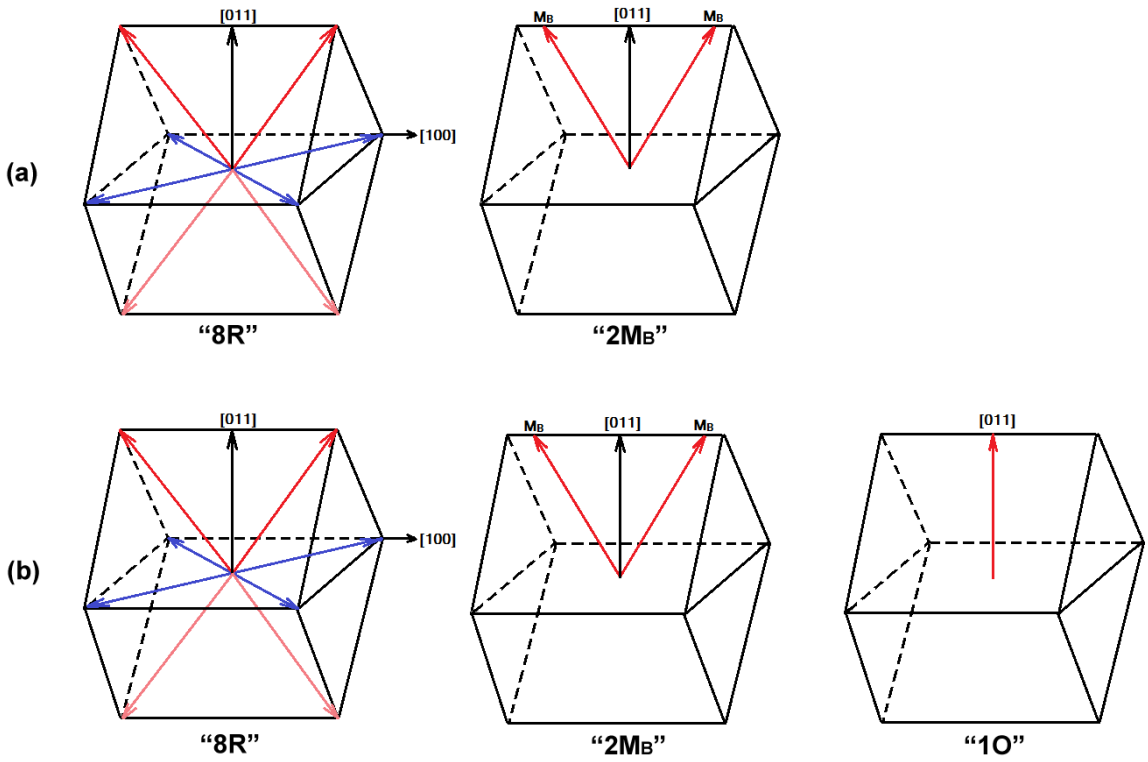

Figure 3.2. Schematic illustration of the phase transition sequence for two types of (011)-oriented PMN-xPT (x ≈ 30%) after electric poling along [011]. (a) E_p//[011] only induces an R → M_B transition; (b) E_p//[011] induces an R → M_B →

O phase transitions. All the diagrams depict the phase condition after removal of the poling field.

Figure 3.2 shows the proposed phase variants after electric field poling along the [011] direction for two types of PMN-PT whose compositions are close to the MPB from the rhombohedral (R) side. The fact that the different phase transition behaviors belong to the two ends of the same PMN-PT piece indicates the phase sensitivity to compositional fluctuations during the crystal growing process. The different stabilities of the E-field induced O phase—i.e., one type of PMN-PT relaxes back to M_B after the removal of poling field E//[011] (Fig. 3.2 (a)), and the other type remains at the O phase after removal of E (Fig.3.2 (b))—has been carefully investigated. Moreover, the relationship of this O-phase stability with crystal composition, initial phase configurations and microstructures has been thoroughly studied.

3.3 Dielectric and piezoelectric properties of PMN-PT crystals

Due to their markedly high piezoelectric properties (k_{33}~94%, d_{33}~2500 pC/N, ε~1.7%) in comparison to conventional piezoelectric ceramics such as $Pb(Zr,Ti)O_3$ (PZT), PMN-PT crystals have been used in a variety of applications such as ultrasonic transducers and strain actuators. More importantly, in the field of magnetoelectric heterostructures, research has targeted the large electrically-induced strain in PMN-xPT, which is an essential handle for tuning the magnetic properties of the magnetostrictive films grown on top. In particular, heterostructures on (011)-oriented PMN-PT substrates have shown both reversible- and irreversible-induced transformations, offering volatile and non-volatile electric-field controlling schemes.

To obtain insights into the different phase transformation behaviors under electric fields, investigations have looked at the dielectric, piezoelectric and strain properties of the two types of (011)-oriented PMN-PT crystals cut from the two ends of the same piece.

Firstly, the temperature dependence of the relative permittivity[102] upon poled heating and zero-field cooling processes for both types of (011)-PMN-PT single crystals were measured (Fig.3.3). The crystals were all poled under 10 kV/cm prior to beginning the measurements upon heating, after which the zero-field cooling response was obtained after two hours of in-situ annealing. In the poled heating curves of the (011)-PMN-PT crystals that had a stable induced M_B phase (hereafter denoted as "type I") (Fig.3.3 (a)), the temperatures of the two small peaks in the relative permittivity corresponded to the $M_B \rightarrow O$ and $O \rightarrow T$ transitions, respectively; and the large peak at 141 ℃ corresponded to the transition to the cubic (C) phase. For crystals featuring a metastable O phase (hereafter denoted type II), the temperature dependence of ε_r during heating from the poled condition (Fig. 3.3 (b)) revealed that the monodomain O state remained stable between 20 ℃ and 80 ℃, and subsequently underwent an $O \rightarrow T$ transition at the first peak (near 80℃), and finally a $T \rightarrow C$ transition near the dielectric maximum. Figure 3.3 (c) shows the ε_r curve for both types of crystals taken upon zero field cooling. By comparisons, we can find that type II crystals may have had a slightly higher $PbTiO_3$ (PT) content than type I crystals, as its $T \rightarrow C$ transition was slightly higher. This means it is closer to the vicinity of the MPB, and thus may have a stronger tendency to have monoclinic and orthorhombic phases coexisting with a primary rhombohedral phase.

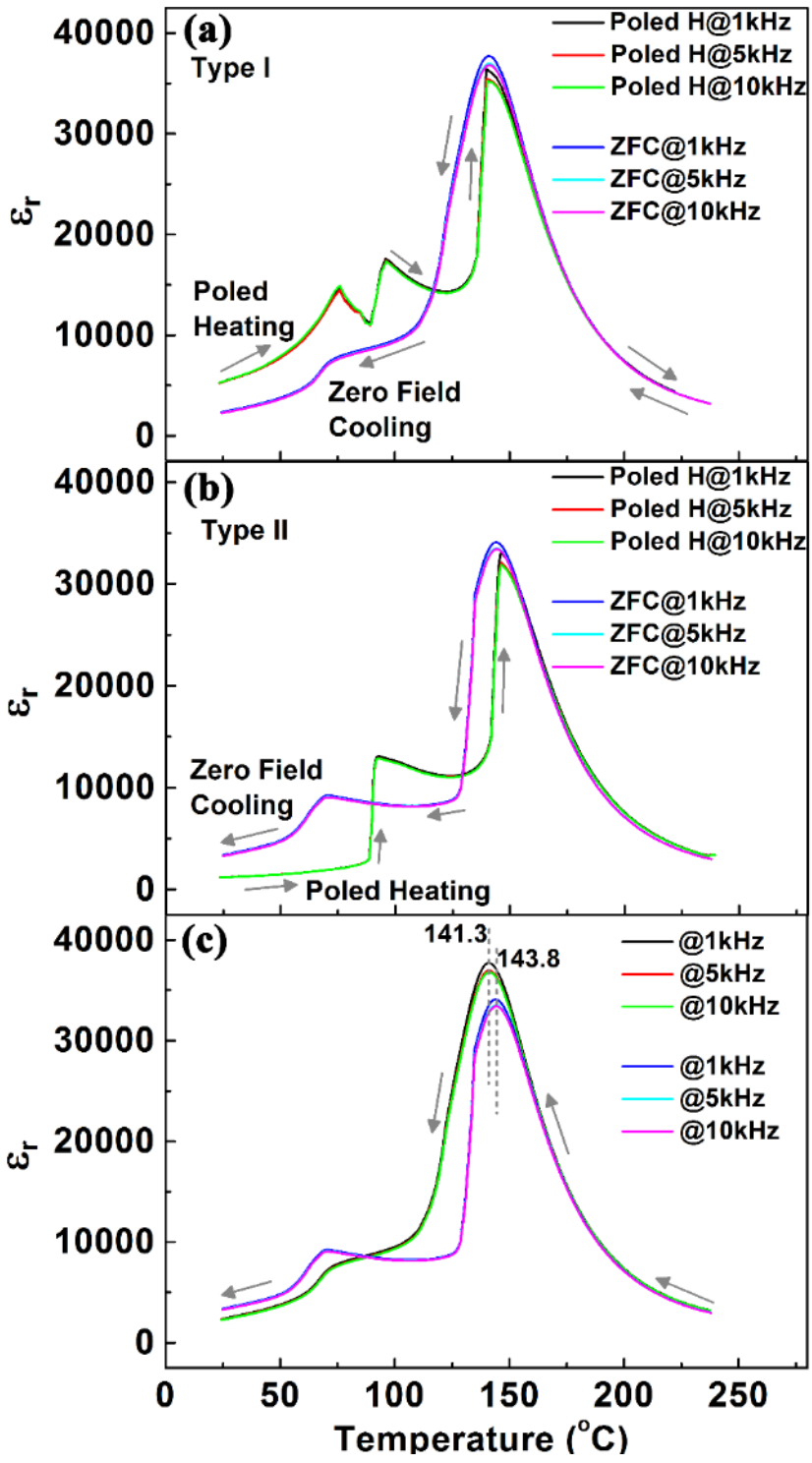

Figure 3.3 Temperature dependence of relative permittivity for (a) (011)-PMN-30PT without a metastable electrically-induced O-phase upon removal of E-field; (b) (011)-PMN-30PT with a metastable electrically-induced O-phase upon removal of the poling electric field and (c) comparison of the ε_r curves for the above two types of (011)-PMN-30PT upon zero field cooling process.

Next, the longitudinal piezoelectric coefficients (d_{33}) of two types of (011)-PMN-xPT ($x \approx 30\%$) crystals were measured at room temperature (Fig. 3.4). The PMN-PT crystals were first poled at room temperature along [011] with increasing poling fields E_p//[011] before measurement of d_{33}. Our results are consistent with the sequence of phase changes as illustrated in Fig. 3.2, where either stable M_B (Fig.3.2 (a)) or O (Fig.3.2 (b)) phases exist after E-field poling. Differences are evident between these two stable phases in the d_{33}-E_p plots. In the initial (unpoled) state, d_{33}=0. This reflects a nearly equal distribution of domain states (polarizations) amongst all possible 8R directions in the rhombohedral phase. After poling under E_p=1.5 kV/cm, a sharp increase of d_{33} was observed for both types of PMN-PT crystals. This increase was due to an $R \rightarrow M_B$ phase transition induced by the poling field. However, subsequent increases of E_p resulted in drastically different situations for the two types of PMN-PT crystals. For (011)-PMN-PT crystals that had a stable induced M_B phase (type I), no further changes in d_{33} ($\approx$ 1100 pC/N) occurred with increasing E_p (Fig.3.4 (a)). In contrast, for crystals that had a metastable O phase (type II), the value of d_{33} decreased markedly ($d_{33} \approx$ 280 pC/N) for $E_p \geq$ 3 kV/cm (Fig.3.4 (b)). A monodomain O phase can be induced for PMN-30%PT crystals under a sufficiently high E//[011]. For type I crystals, the polydomain M_B phase can be recovered on removal of E_p from the monodomain O one. The much higher value of d_{33} is due to the rotation of the polarization in the plane between (111) and (110) in the M_B phase. For type II crystals, the metastable O phase retained its polarization vector being parallel to [011]. This resulted in a significantly lower d_{33} value for $E_p \geq$ 3 kV/cm, which is typical of a single domain orthorhombic phase [100, 103].

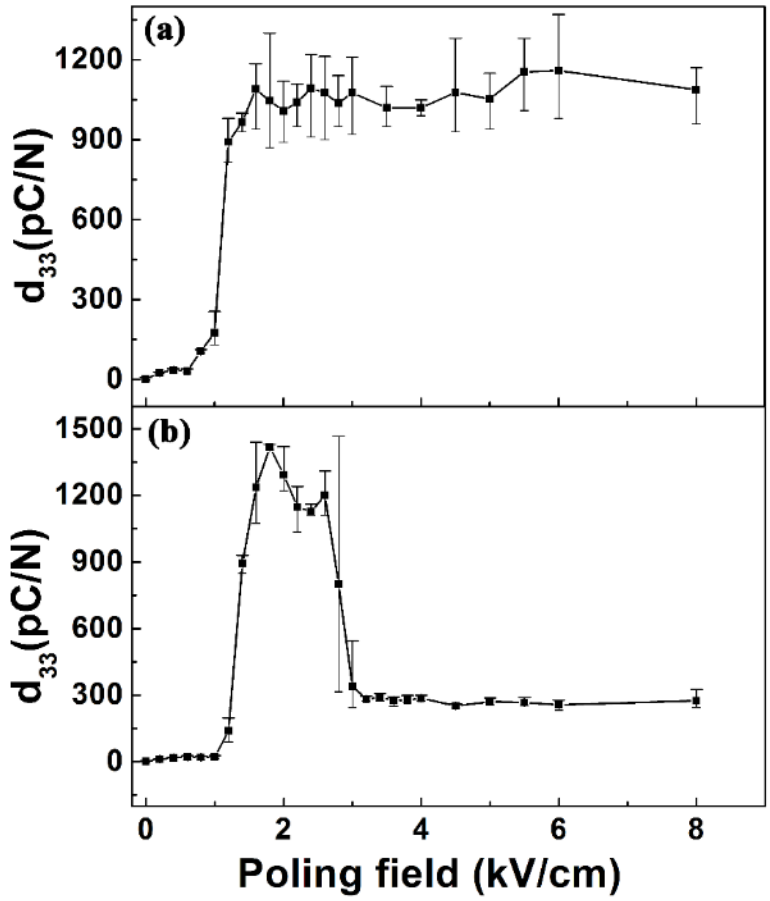

Figure 3.4. Longitudinal piezoelectric coefficient (d_{33}) as a function of poling electric field for (a) (011)-PMN-30PT without an electrically-induced O phase upon removal of E-field, and (b) (011)-PMN-30PT with a metastable O phase upon removal of poling electric field. The PMN-PT single crystals were first poled with the designated electric field and the poling field was removed at each time of measurement.

3.4 PFM investigation of PMN-PT domain structures

In this investigatory phase, piezoresponse force microscopy (PFM) was used to study the domain structures of (011)-oriented PMN-PT crystals with both volatile and non-volatile induced R → O transitions at room temperature. In order to understand the metastability of the induced orthorhombic phase, a correlation between the complex

domain structures and macroscopic properties was undertaken. As facilitated by PFM, a conductive tip working in contact mode detects the piezoelectric oscillations of ferroelectric materials under an AC driving field applied between the conductive tip and the bottom electrode. The oscillations of the sample under the conductive tip are detected with a lock-in amplifier. The amplitude of the measured feedback signal is proportional to the effective longitudinal piezoelectric coefficient in the vertical PFM mode (VPFM), while the phase signal reflects the orientation of the out-of-plane component of the polarization vector.

Figure 3.5 shows height and piezoresponse phase images of a 20 μm scan size for both types of PMN-PT crystals, revealing anisotropic domain morphologies. These crystals are in their initial annealed condition before poling, which corresponds to the E_p=0 kV/cm condition in Fig.3.4. In both cases, domains with conversely-oriented polarizations are distinguished by a different contrast on the piezoresponse phase images. In Figure 3.5 (b), piezoresponse phase mapping of the type I PMN-PT crystals exhibited long and thin domain striations—except the area interrupted by surface deformations, which featured a regular domain pattern and straight domain walls. Figure 3.5 (d) shows a 20 μm PFM phase image of a type II PMN-PT crystal, in which irregular and labyrinth domain structures are evident where the domain boundaries are curved and overlapping. Panels (e) and (f) represent sectional analyses of the PFM phase signals taken from the white lines indicated in the images (b) and (d), respectively. These sectional analyses were taken perpendicular to the elongation directions of the domain patterns in order to better reveal the actual domain structures and provide a more reasonable comparison. Well-defined ferroelectric domains with opposite polarization orientations in the out-of-plane direction can be seen in their

annealed conditions. The distribution of the domain spacing for type I crystals was quite narrow, showing an average size of ~0.6 μm with a standard deviation of ~0.15 μm. This uniformity distinguished itself from that of type II crystals, whose average domain spacing was about 1.1 μm with a standard deviation of ~0.51 μm. Clearly, there are significant and important differences in the domain distributions and morphologies in the (011)-PMN-30%PT crystals between those that with and without metastable O phases after poling.

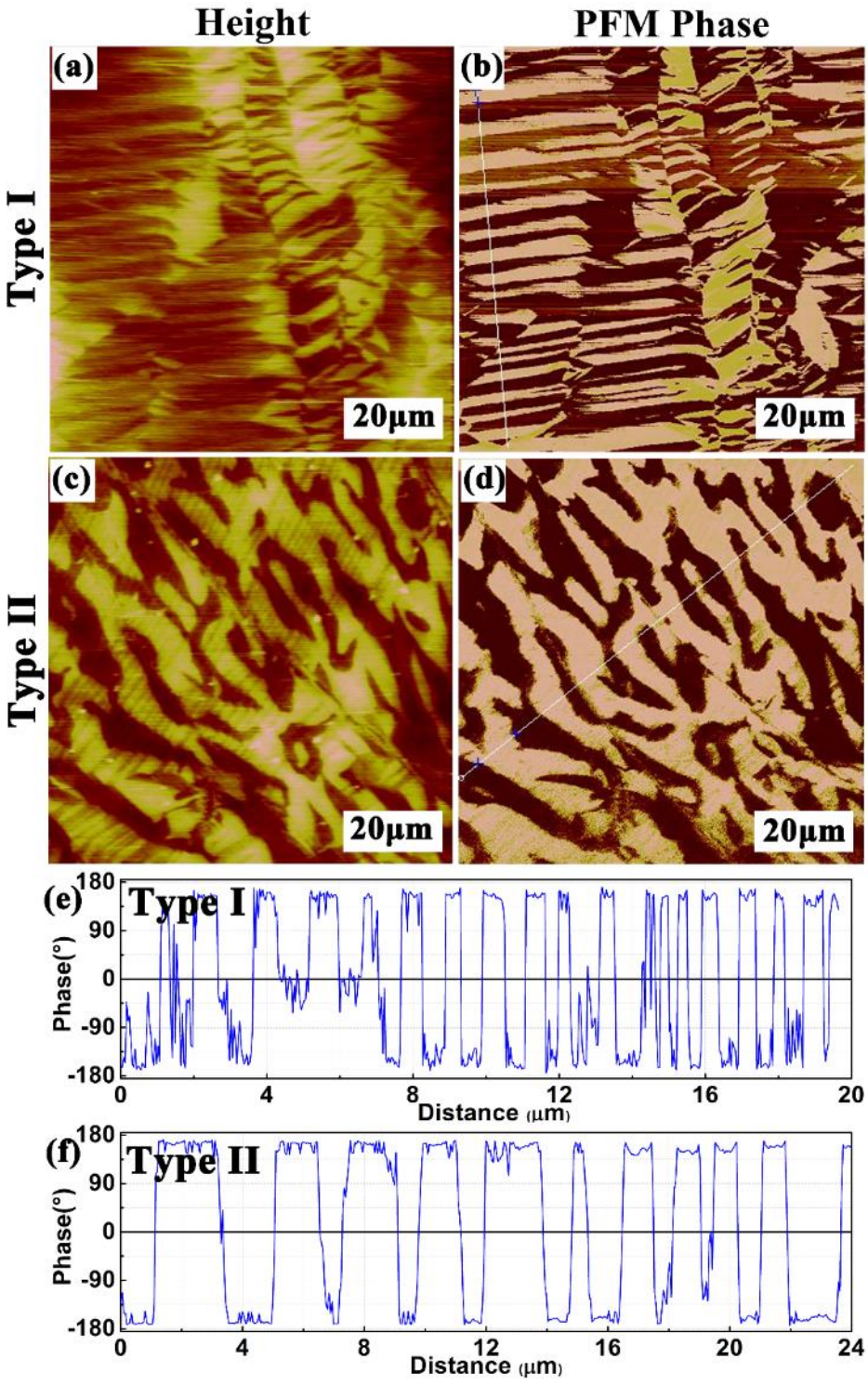

Figure 3.5. Topography height images and piezoresponse phase images as well as sectional analyses under piezoresponse force microscope (PFM) with 20 μm scan sizes for (011) PMN-30PT without an electrically induced O phase upon removal of E-field (panel (a) (b) (e)) and (011) PMN-30PT with a metastable O phase upon removal of poling electric field (panel (c) (d) (f)).

As shown in Fig.3.6 and Fig.3.7, we also obtained finer scale PFM phase images taken at 10 μm sizes, which provide a clearer comparison. Figure 3.6 shows that the domains in type I crystals are highly regular and that the boundaries are nearly straight. This indicates a relatively defect-free condition in type I crystals, where domain boundary growth was unimpeded during the nucleation and growth process. Note that in the initial annealed state the structure of type I crystals was R, with little mixture of monoclinic (M) and orthorhombic (O) phases[96]. For type II crystals (Figure 3.7), the curved boundaries and highly irregular shapes are signs of domain roughening due to heterogeneities. These results indicate a tendency towards phase coexistence and/or a higher concentration of immobile defects that consequently pin the domain boundaries. They also imply that type I crystals have a single R phase field that possesses a less quenched disorder, and thus may require electric fields to maintain the induced monodomain O. In contrast, the initial R phase of type II crystals have higher degrees of phase coexistence and/or quenched disorder, thereby leading to more pinning sites that can metastably trap the O phase and impede recovery of its original polarization direction on removal of field.

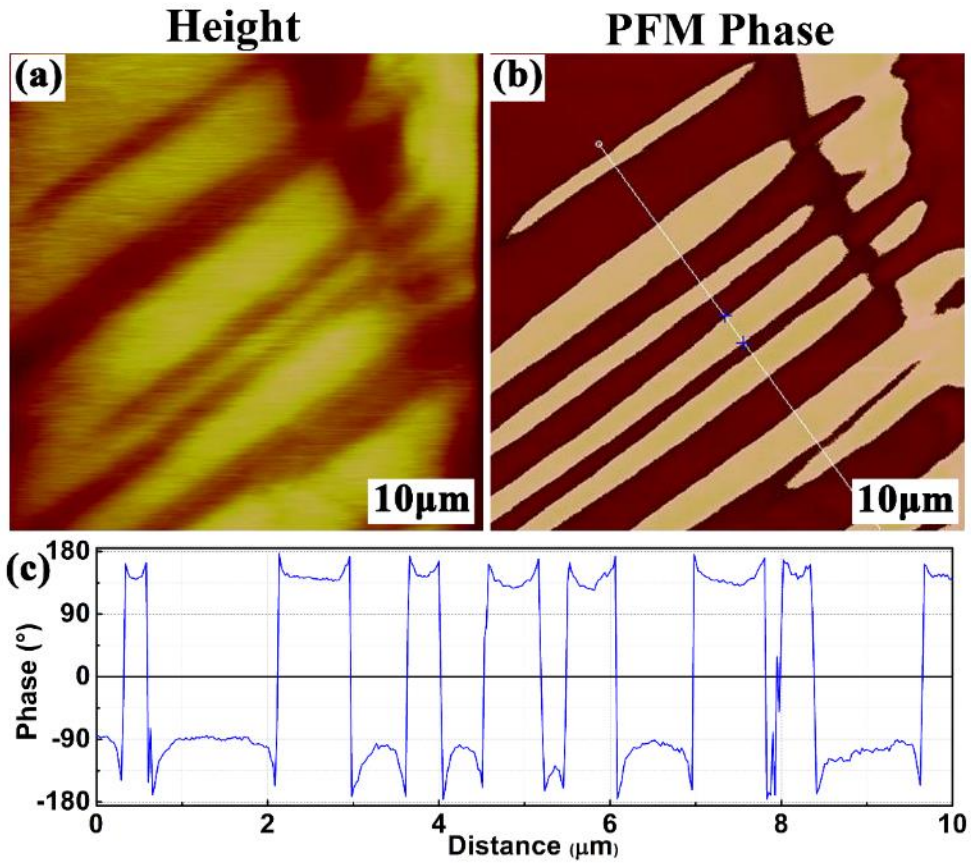

Figure 3.6. Height (a) and piezoresponse phase (b) images with 10 µm scan size for type I (011)-PMN-30PT and (c) sectional analysis of the phase changes indicated by the white line in panel (b).

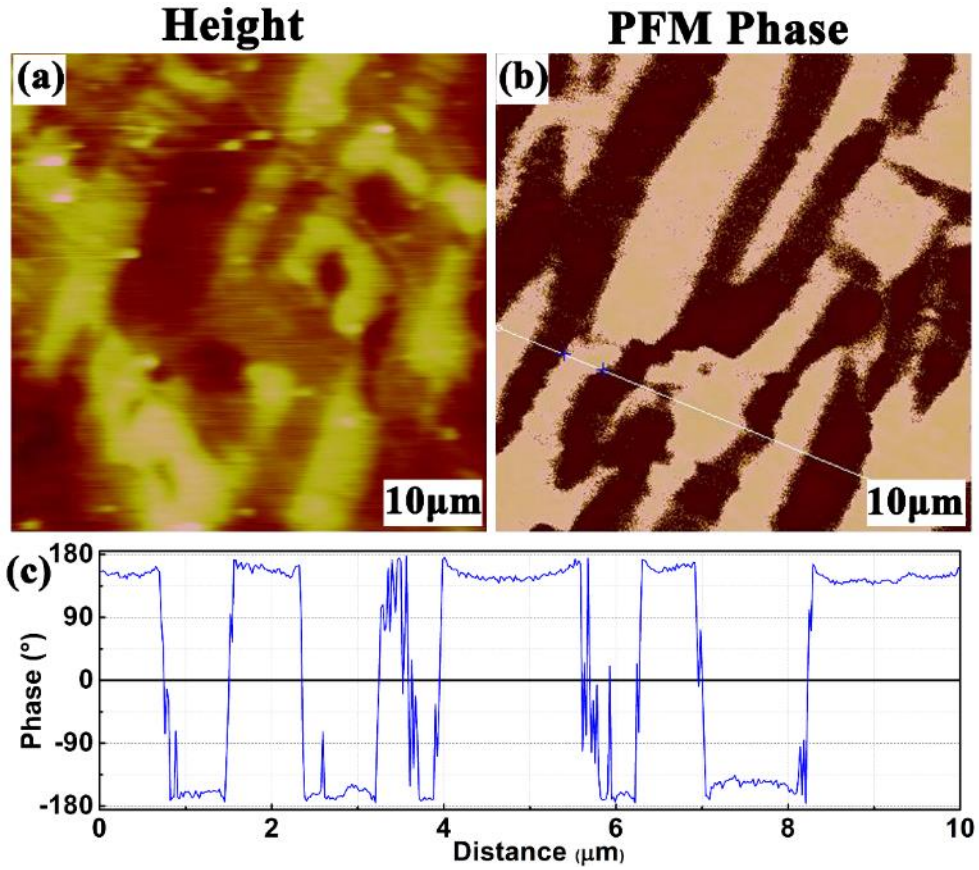

Figure 3.7. Height (a) and piezoresponse phase (b) images with 10 µm scan size for type II (011)-PMN-30PT and (c) sectional analysis of the phase changes indicated by the white line in panel (b).

In combination with the dielectric measurement results shown in Fig. 3.3—where type II crystals may have had a slightly higher $PbTiO_3$ (PT) content than type I crystals—the difference in average domain width revealed by the PFM images suggests that a higher Ti^{4+} content of B-site ions may lead to a higher tendency for colonies of polar nano-regions to assemble into larger microdomains. Research links this association to increased dipole-dipole interactions brought about by an increasing off-center displacement [104].

We then investigated the switching behavior of the two types of PMN-PT crystals by writing box-in-box patterns using opposite tip biases (Fig.3.8). First a +10V tip bias was applied to the central 2 μm squares, which poled the polarization vectors downwards. A -10V tip bias was subsequently applied to the central 1 μm squares to pole the polarization vectors upwards. Piezoresponse phase and amplitude images are shown in Fig.3.8 (a)-(b) and (c)-(d) for both types of crystals, respectively. It can be observed that both types of crystals are electrically switchable under an in-situ DC field of about ~ 0.75 kV/cm. Figures 3.8 (e) and (f) show sectional phase images demonstrating a complete domain switching induced by E, whereas panel (g)-(h) are sectional images of the amplitude channels, where domain walls can clearly be identified.

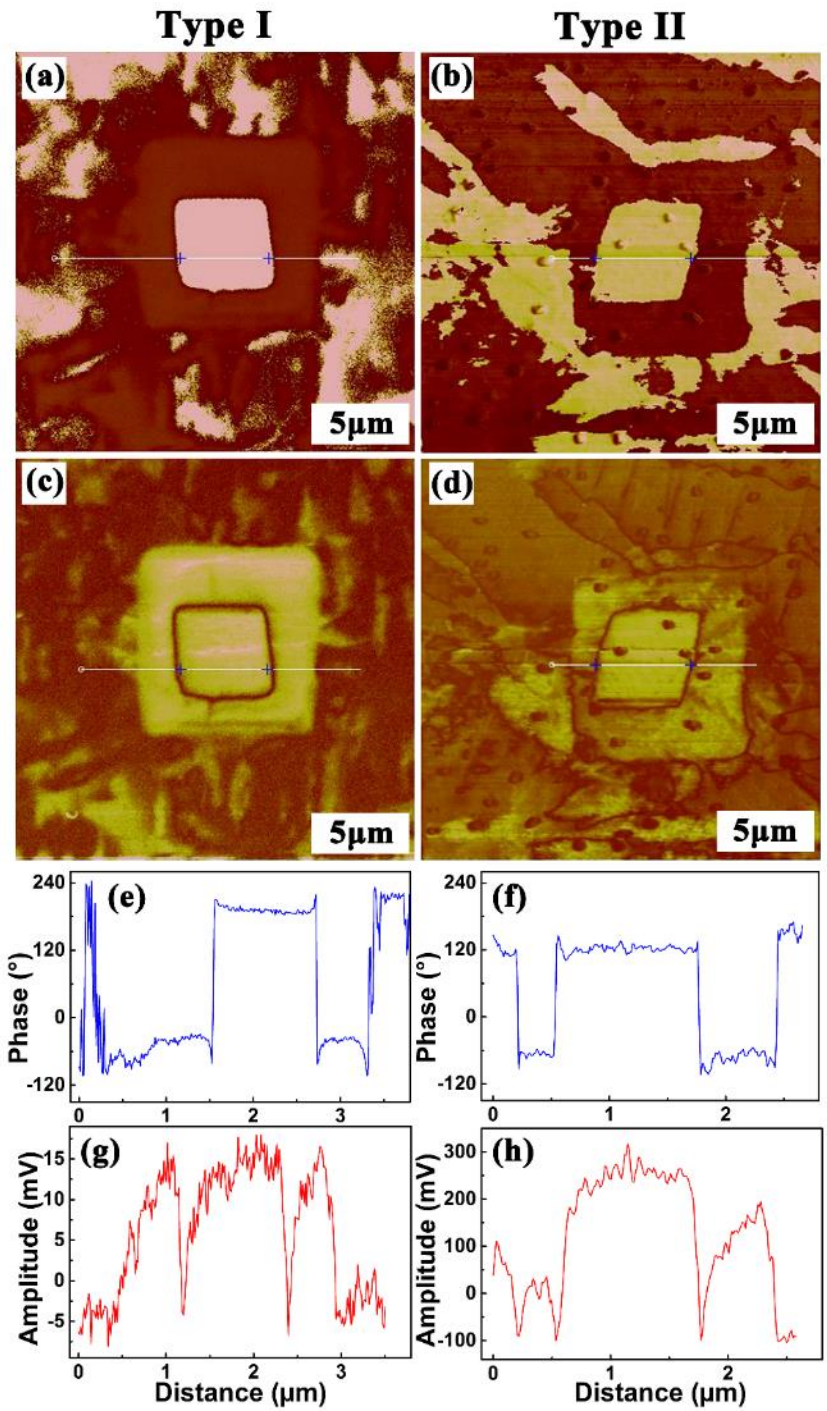

Figure 3.8. Piezoresponse phase (a) (b) and amplitude (c) (d) images with 5 µm scan size for two types of (011)-PMN-30PT showing box-in-box electric writing patterns, and (e) (f) sectional analysis of the phase changes as well as (g) (h) sectional analysis of the amplitude changes at switching boundaries.

3.5 Summary

In summary, macroscopic piezoelectric and dielectric measurements were combined with microscopic piezoresponse force microscopy mapping in order to investigate two types of (011)-oriented PMN-30%PT single crystals, which exhibited different electrically-induced phase transition sequences. In particular, both volatile and non-volatile orthorhombic (O) phases were studied upon removal of E. The temperature dependence of the relative permittivity indicated that crystals with non-volatile field-induced O phases had slightly higher PT contents. Piezoresponse force microscopy images revealed a microstructural origin of the changes between the volatile and non-volatile O phases. The domain configurations for the annealed crystals, whose induced O-phase was volatile, were of regular shape with straight and smooth walls. In contrast, the domain configurations for the induced O phase, which was non-volatile (metastable upon removal of E), displayed irregular shapes with wavy domain walls. The irregularities of the walls signal the presence of significantly higher degrees of heterogeneity that may metastably trap coexisting M_B and O phases. These results provide useful guidance in the understanding the behavior and optimal selection of PMN-x%PT crystals with regards to whether phase transition-induced strain is volatile or non-volatile. Such information is likely to be of importance for identifying suitable substrates for magnetoelectric heterostructures and future non-volatile electric-write magnetic-read storage devices.

CHAPTER 4: ELECTRIC-FIELD MANIPULATION OF MAGNETIZATION IN FERROMAGNETIC / FERROELECTRIC FE-GA/PMN-PT HETEROSTRUCTURES

4.1 Overview

Research in magnetoelectric thin-film heterostructures tends to focus on the strongly correlated ferromagnetic-ferroelectric system, in which the application of a voltage across the ferroelectric changes the properties of the adjacent ferromagnet (relevant examples are shown in Fig. 4.1 [105]). In particular, the magnetoelectric coupling in such structures can occur through three main mechanisms: (a) indirect coupling via strain, (b) electronic effects (a change in electronic structures of the ferromagnet by the polarization charge of the adjacent ferroelectric), and (c) exchange bias between a feromagnet and a multiferroic.

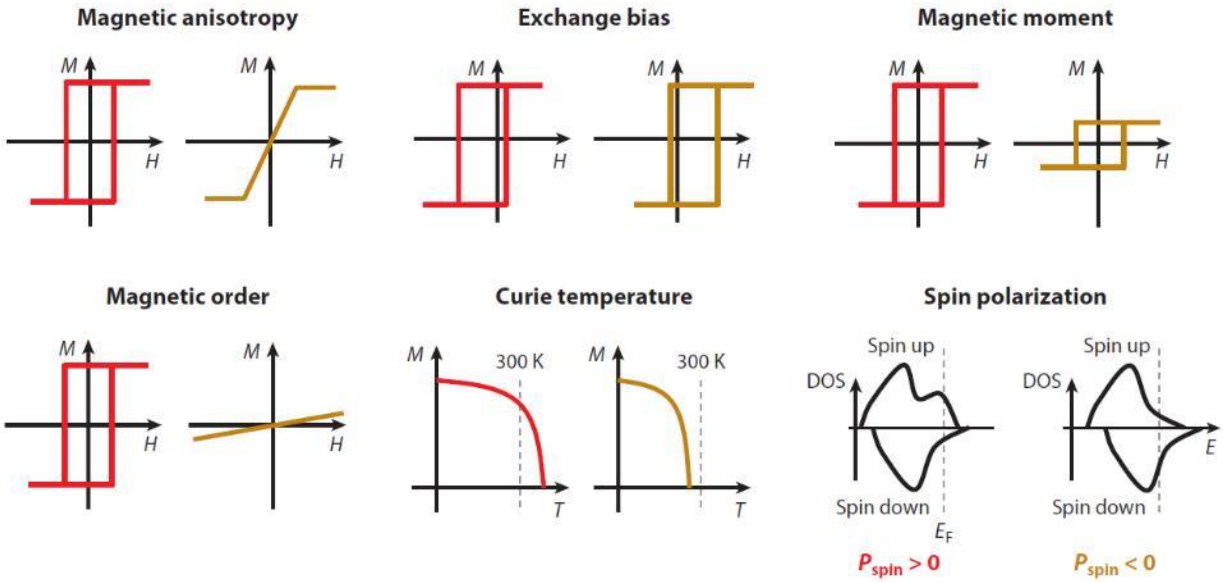

Figure 4.1. Different manifestation of electric controllable magnetic properties in ferromagnetic-ferroelectric heterostructures. ([105] Fusil, S.; Garcia, V.; Barthelemy, A.; Bibes, M., Magnetoelectric Devices for Spintronics. *Annual Review of Materials Research, Vol 44* 2014, *44*, 91-116.) Used under fair use, 2015.

Since strain engineering has proven to be a powerful and viable tool to tailor functionalities in oxides [33], a significant number of studies targeting magnetoelectric heterostructures have utilized interfacial strain to tune magnetic properties. For example, Eerenstein et al. reported the growth of epitaxial $La_{0.66}Sr_{0.33}MnO_3$ (LSMO) thin films on single crystal $BaTiO_3$ (BTO) substrates, in which they observed significant magnetization changes near the R → O phase transition [87]. Similarly, Yang et al. deposited epitaxial CFO thin films on PMN-PT substrates to study magnetization changes under different electric fields, whereby they observed a converse magnetoelectric coefficient of $3.2\times10^{-8}sm^{-1}$ [106]. Thiele et al. reported the growth of LSMO on a PMN-PT substrate and obtained a strain-mediated converse ME coefficient of $\sim6\times10^{-8}sm^{-1}$ [88]. Despite the various materials systems investigated, they all focused on the overall magnetization change or switching of magnetization induced by the electric field coupled strain or phase transition. In our investigation, ferromagnetic Fe-Ga films on ferroelectric PMN-PT single crystal substrates were fabricated by pulsed laser deposition, after which we studied the effects of electric field on the magnetic anisotropy of the ferromagnetic phase.

4.2 Growth and characterization of Fe-Ga/PMN-PT heterostructures

4.2.1 Sample preparation

To achieve significant coupling and efficient transfer of strain in the ME thin-film heterostructures, it is essential to choose a ferromagnetic phase with high magnetostriction and a ferroelectric substrate with high piezoelectricity. Accordingly, films of Fe-Ga with a 50 nm thickness were deposited on (011)-oriented PMN-

30%PT substrates with dimensions of $4\text{mm} \times 5.9\text{mm} \times 0.33\text{mm}$ by pulsed laser deposition (PLD) in an Ar atmosphere at room temperature. The base pressure was 2.5×10^{-5} Torr and the deposition pressure 4 mTorr.

4.2.2 Characterization

The crystal structures of the as-deposited Fe-Ga/PMN-PT heterostructures were characterized by a PANalytical X-ray diffractometer in 2θ-ω scan, and the morphology features were studied by transmission electron microscopy (JEOL 2100). Investigations of electric field manipulation of the magnetization for the Fe-Ga films were performed using a vibrating sample magnetometer (VSM, Lakeshore 7300) at room temperature.

Figure 4.2 shows a XRD 2θ-ω line scan of a Fe-Ga/PMN-PT heterostructure with obvious <110> peaks of the PMN-PT substrates. However, no apparent diffraction peak from the Fe-Ga film could be detected in the pattern. This indicates that the Fe-Ga film did not epitaxially grow on the PMN-PT substrate owing to the large lattice mismatch.

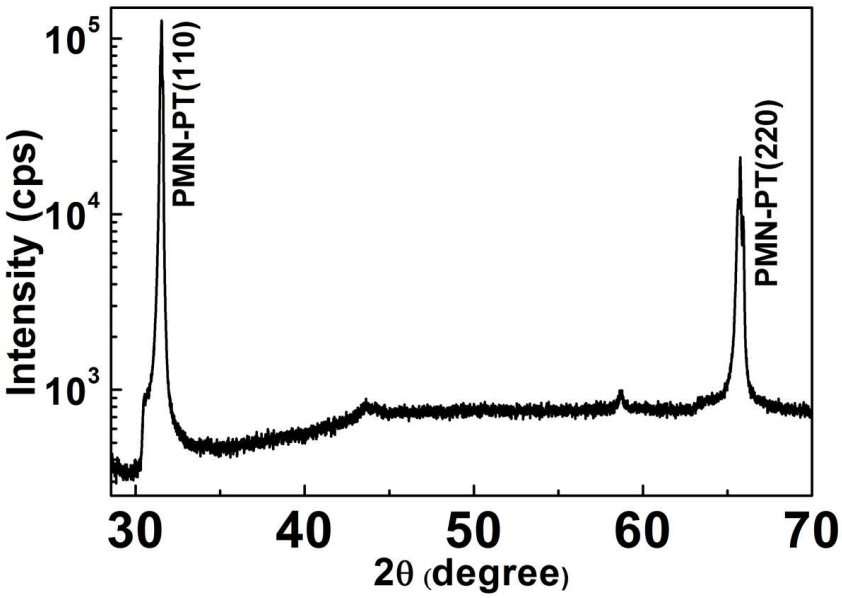

Figure 4.2. XRD 2θ-ω line scan of Fe-Ga/PMN-PT heterostructure.

To better understand the structure of the as-prepared Fe-Ga/PMN-PT heterostructures, TEM was used to obtain bright field images and selected area electron diffraction (SAED) patterns, as can be seen in Fig. 4.3. The bright field image in Part (a) confirmed that the as-deposited Fe-Ga films display a highly-organized columnar-like morphology with a diameter of ~5 nm. The higher magnification image shown in Part (b) revealed that the columns consist of many separate nanocrystals. By comparison, from the SAED patterns taken from regions of the ion-milled sample for both the Fe-Ga/PMN-PT heterostructure (Fig.4.3 (c)) and the Fe-Ga film (Fig.4.3 (d)), one observes that the lattice of the PMN-PT substrates affords strong peaks in the pattern, whereas the Fe-Ga film yields only weak diffraction rings. These data clearly demonstrate that the Fe-Ga film on the heterostructures have short-range nanocrystalline ordering in its microstructure. Additionally, the [111] diffraction rings of the Fe-Ga film coincided with the [200] diffraction peak of the PMN-PT substrate, allowing for coherent growth and interfacial matching. It is important to note that the lack of long-range crystalline order in the Fe-Ga film may be essential in promoting

the overall contribution of the magnetoelastic anisotropy to the total magnetic free energy over that of the magnetocrystalline anisotropy; in fact, for the latter the contribution should be negligible. In turn, this should enable large changes in the free energy by imposed elastic strain fields.

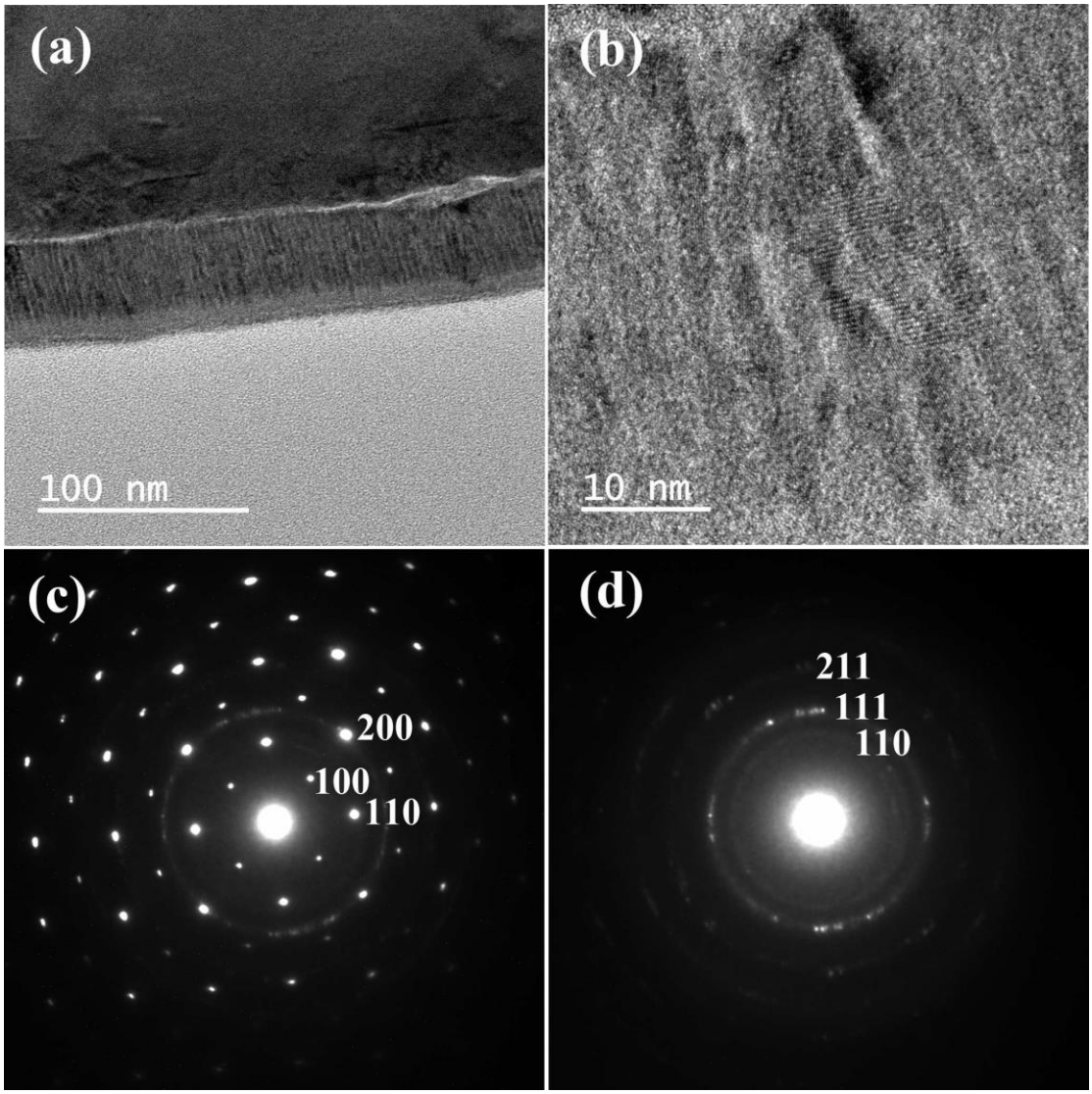

Figure 4.3. Transmission electron microscopy (TEM) images of the Fe-Ga/PMN-30PT heterostructure.(a)(b) bright field images with scale bars of 100nm and 10nm, respectively; (c) selected area electron diffraction (SAED) pattern for both Fe-Ga film and PMN-PT substrate; (d) SAED pattern for Fe-Ga film alone.

4.3 Electric field control of magnetization

4.3.1 Electric field control of magnetic remanence and coercivity

The changes in the magnetic responses of the as-deposited Fe-Ga film induced by an external applied electric field were investigated in-situ using a VSM. A DC electric field was applied along the [110] out-of-plane direction and the corresponding magnetic changes in the Fe-Ga film were measured using VSM. A schematic illustration of the crystallographic geometry of the heterostructure is given in Figure 4.4 (b). The orientation of the external magnetic field $\boldsymbol{H}$ and magnetization $\boldsymbol{M}$ is annotated in the diagram.

The magnetic hysteresis loops in Fig. 4.4 (a) provide a clear demonstration of the large shape anisotropy in the vertical direction versus the film plane. These measurements were obtained under a zero-electric field. The in-plane directions exhibited M-H hysteresis behaviors typical of that previously reported for bulk Fe-Ga alloys [57-61, 63]. However, the column arrays that stand in the out-of-plane direction resulted in this orientation being magnetically harder.

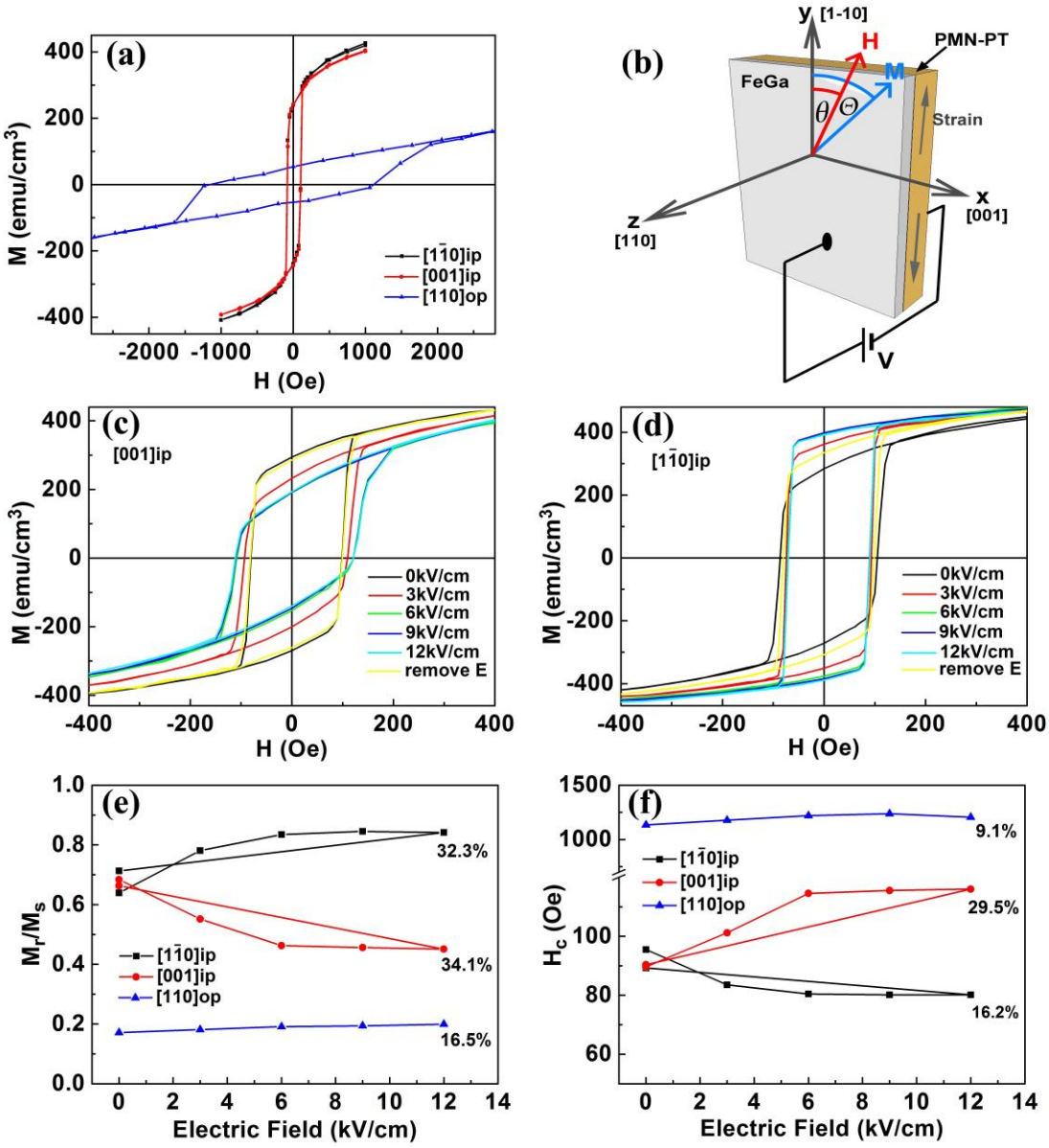

Figure 4.4. (a) Comparison of magnetic hysteresis loops obtained from [1$\bar{1}$0] in-plane, [001] in-plane, and [110] out-of-plane directions. (b) Schematic illustration of the Fe-Ga/PMN-PT heterostructure geometry and the measurement setup. (c) Magnetic hysteresis loops of Fe-Ga/PMN-PT with external magnetic field aligned along in-plane [001] direction. (d) Magnetic hysteresis loops of Fe-Ga/PMN-PT with external magnetic field aligned along in-plane [1 $\bar{1}$ 0] direction. (e) Squareness ratio (M_r/M_s) changes of Fe-Ga/PMN-PT with external electric field. (f) Coercive field changes of Fe-Ga/PMN-PT with external electric field.

The M-H loops in the in-plane [001], [$1\bar{1}0$] and out-of-plane, and [110] directions were all measured as a function of electric field, as shown in Fig. 4.4 (c) (d). These M-H loops were observed to exhibit considerable changes with $\boldsymbol{E}$ in both the remanence and coercivity along the in-plane [001] and [$1\bar{1}0$] directions, but hardly any changes were noted in the out-of-plane direction. With increasing $\boldsymbol{E}$, the remanent magnetization (M_r) of the Fe-Ga film in the [001] in-plane direction decreased notably, while its coercive field increased significantly, as seen in Fig. 4.4 (e) and (f). On the contrary, along the [$1\bar{1}0$] in-plane direction, M_r was greatly enhanced with increasing $\boldsymbol{E}$, while H_c was reduced. The change in H_c reached 29.5% along the [001] in-plane direction, which was notably larger than previously reported for either Ni/$BaTiO_3$(10%) [107] or Fe/$BaTiO_3$ samples (20%) [108].

Along the in-plane [001] direction, a maximum plateau in the squareness and coercive were found under electric fields of $8 \leq \boldsymbol{E} \leq 12$kV/cm. Interestingly, this corresponds to a significantly enhanced piezoelectric response of the PMN-30%PT substrate along [001], with a large transverse piezoelectric coefficient d_{31}. In the field range of $8 \leq \boldsymbol{E} \leq 12$kV/cm, a maximum in the piezoelectric coefficient occurred in PMN-30%PT due to a field-induced R→O phase transition. At lower $\boldsymbol{E}$, the strain varied linearly with electric field, and at higher fields, the strain state was constant. It is also interesting to note that the change in magnetization of the Fe-Ga film, particularly those in M_r/M_s and H_c, were reversible, exhibiting only small hysteresis effects (Fig. 4.4 (e) and (f)) transferred from those of the ε-E response of the PMN-PT substrate [109].

4.3.2 Electric field control of converse magnetoelectric coefficient

To further explore the electric field tunability of the magnetization of Fe-Ga films, the evolution of magnetization $\boldsymbol{M}$ was measured as a function of $\boldsymbol{E}$, and then normalized to its poled value $\boldsymbol{M_{pol}}$ at an applied poling electric field of 10kV/cm. The ferroelectric PMN-PT substrate was poled at 10 kV/cm before the measurements, and the magnetic field $\boldsymbol{H}$ applied along the [001] in-plane direction was kept constant during each measurement. When the electric field was reduced from 10 kV/cm to -1.8 kV/cm, the Fe-Ga film experienced a decreasing compressive strain due to inverse piezoelectric effects. This development led to a large change in the in-plane magnetic anisotropy, which altered the projection of $\boldsymbol{M}$ onto the direction of the external magnetic field. This change reached its saturation at -1.8 kV/cm. Upon further decrease of $\boldsymbol{E}$ to -10 kV/cm, the value of $\boldsymbol{M}$ returned to its value at E=10 kV/cm. Please note that the M-E curve exhibited a butterfly shape, rather than being bipolar. This demonstrates that an elastic strain-transferred coupling mechanism between the substrate and the film was responsible for the changes in $\boldsymbol{M}$. The maximum magnetization change with $\boldsymbol{E}$ can be seen in Fig. 4.5 (b), which reached 46% for $\boldsymbol{H}$=0 Oe. These data demonstrate a highly-efficient and deterministic E-control magnetization process. Additionally, a dramatic decrease of $\boldsymbol{E}$-induced magnetization change was found with increasing $\boldsymbol{H}$, which is due to the Fe-Ga film being saturated for $\boldsymbol{H}$>500 Oe.

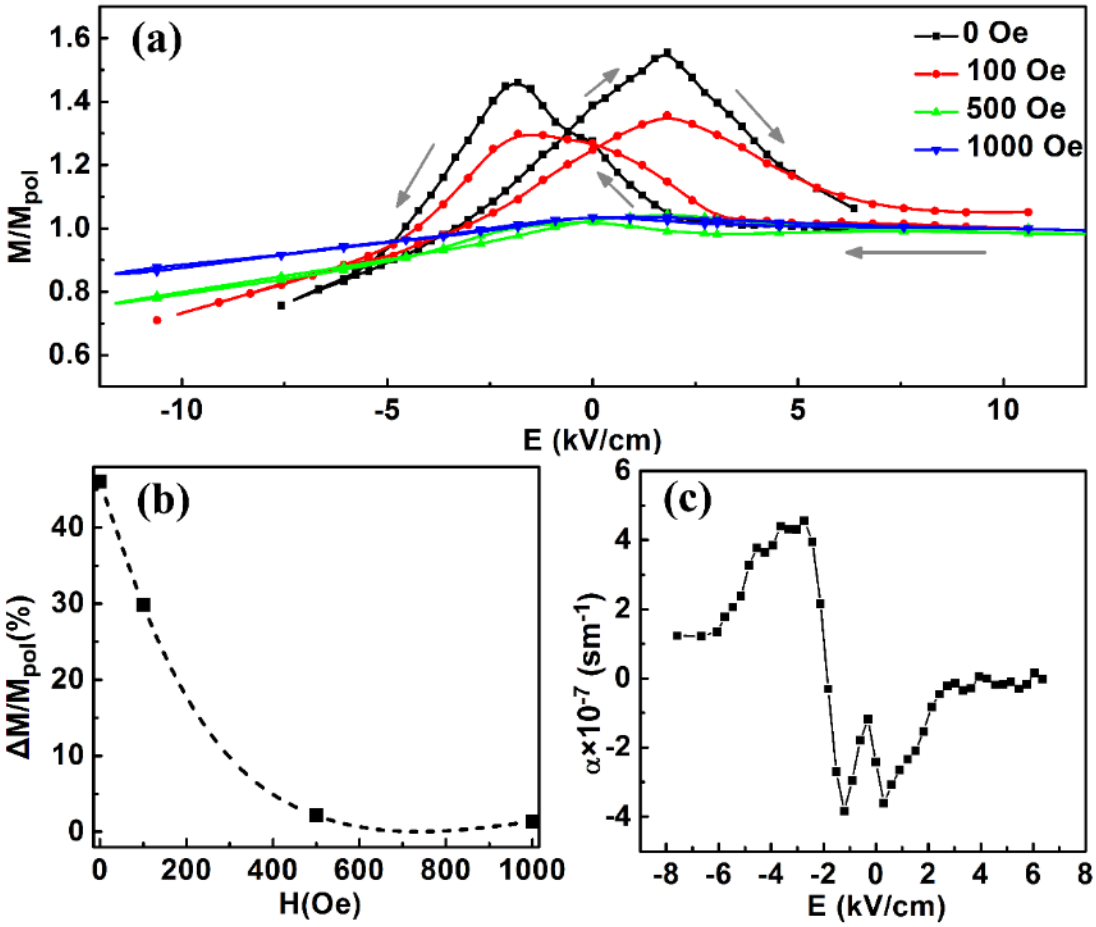

Figure 4.5. (a) Magnetization *M* of Fe-Ga with respect to different electric field *E* applied across PMN-PT substrate (*M* is normalized to the value M_{pol} at E=10 kV/cm). (b) Maximum magnetization change with *E* as a dependent of *H*. (c) Magnetoelectric coupling coefficient obtained directly from (a) when *H*=0 Oe.

Figure 4.5 (c) shows the converse magnetoelectric coefficient, which was calculated from the M-E curve for $\boldsymbol{H}$=0 Oe (Fig. 4.5 (a)) by $\alpha = \mu_0 \Delta M/\Delta E$. The maximum value of the as-derived converse magnetoelectric coefficient was α=4.55$\times 10^{-7}$ sm^{-1} for E=-2.7 kV/cm, whose field is close to the polarization coercivity of the ferroelectric PMN-PT substrate[110]. The converse ME coefficient is highly comparable with the reported value of multiferroic $La_{0.67}Sr_{0.33}MnO_3/BaTiO_3$ heterostructures and other magnetostrictive/piezoelectric laminates [87-88, 106].

4.3.3 Electric field control of magnetization orientation

As shown in Fig. 4.6, measurements were also performed to determine the ***E*** field control of the ***M*** orientation. Before each experiment, the sample was poled under ***H***=-5000 Oe and ***E***=12 kV/cm, which prepared ***M*** into a single domain state. Since ***H*** was applied along the in-plane [001] direction (θ=90°), the measured value of ***M*** was the projection of its value onto the [001] direction (Θ=90°). Measurements were performed under ***E***=12 kV/cm, while ***H*** was increased from -5000 Oe to 100 Oe, which is close to, but still below, the coercive field of the M-H loop. During the ***H*** sweep, ***M*** remained in its initial orientation for most of the ***H*** field range, and only began rotating when ***H*** came near 0 Oe (see Fig.4.6 (a)). As ***H*** approached the maximum value applied in Fe-Ga (100 Oe), ***M*** had not been fully switched. Note at the starting point B_1 of Fig. 4.6 (b) that ***M*** remained negative while the magnetic field ***H*** was positive, indicating that ***M*** and ***H*** were antiparallel at this point. To demonstrate that ***M*** can be switched solely by changing ***E***, the following ***E*** sweep was performed under constant magnetic field ***H***=100 Oe: +12 (B_1) → -1.8 (B_2) → +12 (B_3) kV/cm, and a following sequence of +12 (B_3) → -1.8 (B_4) → +12 (B_5) kV/cm.

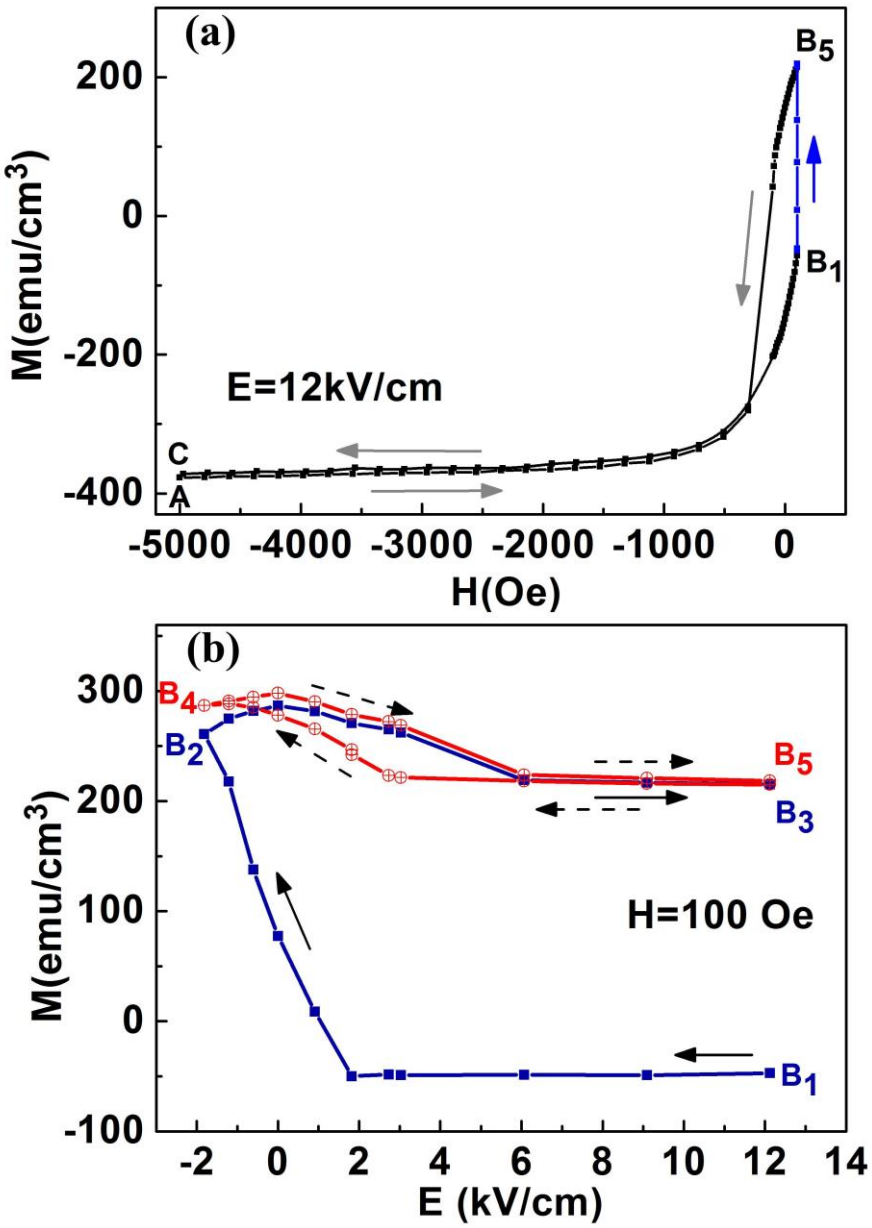

Figure 4.6. (a) The magnetization state of Fe-Ga/PMN-PT was prepared by settling electric field to 12 kV/cm and magnetic field to -5000 Oe (at point A); then the magnetic field *H* was increased from -5000 Oe to 100 Oe when *E* was kept constant at 12 kV/cm (at point B_1); (b) Magnetization manipulation by sweeping the electric field at constant *H*. By sweeping *E* at *H*=100 Oe from +12 kV/cm (B_1) → -1.8 kV/cm (B_2) → +12 kV/cm (B_3), the magnetization *M* was irreversibly changed (blue line). A second *E* cycle +12 kV/cm (B_3) → -1.8 kV/cm (B_4) → +12 kV/cm (B_5) only changed *M* reversibly (red line).

Upon decreasing ***E*** from 12 kV/cm (B_1) to -1.8 kV/cm (B_2), the orientation of ***M*** was completely switched, reaching a nearly demagnetized state (***M***=8.5879emu/cc) under ***E***=0.9 kV/cm, and changed sign with decreasing ***E*** to be parallel to that of the applied ***H***=100 Oe. On subsequent sweeping of ***E*** from -1.8 kV/cm (B_2) back to 12 kV/cm (B_3), ***M*** remained positive, and parallel to ***H***. A second scan of ***E*** from 12 kV/cm (B_3) to -1.8 kV/cm (B_4) and back (B_5) revealed a reversible change in ***M*** of only 38.6%, but no switch in its orientation. The small hysteresis in the second cycle corresponds to that in the $\boldsymbol{\varepsilon}$-***E*** loop of ferroelectric substrate. Clearly, a different evolution route of ***M*** was observed between these two ***E*** sweeps, from 12 to -1.8 kV/cm, where an irreversible ***M*** rotation occurred in the first cycle, but a reversible one occurred in the second cycle. This finding demonstrates that by sweeping only ***E*****,** ***M*** can be irreversibly switched. To restore the initial state of ***M***, ***H*** needed to be decreased to the original condition of -5000 Oe (see Fig.4.6 (a)), resulting in resetting the heterostructure back to point C from B_5. This pathway difference in magnetization changes can be understood by its magnetic free energy, and that the magnetization must be prepared in a local free-energy minimum to allow an irreversible rotation upon changing ***E*** [111].

Finally, ***M*** was manipulated with periodic electric-field pulses to gain some insights into its reversible responses between two well-defined states. Figure 4.7 shows that ***M*** can be switched between two well-defined electro-remanent states by applying an ***E*** field sequence of -0.9→0→0.9→0 kV/cm for ***H*** =0 Oe. These data show the ability to reversibly and rapidly tune the magnetization ***M*** of Fe-Ga by applying an appropriate electric field. Not only do these results extend our understanding of how to modulate

magnetization, they also point to significant applications potential—for example, as magnetoelectric read heads in memory devices.

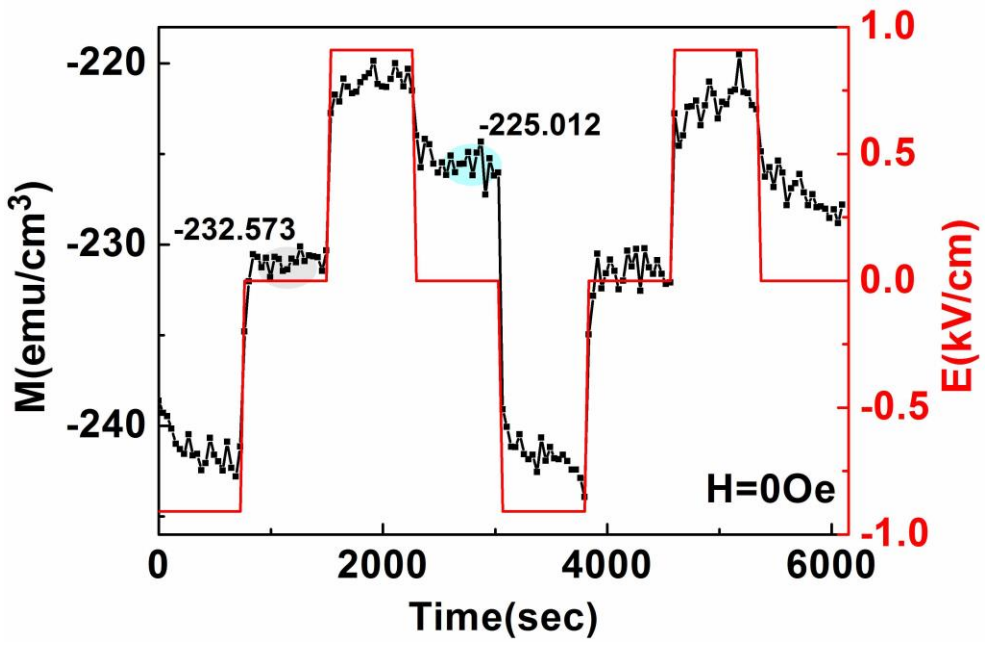

Figure 4.7. M sequence with periodically ramping electric field.

4.4 Mechanism of electric control of magnetization in Fe-Ga/PMN-PT

The origin of the electric tunability of magnetization in Fe-Ga film can be explained by considering the magnetic free energy density approach. Upon applying an electric field, the ferroelectric PMN-PT deforms and transfers a uniaxial in-plane strain to the ferromagnetic Fe-Ga film affixed to it. The PMN-PT expands along the in-plane [1$\bar{1}$0] direction (**y** axis) and contracts along the in-plane [001] direction (**x** axis) (see Fig.4.8). As a consequence, the Fe-Ga film is strained tensilely along **y** and compressively along **x**. The equilibrium state of the magnetization of Fe-Ga thin film is realized through the minimization of its magnetic total free energy. The total free energy of a ferromagnet in a magnetic field can be expressed as [112]:

$$F_{total} = F_H + F_D + F_K + F_\sigma + F_e$$

where each term above represents the Zeemann term (F_H), the demagnetization energy (F_D), the crystalline magnetic anisotropy energy (F_K), the magnetoelastic energy (F_σ) and exchange free energy (F_e).

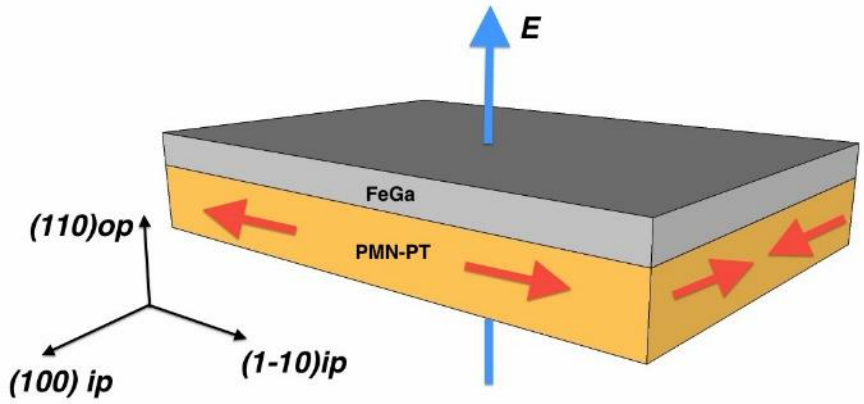

Figure 4.8. Schematic illustration of the crystallographic orientation and strain states in the Fe-Ga/PMN-PT heterostructures.

The exchange free energy, F_e, is related to the intrinsic crystal structure; however, methods for determining F_e are beyond the scope of this study. Also, the polycrystalline nature of Fe-Ga film, as previously described, shows no net crystalline magnetic anisotropy which may rival with the strain-induced anisotropy and thus can also be left out. Therefore, the total free energy would be:

$$F_{total} = F_H + F_D + F_\sigma$$

Zeeman term F_H is the energy of Fe-Ga's magnetization in the applied field H:

$$F_H = -\int M \cdot H dv$$

$$= -\mu_0 \mathrm{MH}(\sin\Theta\sin\Phi\sin\theta\sin\phi + \cos\Theta\cos\theta + \sin\Theta\cos\Phi\sin\theta\cos\phi)$$

The uniaxial demagnetization term $F_D = (\frac{\mu_0}{2})M^2 sin^2\Theta cos^2\Phi$ is related to the self-energy of the magnetization in its own field and is caused by the thin-film shape.

F_σ is the magnetostrictive energy (also referred to as magnetoelastic energy) caused by a stress σ acting on the ferromagnetic body. The contribution of magnetoelastic anisotropy is expressed as:

$$F_\sigma = B_1[\varepsilon_1\left(sin^2\Theta sin^2\Phi - \frac{1}{3}\right) + \varepsilon_2\left(cos^2\Theta - \frac{1}{3}\right) + \varepsilon_3\left(sin^2\Theta cos^2\Phi - \frac{1}{3}\right)]$$

where $B_1 = \frac{3}{2}\bar{\lambda}(c_{12}^{FeGa} - c_{11}^{FeGa})$ represents the magnetoelastic coupling coefficient; ε_1, ε_2, ε_3 correspond to the elastic strain along the x, y, z axis while shear strains are omitted due to their overall negligible effect on the polycrystalline film. $c_{11}^{FeGa} = 2.25 \times 10^{11} N/m^2$, $c_{12}^{FeGa} = 1.81 \times 10^{11} N/m^2$ are the elastic moduli of Fe-Ga (with 17 at% Ga) [113].

Substituting $sin^2\Theta sin^2\Phi + cos^2\Theta + sin^2\Theta cos^2\Phi = 1$ into the equation and omitting isotropic terms, the equation could be written as:

$$F_\sigma = K_u^{[1\bar{1}0]} cos^2\Theta + K_u^{[110]} sin^2\Theta cos^2\Phi$$

where $K_u^{[1\bar{1}0]}$, $K_u^{[110]}$ represent the uniaxial anisotropy contribution along $[1\bar{1}0]$ and $[110]$, respectively, and

$$K_u^{[1\bar{1}0]} = B_1(\varepsilon_2 - \varepsilon_1)$$

$$K_u^{[110]} = B_1(\varepsilon_3 - \varepsilon_1)$$

We use strain values of $\varepsilon_1 = -0.1875\%$, $\varepsilon_2 = 0.0375\%$, $\varepsilon_3 = 0.1625\%$.

$$\varepsilon_3 = -\frac{c_{12}^{FeGa}}{c_{11}^{FeGa}}(\varepsilon_1 + \varepsilon_2)$$

Here, I utilized the value $B_1 = -17 \times 10^6 \mathrm{J/m^2}$ [63] to calculate the angular dependence of magnetic anisotropy in FeGa film.

Consider the effects of strain on the magnetic anisotropy energy as described in the equations above. In the absence of an external magnetic field, the in-plane easy axis of F_{total} should orient parallel to tensile strains, and orthogonal to compressive strains, due to the negative sign of B_1.Upon application of an external electric field, the FeGa film experiences a tensile strain along the $[1\bar{1}0]$ direction (y axis) and a compressive strain along x ([001]) direction. Therefore, the easy axis would tend to align towards the y axis ($[1\bar{1}0]$ direction.

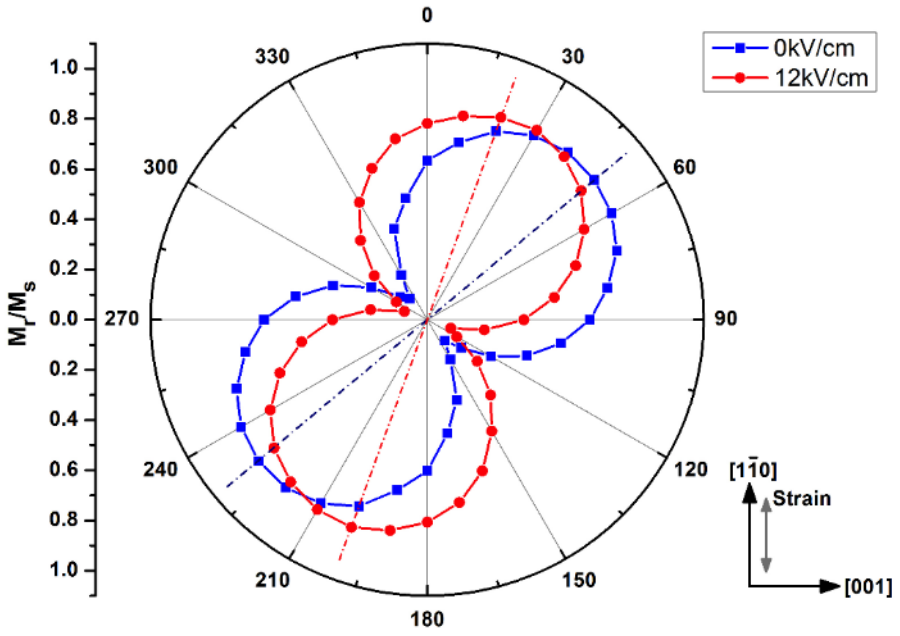

Figure 4.9. Angular dependence of squareness ratio Mr/Ms of the Fe-Ga films with no electric field (blue line) and 12kV/cm E-field (red line).

Figure 4.9 shows the angular dependence of the squareness ratio Mr/Ms with no electric field (blue line) and a 12kV/cm E-field (red line). With no E-field applied, ***M***

reached its maximum at 50 and 230 degrees, indicating a magnetic easy axis along that direction. Upon application of an electric field of 12 kV/cm, the in-plane magnetic easy axis rotated towards the [110]ip direction by 30 degree. Based on the equations and calculations above, it can be explained that the tensile strain along the [110]ip orientation induced by $\boldsymbol{E}$ changed the magnetoelastic anisotropy energy, thereby enabling the [110] direction to be a favorable direction for in-plane uniaxial magnetic anisotropy. These findings provide important insights into the evolution of $\boldsymbol{M}$ upon application of an external electric field, which can also shed light on the manipulation of magnetization by $\boldsymbol{E}$. Upon optimizing the film-growth process and strain-transfer efficiency, much larger magnetization rotation will be possible.

4.5 Summary

In summary, novel columnar-like Fe-Ga magnetostrictive layers on piezoelectric <110>PMN-30%PT substrate were grown and characterized. These columnar structured Fe-Ga films had droplet-shaped nanocrystalline regions. Films with this morphology exhibited large magnetic-shape anisotropy and a large converse magnetoelectric effect. It was shown that an electric field can be utilized to both irreversibly and reversibly modulate magnetization, opening up the potential for electric field-controlled magnetization devices.

CHAPTER 5: ELECTRIC-FIELD MANIPULATION OF MAGNETIZATION IN A SHEAR MODE CFO/PMN-PT HETEROSTRUCTURE

5.1 Introduction

The electric-field induced changes in magnetic properties is commonly known as the converse magnetoelectric effect. Research into two-phase ferromagnetic/piezoelectric composites is increasing in response to (a) their high magnetoelectric response, (b) their relatively uncomplicated electro-mechanical-magnetic coupling mechanisms, (c) their huge potential for the effective control of strain-sensitive order parameters, and (d) their promising applications in a wide spread of fields, including high density information storage, logic and spintronic devices. Various ferromagnetic thin films have been fabricated on piezoelectric single-crystal substrates using modern epitaxial techniques. Most of them utilized the high piezoelectric response of the substrates and the large magnetostriction of the ferromagnetic films—principally because the coupling between electric and magnetic orders in these heterostructures is achieved by interfacial strain mediation, through the combination of inverse piezoelectric effect and magnetostriction at the interface. In this regard, we selected ferromagnetic $CoFe_2O_4$ (CFO) due to its excellent magnetostrictive properties, and ferroelectric PMN-PT due to its piezoelectric responses. We then explored the interaction between the magnetic and electric orders in the individual phases.

5.2 Electric field control of magnetization in shear mode CFO/PMN-PT

It has been reported that ultrahigh shear piezoelectric coefficient (>4000 pC/N) exist in single-domain, relaxor-based crystals such as PMN-PT and PZN-PT [114-115].

Therefore, high quality $0.72Pb(Mg_{1/3}Nb_{2/3})O_3$-$0.28PbTiO_3$ (PMN-28PT) single crystals grown via a top-seeded modified Bridgman method were used as the shear-mode piezoelectric substrates [116]. The PMN-PT substrates were cut into $<111>_{cub} \times <1\bar{1}0>_{cub} \times <11\bar{2}>_{cub}$ platelets with dimensions of $5.5 \times 5 \times 0.5$ mm^3 to obtain a clear thickness shear response. Magnetostrictive CFO thin films were epitaxially grown via pulsed laser deposition (KrF excimer laser, λ=248nm) at 800℃ and 260 mJ for 30 min, with a base vacuum pressure of $\sim 10^{-6}$ Torr and oxygen pressure of 83 mTorr during deposition. The PMN-PT substrates were first poled along the spontaneous polarization directions of rhombohedral phase $<111>_{cub}$ to obtain a nearly single domain state, and then perpendicular electric-field along $<110>_{cub}$ was applied to trigger a thickness-shear piezoelectric response (d_{15}). This shear stress was directly transferred to the heteroepitaxial CFO films grown on the substrates via interfacial strain transfer and induced notable magnetization change in the ferromagnetic film.

The as-deposited films were ~200 nm in thickness as determined by cross-sectional scanning electron microscopy (SEM) measurements. The crystallographic structures of the as-deposited heterostructures were characterized using a high resolution PANalytical X-ray diffractometer (XRD) with an x-ray wavelength of Cu $K\alpha$ = 1.5406 Å. A Lakeshore 7300 series vibrating sample magnetometer (VSM) system was used to investigate the electric field tunability of magnetization for the CFO films at room temperature, with a Bertan high-voltage power supply (210-20R) attached to the samples as the external electric field source.

Figure 5.1 shows the crystal structure of the as-deposited CFO/PMN-PT heterostructures by an XRD line scan; while the insert shows a schematic illustration of the sample orientation. The two diffraction peaks can be assigned to CFO film and PMN-PT substrate, respectively, confirming that the film was epitaxially grown on the substrates with high crystallinity. The d-spacing of the CFO (422) plane and PMN-PT (211) plane was calculated to be (1.7139 Å, 1.6425Å) from the 2θ values of (53.4166°, 55.9344°), indicating a relatively large lattice mismatch of ~4.3% in the out-of-plane direction—and thus, theoretically a high level of strain in this architecture.

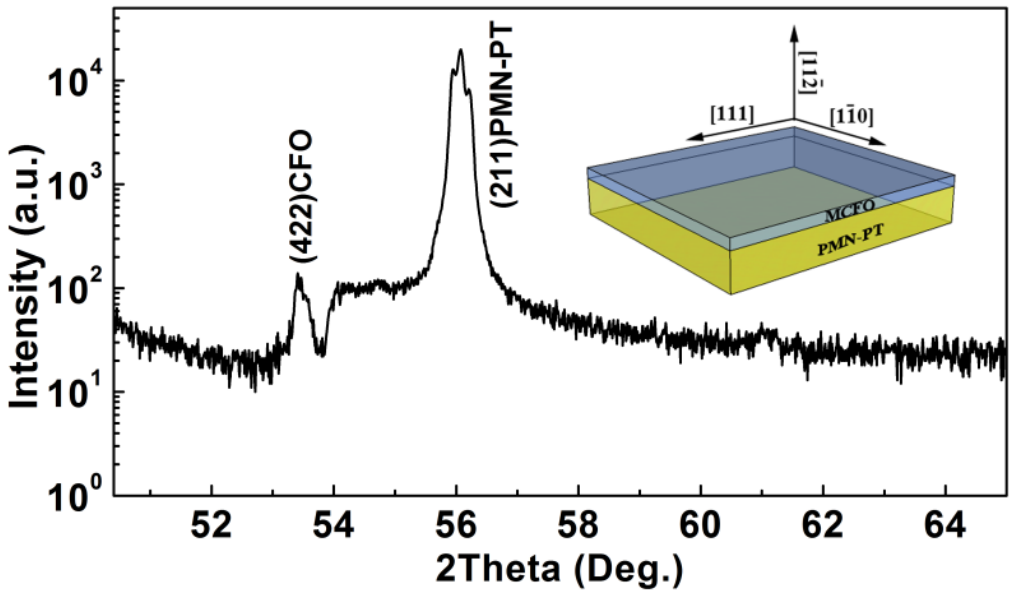

Figure 5.1. XRD line scan of the CFO/(112)PMN-PT heterostructures.

To achieve thickness shear mode (d_{15}) in the piezoelectric substrates, silver electrodes were first applied to the (111) faces and the samples were poled along the [111] direction in silica oil with a DC field of 4kV/cm at 125℃ for 20 min. After each poling, the longitudinal piezoelectric coefficient d_{33} was measured along [111] to

examine the validity of poling. Then, the silver electrodes were removed from the poled samples and were re-applied to the (110) faces. By applying DC electric field along the perpendicular [110] direction and then gradually increasing the field strength, d_{15} shear piezoelectric response was activated in the PMN-PT substrates. This polarization reorientation-induced shear stress was directly transferred to the heteroepitaxial CFO films. The crystal structure evolution of the PMN-PT substrates and the magnetic anisotropy changes of the CFO film were recorded during the process.

Figure 5.2 exhibits high-resolution x-ray diffraction peaks of the PMN-PT substrates before and after poling, as well as the evolution of crystal structure with increasing perpendicular field. The as-deposited CFO/PMN-PT heterostructures were in a depoled state due to the high deposition temperature, which was well above the ferroelectric Curie temperature (T_C) of PMN-PT. Thus, the polarizations in PMN-PT were distributed in all eight possible directions in the rhombohedral state (i.e. 8R), and appeared as a broad peak in the XRD pattern. After electric poling along their spontaneous polarization direction [111], the PMN-PT substrates experienced a polarization rotation process and changed to a nearly single domain state, i.e., 1R, as evidenced by the sharp narrow peak in the XRD scan in Figure 5.2. When applying a perpendicular E-field along [110], part of the polarization would rotate towards the external electric field, resulting in a multi-domain state. This trend was observed in the XRD pattern from the decrease of the peak at 55.9° and increase of the peak at 56°.

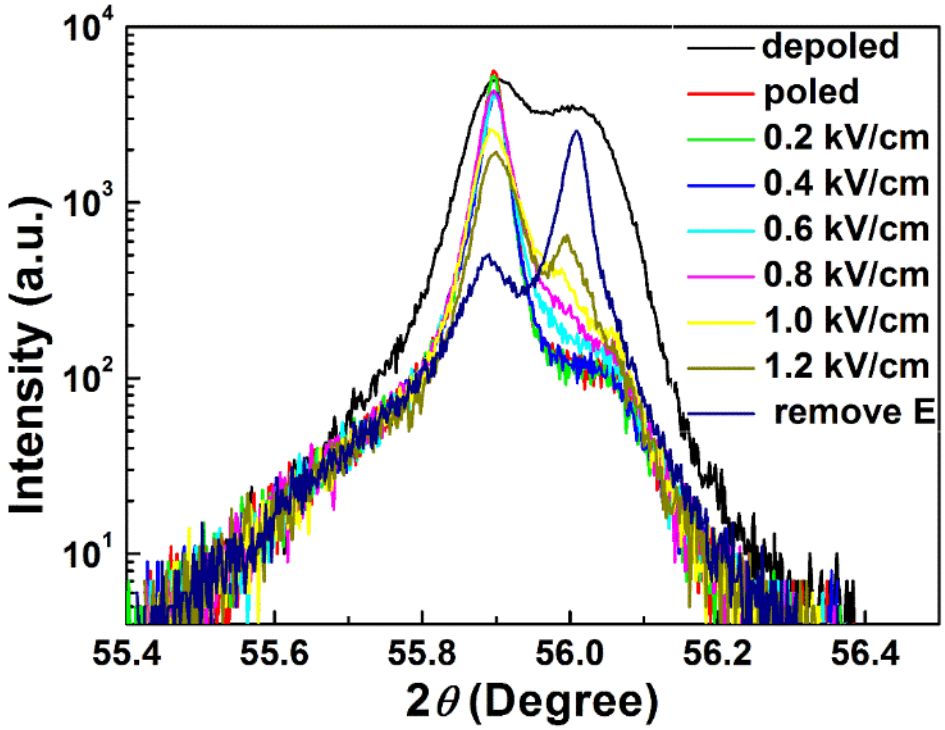

Figure 5.2. High-resolution XRD patterns of the (112) PMN-PT substrates before and after [111]-oriented poling, as well as their evolution with increasing perpendicular field along [110].

While the polarizations reoriented in the PMN-PT substrates, the induced shear stress acted directly on the CFO films on top, which tuned the magnetic anisotropy. Figure 5.3 demonstrates the original magnetic hysteresis loops measured along three perpendicular directions in the as-deposited samples. It is clear from this figure that the in-plane [111] direction is magnetically easier than the in-plane [110] direction, while the out-of-plane is the magnetic hard direction due to magnetic shape anisotropy energy caused by the small dimension of film thickness relative to the in-plane length and width.

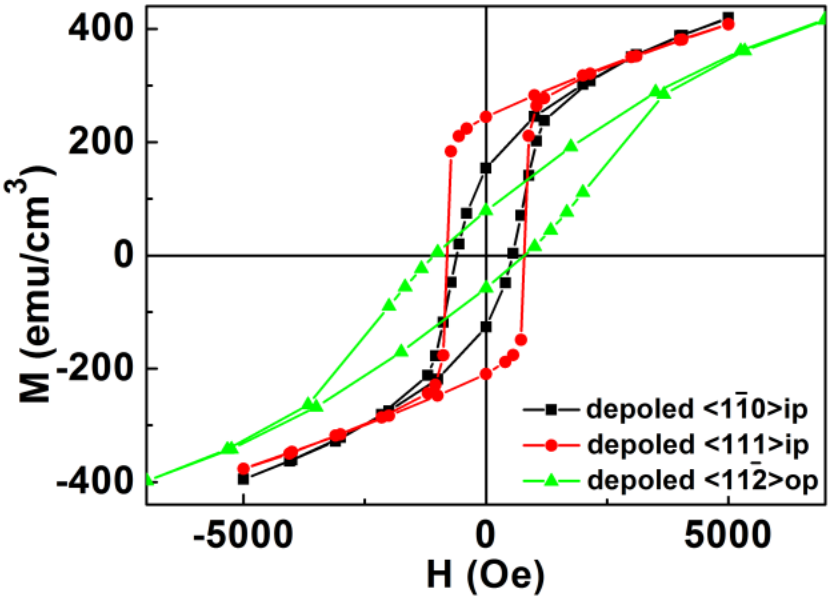

Figure 5.3. M-H loops of the as-deposited CFO/(112) PMN-PT sample in the depoled state. All three directions: in-plane [110], in-plane [111], and out-of-plane [112] were measured.

Figure 5.4 shows the electric field-dependence of magnetization in the CFO films when applying zero to 1.2 kV/cm E-field along the [110] direction, while the sample was poled along the [111] direction prior to measuring. With increasing electric field, the two in-plane directions ([110] and [111]) exhibited opposite trends in their changes of remanent magnetization and coercive field, as summarized in Fig.5.4 (c) and (d). Specifically, the magnetization squareness ratio M_r/M_s changed from 0.338 to 0.395 for the [110] in-plane direction when E-field increased from 0 to 1.2 kV/cm, and the magnetic coercive field H_c changed correspondingly from 732 Oe to 834 Oe (~14%), as shown by the red curves in Fig. 5.4 (c) and (d). This outcome corresponds to the electric field-induced shear stress transferred from the PMN-PT substrates to the CFO films, when the shear stress caused shrinkage along the [110] direction, and when CFO possessed a negative magnetostrictive coefficient along [110]. A similar,

but opposite, trend was observed for the in-plane [111] direction. The magnetization squareness ratio for the in-plane [111] direction dropped from 0.421 to 0.380 upon increasing E-field along [110], and the coercive field also experienced a decrease from 1065 Oe to 961 Oe (~9.7%). This change can be easily understood by the polarization rotation of the underlying PMN-PT substrates. The initially-established, nearly-single domain (1R) state by poling along the [111] direction was gradually destroyed during the increase of the perpendicular electric field along [110], causing a compressive deformation along [111], while at the same time the whole sample went through a shear distortion.

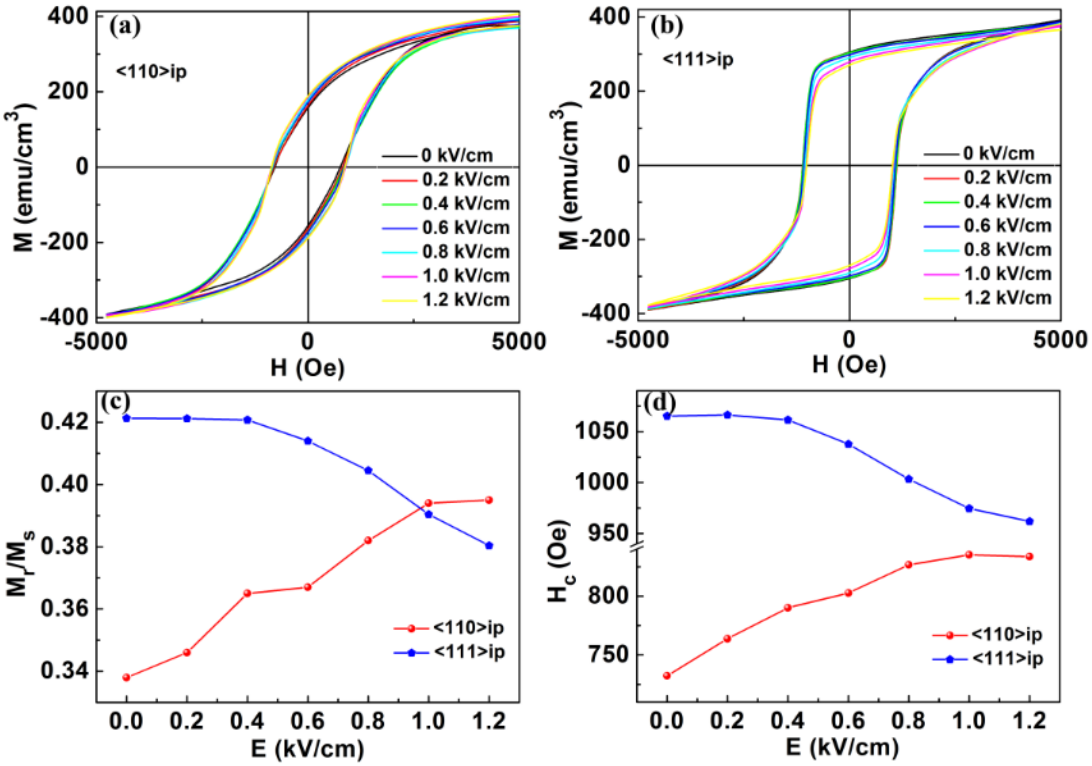

Figure 5.4. Electric field manipulation of magnetization in shear mode CFO/(112) PMN-PT when applying zero to 1.2 kV/cm E-field along the [110] direction after the sample had been poled along the [111] direction prior to measuring; (a) and (b) are M-H measurements along the [110] and [111] in-plane directions, respectively. (c) Magnetic squareness ratio (Mr/Ms) as a dependent of E-field for

the in-plane [110] and [111] directions. (d) Coercive field as a function of E-field for the in-plane [110] and [111] directions.

If one expects a reversible process, the perpendicular electric field along [110] should not exceed 1.0 kV/cm, as confirmed by the high resolution XRD scan of the PMN-PT substrates as a function of E-field. It should be noted that E>1.0 kV/cm will introduce irreversible polarization rotation in the PMN-PT substrates, thereby destroying the initial domain state. This can also be confirmed by the M-H loop measurements in that only E<1.0 kV/cm can give rise to a M-H loop that is similar to the initial one after removing the E-field.

5.3 Summary

This investigation confirmed the existence of the converse magnetoelectric effect in ferromagnetic CFO thin films grown on piezoelectric PMN-PT substrates with thickness-shear d_{15} cuts; related studies were undertaken on the electric-field dependence of magnetization change in the heterostructures. Rhombohedral phase $0.72Pb(Mg_{1/3}Nb_{2/3})O_3$-$0.28PbTiO_3$ single crystals oriented along $<111>^{l} \times <1\bar{1}0>^{w} \times <11\bar{2}>^{t}$ were used as substrates, and Mn-doped cobalt ferrite or $CoFe_2O_4$ (MCFO) thin films were epitaxially grown on the substrates by pulsed laser deposition (PLD). The PMN-PT substrates were first poled along the spontaneous polarization directions of rhombohedral phase $<111>_{cub}$ to obtain a nearly-single domain state, after which perpendicular electric-field along $<110>_{cub}$ was applied to trigger a thickness-shear piezoelectric response (d_{15}). This shear stress was directly transferred to the heteroepitaxial CFO films grown on the substrates via interfacial strain transfer and

induced magnetization change in the ferromagnetic film. The reason for the somewhat reduced changes in ferromagnetic properties (remanent magnetization, coercive field) in comparison to the Fe-Ga/(011) PMN-PT heterostructures could have resulted from the complex working mode and lower strain transfer efficiency of the shear-mode strain as opposed to the in-plane uniaxial strain. Therefore in order to obtain significant and applicable coupling effects for ferromagnetic-ferroelectric ME heterostructures, it is important to take into account several critical parameters, including constituent composition, microstructures, and working modes.

CHAPTER 6: SUMMARY

The heterostructures of magnetoelectric thin films and electric field manipulation of magnetization were investigated in great detail. Specifically, the ME coupling effect was achieved in different ferromagnetic-ferroelectric heterostructures through the use of interfacial strain mediation, and the E-field tuning of ferromagnetic properties was methodically explored.

Intriguing differences in the phase stabilities of PMN-PT crystals near the morphotropic phase boundary (MPB) were also thoroughly investigated. Results show that (011)-oriented PMN-PT crystals with compositions close to each other exhibited distinctive dielectric and piezoelectric behaviors due to different phase stabilities after E-field poling (i.e., $R \rightarrow M_B$ and $R \rightarrow M_B \rightarrow O$), where a metastable O-phase was observed in PMN-30%PT after E-field poling along [011]. The microstructural origins of these different behaviors were studied by PFM, after which correlations between the microstructures and macroscopic properties and phase transformations were proposed.

Converse magnetoelectric coupling was achieved in different ME thin film heterostructures, including Fe-Ga/(011) PMN-PT and CFO/(112) PMN-PT, and the E-field manipulation of ferromagnetic properties in these heterostructures was thoroughly studied. Our findings indicate that not only can an E-field effectively tune the magnetic remanence, coercive field, and ME coefficient of the Fe-Ga/PMN-PT heterostructures, it can also manipulate the magnetization directions of the Fe-Ga films. Moreover, ME coupling in CFO/(112) PMN-PT was achieved using a shear-strain mode in the PMN-PT substrates. Despite the fact that E-field control of

ferromagnetic properties was confirmed to some degree, the weaker controlling capability in this shear-mode heterostructure might be due to the complex working requirements of poling and subsequent perpendicular E-field—as well as to the less efficient transfer of shear strain between the ferromagnetic and ferroelectric phases.

In conclusion, the E-field manipulation of ferromagnetic properties in ME thin film heterostructures has opened up extraordinary research and applications opportunities—both in terms of elucidating its mechanisms and microstructure optimization, as well as in terms of the design of novel multifunctional devices. Our findings suggest that by selecting proper constituents (and their individual compositions), microstructure type, and electronic/magnetic properties, significant coupling between the phases can be realized. The results discussed herein have potential for the development of advanced industrial applications, including the field of sensors, microwave devices, and memory-related technologies.

PUBLICATIONS

- **Zhang, Y.**; Wang, Z.; Wang, Y.; Luo, C.; Li, J.; Viehland, D., Electric-field induced strain modulation of magnetization in Fe-Ga/Pb(Mg1/3Nb2/3)-PbTiO3 magnetoelectric heterostructures. Journal of Applied Physics, 2014, 115 (8).
- **Zhang, Y.**; Wang, Y.; Li, J.; Viehland, D., Domain configurations and phase transition sequence of (011)-oriented 0.7Pb(Mg1/3Nb2/3)O3-0.3PbTiO3 single crystals: volatile and non-volatile induced orthorhombic phases (to be submitted)
- Wang, Z.; **Zhang, Y.**; Viswan, R.; Li, Y.; Luo, H.; Li, J.; Viehland, D., Electrical and thermal control of magnetic coercive field in ferromagnetic/ferroelectric heterostructures. Physical Review B, 2014, 89 (3).
- Wang, Z.; **Zhang, Y.**; Wang, Y.; Li, Y.; Luo, H.; Li, J.; Viehland, D., Magnetoelectric Assisted 180° Magnetization Switching for Electric Field Addressable Writing in Magnetoresistive Random-Access Memory. ACS Nano, 2014, 8(8).

REFERENCES

1. Fiebig, M., Revival of the magnetoelectric effect. *Journal of Physics D: Applied Physics* **2005,** *38* (8), R123.
2. Spaldin, N. A.; Fiebig, M., The renaissance of magnetoelectric multiferroics. *Science* **2005,** *309* (5733), 391-392.
3. Schmid, H., Multi-ferroic magnetoelectrics. *Ferroelectrics* **1994,** *162* (1), 317-338.
4. Hill, N. A., Why are there so few magnetic ferroelectrics? *Journal of Physical Chemistry B* **2000,** *104* (29), 6694-6709.
5. Eerenstein, W.; Mathur, N. D.; Scott, J. F., Multiferroic and magnetoelectric materials. *Nature* **2006,** *442* (7104), 759-765.
6. Khomskii, D. I., Multiferroics: Different ways to combine magnetism and ferroelectricity. *Journal of Magnetism and Magnetic Materials* **2006,** *306* (1), 1-8.
7. Cheong, S.-W.; Mostovoy, M., Multiferroics: a magnetic twist for ferroelectricity. *Nature Materials* **2007,** *6* (1), 13-20.
8. Spaldin, N. A.; Cheong, S.-W.; Ramesh, R., Multiferroics: Past, present, and future. *Physics Today* **2010,** *63* (10), 38-43.
9. Curie, P., Sur la symétrie dans les phénomènes physiques. *Journal de Physique* **1894,** *3e Série* (3), 393-416.
10. Dzyaloshinskii, I. E., On the magneto-electrical effects in antiferromagnetics. *Soviet Physics—JET* **1960,** *37*, 628-629.
11. Astrov, D. N., The magnetoelectric effect in antiferromagnets. *Soviet Physics—JETP* **1960,** *11*, 708-709.
12. Folen, V. J.; Rado, G. T.; Stalder, E. W., Anisotropy of the magnetoelectric effect in Cr2O3. *Physical Review Letters* **1961,** *6* (11), 607-608.
13. Ascher, E.; Rieder, H.; Schmid, H.; Stossel, H., Some Properties of Ferromagnetoelectric Nickel-Iodine Boracite, Ni3B7O13I. *Journal of Applied Physics* **1966,** *37* (3), 1404-1405.
14. Alshin, B. I.; Astrov, D. N.; Tishchenko, A. V.; Petrov, S. V., Magnetoelectric effect in BaCoF4. *JETP Lett.* **1970,** *12*, 142.

15. Fiebig, M., Revival of the magnetoelectric effect. *Journal of Physics D-Applied Physics* **2005,** *38* (8), R123-R152.

16. Wang, J.; Neaton, J. B.; Zheng, H.; Nagarajan, V.; Ogale, S. B.; Liu, B.; Viehland, D.; Vaithyanathan, V.; Schlom, D. G.; Waghmare, U. V.; Spaldin, N. A.; Rabe, K. M.; Wuttig, M.; Ramesh, R., Epitaxial BiFeO3 Multiferroic Thin Film Heterostructures. *Science* **2003,** *299* (5613), 1719-1722.

17. Kimura, T.; Goto, T.; Shintani, H.; Ishizaka, K.; Arima, T.; Tokura, Y., Magnetic control of ferroelectric polarization. *Nature* **2003,** *426* (6962), 55-58.

18. Lawes, G.; Srinivasan, G., Introduction to magnetoelectric coupling and multiferroic films. *Journal of Physics D-Applied Physics* **2011,** *44* (24).

19. Hans, S., Some symmetry aspects of ferroics and single phase multiferroics *. *Journal of Physics: Condensed Matter* **2008,** *20* (43), 434201.

20. Schmid, H., On a magnetoelectric classification of materials. *International Journal of Magnetism* **1973,** *4* (4), 337-361.

21. Akbashev, A. R.; Kaul, A. R., Structural and chemical aspects of the design of multiferroic materials. *Russian Chemical Reviews* **2011,** *80* (12), 1159-1177.

22. Ortega, N.; Kumar, A.; Scott, J. F.; Katiyar, R. S., Multifunctional Magnetoelectric Materials for Device Applications. *arXiv.org* **2014**.

23. Catalan, G.; Scott, J. F., Physics and Applications of Bismuth Ferrite. *Advanced Materials* **2009,** *21* (24), 2463-2485.

24. Roginskaya, Y. E.; Venevtsev, Y. N.; Zhdanov, G. S., New Magnetic Ferroelectrics. *Soviet Physics JETP* **1965,** *21*, 817-822.

25. Smolenskiĭ, G. A.; Chupis, I. E., Ferroelectromagnets. *Soviet Physics Uspekhi* **1982,** *25* (7), 475.

26. Hur, N.; Park, S.; Sharma, P. A.; Ahn, J. S.; Guha, S.; Cheong, S. W., Electric polarization reversal and memory in a multiferroic material induced by magnetic fields. *Nature* **2004,** *429* (6990), 392-395.

27. Malashevich, A.; Vanderbilt, D., First-principles theory of magnetically induced ferroelectricity in TbMnO3. *European Physical Journal B* **2009,** *71* (3), 345-348.

28. Wang, C.; Guo, G.-C.; He, L., Ferroelectricity driven by the noncentrosymmetric magnetic ordering in multiferroic TbMn2O5: A first- principles study. *Physical Review Letters* **2007,** *99* (17).

29. Blake, G. R.; Chapon, L. C.; Radaelli, P. G.; Park, S.; Hur, N.; Cheong, S. W.; Rodriguez-Carvajal, J., Spin structure and magnetic frustration in multiferroic RMn2O5 (R=Tb,Ho,Dy). *Physical Review B* **2005,** *71* (21), 9.

30. Van Aken, B. B.; Palstra, T. T. M.; Filippetti, A.; Spaldin, N. A., The origin of ferroelectricity in magnetoelectric YMnO3. *Nat Mater* **2004,** *3* (3), 164-170.

31. Choi, T.; Horibe, Y.; Yi, H. T.; Choi, Y. J.; Wu, W.; Cheong, S. W., Insulating interlocked ferroelectric and structural antiphase domain walls in multiferroic YMnO3. *Nat Mater* **2010,** *9* (3), 253-258.

32. Ederer, C.; Spaldin, N. A., Electric-field-switchable magnets: The case of BaNiF4. *Physical Review B* **2006,** *74* (2).

33. Schlom, D. G.; Chen, L.-Q.; Fennie, C. J.; Gopalan, V.; Muller, D. A.; Pan, X.; Ramesh, R.; Uecker, R., Elastic strain engineering of ferroic oxides. *MRS Bulletin* **2014,** *39* (02), 118-130.

34. Van Suchtelen, J., Product properties: a new application of composite materials. *Philips Res. Rep* **1972,** *27* (1), 28-37.

35. Nan, C.-W.; Bichurin, M. I.; Dong, S.; Viehland, D.; Srinivasan, G., Multiferroic magnetoelectric composites: Historical perspective, status, and future directions. *Journal of Applied Physics* **2008,** *103* (3).

36. Bichurin, M. I.; Petrov, V. M.; Kiliba, Y. V.; Srinivasan, G., Magnetic and magnetoelectric susceptibilities of a ferroelectric/ferromagnetic composite at microwave frequencies. *Physical Review B* **2002,** *66* (13), 134404.

37. Dong, S.; Zhai, J.; Bai, F.; Li, J. F.; Viehland, D., Push-pull mode magnetostrictive/piezoelectric laminate composite with an enhanced magnetoelectric voltage coefficient. *Appl. Phys. Lett.* **2005,** *87* (6), 062502.

38. Dong, S. X.; Li, J. F.; Viehland, D., A longitudinal-longitudinal mode TERFENOL-D/Pb($Mg_{1/3}Nb_{2/3}$)O_3-$PbTiO_3$ laminate composite. *Appl. Phys. Lett.* **2004,** *85* (22), 5305-5306.

39. Dong, S. X.; Cheng, J. R.; Li, J. F.; Viehland, D., Enhanced magnetoelectric effects in laminate composites of Terfenol-D/Pb(Zr,Ti)O_3 under resonant drive. *Appl. Phys. Lett.* **2003,** *83* (23), 4812-4814.

40. Dong, S. X.; Li, J. F.; Viehland, D., Ultrahigh magnetic field sensitivity in laminates of TERFENOL-D and $Pb(Mg_{1/3}Nb_{2/3})O_3$-$PbTiO_3$ crystals. *Appl. Phys. Lett.* **2003,** *83* (11), 2265-2267.

41. Srinivasan, G., Magnetoelectric Composites. In *Annual Review of Materials Research, Vol 40*, Clarke, D. R.; Ruhle, M.; Zok, F., Eds. 2010; Vol. 40, pp 153-178.

42. Ryu, J.; Priya, S.; Uchino, K.; Kim, H. E., Magnetoelectric effect in composites of magnetostrictive and piezoelectric materials. *Journal of Electroceramics* **2002,** *8* (2), 107-119.

43. Cai, N.; Nan, C. W.; Zhai, J. Y.; Lin, Y. H., Large high-frequency magnetoelectric response in laminated composites of piezoelectric ceramics, rare-earth iron alloys and polymer. *Applied Physics Letters* **2004,** *84* (18), 3516-3518.

44. Wang, Y.; Hu, J.; Lin, Y.; Nan, C.-W., Multiferroic magnetoelectric composite nanostructures. *Npg Asia Materials* **2010,** *2* (2), 61-68.

45. Shrout, T. R.; Fielding, J., *RELAXOR FERROELECTRIC MATERIALS*. 1990; p 711-720.

46. Park, S.-E.; Shrout, T. R., Ultrahigh strain and piezoelectric behavior in relaxor based ferroelectric single crystals. *Journal of Applied Physics* **1997,** *82* (4), 1804-1811.

47. Han, P. D.; Yan, W. L.; Tian, J.; Huang, X. L.; Pan, H. X., Cut directions for the optimization of piezoelectric coefficients of lead magnesium niobate-lead titanate ferroelectric crystals. *Applied Physics Letters* **2005,** *86* (5).

48. Park, S. E.; Shrout, T. R., Relaxor based ferroelectric single crystals for electro-mechanical actuators. *Materials Research Innovations* **1997,** *1* (1), 20-25.

49. Noheda, B.; Cox, D. E.; Shirane, G.; Gonzalo, J. A.; Cross, L. E.; Park, S. E., A monoclinic ferroelectric phase in the Pb(Zr[sub 1 - x]Ti[sub x])O[sub 3] solid solution. *Applied Physics Letters* **1999,** *74* (14), 2059-2061.

50. Noheda, B.; Cox, D. E., Bridging phases at the morphotropic boundaries of lead oxide solid solutions. *Phase Transitions* **2006,** *79* (1-2), 5-20.

51. Fu, H. X.; Cohen, R. E., Polarization rotation mechanism for ultrahigh electromechanical response in single-crystal piezoelectrics. *Nature* **2000,** *403* (6767), 281-283.

52. Viehland, D., Symmetry-adaptive ferroelectric mesostates in oriented Pb(BI1/3BII2/3)O-3-PbTiO3 crystals. *Journal of Applied Physics* **2000,** *88* (8), 4794-4806.

53. Jin, Y. M.; Wang, Y. U.; Khachaturyan, A. G.; Li, J. F.; Viehland, D., Conformal miniaturization of domains with low domain-wall energy: Monoclinic ferroelectric states near the morphotropic phase boundaries. *Physical Review Letters* **2003,** *91* (19).

54. Spaldin, N. A., Analogies and differences between ferroelectrics and ferromagnets. *Physics of Ferroelectrics: A Modern Perspective* **2007,** *105*, 175-217.

55. Du Trémolet de Lacheisserie, E., *Magnetostriction : theory and applications of magnetoelasticity*. CRC Press: Boca Raton, 1993.

56. Cullity, B. D., *Introduction to magnetic materials*. Addison-Wesley Pub. Co.: Reading, Mass., 1972.

57. Dai, L. Y.; Cullen, J.; Wuttig, M.; Lograsso, T.; Quandt, E., Magnetism, elasticity, and magnetostriction of FeCoGa alloys. *Journal of Applied Physics* **2003,** *93* (10), 8627-8629.

58. Clark, A. E.; Hathaway, K. B.; Wun-Fogle, M.; Restorff, J. B.; Lograsso, T. A.; Keppens, V. M.; Petculescu, G.; Taylor, R. A., Extraordinary magnetoelasticity and lattice softening in bcc Fe-Ga alloys. *Journal of Applied Physics* **2003,** *93* (10), 8621-8623.

59. Srisukhumbowornchai, N.; Guruswamy, S., Large magnetostriction in directionally solidified FeGa and FeGaAl alloys. *Journal of Applied Physics* **2001,** *90* (11), 5680-5688.

60. Srisukhumbowornchai, N.; Guruswamy, S., Influence of ordering on the magnetostriction of Fe-27.5 at. % Ga alloys. *Journal of Applied Physics* **2002,** *92* (9), 5371-5379.

61. Wu, R. Q., Origin of large magnetostriction in FeGa alloys. *Journal of Applied Physics* **2002,** *91* (10), 7358-7360.

62. Kellogg, R. A. Development and Modeling of Iron-Gallium Alloys. PhD Thesis, Iowa State University, Ames, Iowa, 2003.

63. Clark, A. E.; Restorff, J. B.; Wun-Fogle, M.; Lograsso, T. A.; Schlagel, D. L., Magnetostrictive properties of body-centered cubic Fe-Ga and Fe-Ga-Al alloys. *Magnetics, IEEE Transactions on* **2000,** *36* (5), 3238-3240.

64. Tatsumoto, E.; Okamoto, T., Temperature Dependence of the Magnetostriction Constants in Iron and Silicon Iron. *Journal of the Physical Society of Japan* **1959,** *14* (11), 1588-1594.

65. Hunter, D.; Osborn, W.; Wang, K.; Kazantseva, N.; Hattrick-Simpers, J.; Suchoski, R.; Takahashi, R.; Young, M. L.; Mehta, A.; Bendersky, L. A.; Lofland, S. E.; Wuttig, M.; Takeuchi, I., Giant magnetostriction in annealed Co1-xFex thin-films. *Nature Communications* **2011,** *2*.

66. Ikeda, O.; Kainuma, R.; Ohnuma, I.; Fukamichi, K.; Ishida, K., Phase equilibria and stability of ordered b.c.c. phases in the Fe-rich portion of the Fe–Ga system. *Journal of Alloys and Compounds* **2002,** *347* (1–2), 198-205.

67. Slonczewski, J. C., Origin of Magnetic Anisotropy in Cobalt-Substituted Magnetite. *Physical Review* **1958,** *110* (6), 1341-1348.

68. Behera, C.; Choudhary, R. N. P.; Das, P., Size effect on electrical and magnetic properties of mechanically alloyed CoFe2O4 nanoferrite. *J Mater Sci: Mater Electron* **2015,** *26* (4), 2343-2356.

69. Zi, Z.; Sun, Y.; Zhu, X.; Yang, Z.; Dai, J.; Song, W., Synthesis and magnetic properties of CoFe2O4 ferrite nanoparticles. *Journal of Magnetism and Magnetic Materials* **2009,** *321* (9), 1251-1255.

70. Song, Q.; Zhang, Z. J., Shape control and associated magnetic properties of spinel cobalt ferrite nanocrystals. *Journal of the American Chemical Society* **2004,** *126* (19), 6164-6168.

71. Ai, L.; Jiang, J., Influence of annealing temperature on the formation, microstructure and magnetic properties of spinel nanocrystalline cobalt ferrites. *Curr. Appl. Phys.* **2010,** *10* (1), 284-288.

72. Chopdekar, R. V.; Suzuki, Y., Magnetoelectric coupling in epitaxial CoFe2O4 on BaTiO3. *Applied Physics Letters* **2006,** *89* (18).

73. Nlebedim, I. C.; Snyder, J. E.; Moses, A. J.; Jiles, D. C., Dependence of the magnetic and magnetoelastic properties of cobalt ferrite on processing parameters. *Journal of Magnetism and Magnetic Materials* **2010,** *322* (24), 3938-3942.

74. Giri, A. K.; Kirkpatrick, E. M.; Moongkhamklang, P.; Majetich, S. A.; Harris, V. G., Photomagnetism and structure in cobalt ferrite nanoparticles. *Applied Physics Letters* **2002,** *80* (13), 2341-2343.

75. Mooney, K. E.; Nelson, J. A.; Wagner, M. J., Superparamagnetic Cobalt Ferrite Nanocrystals Synthesized by Alkalide Reduction. *Chemistry of Materials* **2004,** *16* (16), 3155-3161.

76. Hu, J.-M.; Nan, C. W., Electric-field-induced magnetic easy-axis reorientation in ferromagnetic/ferroelectric layered heterostructures. *Phys. Rev. B* **2009,** *80* (22), 224416.

77. Committee, A. S. f. M. M. H., *Metals Handbook. - Vol. 8: Metallography, Structures and Phase Diagrams*. ASM: 1973.

78. Krebs, H.-U.; Weisheit, M.; Faupel, J.; Süske, E.; Scharf, T.; Fuhse, C.; Störmer, M.; Sturm, K.; Seibt, M.; Kijewski, H.; Nelke, D.; Panchenko, E.; Buback, M., Pulsed Laser Deposition (PLD) -- A Versatile Thin Film Technique. In *Advances in Solid State Physics*, Kramer, B., Ed. Springer Berlin Heidelberg: 2003; Vol. 43, pp 505-518.

79. Binnig, G.; Quate, C. F.; Gerber, C., Atomic Force Microscope. *Physical Review Letters* **1986,** *56* (9), 930-933.

80. Martin, Y.; Williams, C. C.; Wickramasinghe, H. K., Atomic force microscope‐force mapping and profiling on a sub 100 ‐ Å scale. *Journal of Applied Physics* **1987,** *61* (10), 4723-4729.

81. Foner, S., Versatile and Sensitive Vibrating ‐ Sample Magnetometer. *Review of Scientific Instruments* **1959,** *30* (7), 548-557.

82. Nan, T.; Liu, M.; Ren, W.; Ye, Z.-G.; Sun, N. X., Voltage Control of Metal-insulator Transition and Non-volatile Ferroelastic Switching of Resistance in VOx/PMN-PT Heterostructures. *Sci. Rep.* **2014,** *4*.

83. Phuoc, N. N.; Ong, C. K., Electric field modulation of ultra-high resonance frequency in obliquely deposited [Pb(Mg1/3Nb2/3)O3]0.68-[PbTiO3]0.32(011)/FeCoZr heterostructure for reconfigurable magnetoelectric microwave devices. *Applied Physics Letters* **2014,** *105* (2), -.

84. Dong, C.; Guo, D.; Wu, L.; Wang, F.; Jiang, C.; Jia, C.; Xue, D., Piezoelectric control of magnetic anisotropy in the Ni0.46Zn0.54Fe2O4/Pb(Mg1/3Nb2/3)O-3-PbTiO3 composite. *Applied Physics Letters* **2014,** *104* (6).

85. Wang, Z.; Zhang, Y.; Viswan, R.; Li, Y.; Luo, H.; Li, J.; Viehland, D., Electrical and thermal control of magnetic coercive field in ferromagnetic/ferroelectric heterostructures. *Physical Review B* **2014,** *89* (3).

86. Wang, Z.; Zhang, Y.; Wang, Y.; Li, Y.; Luo, H.; Li, J.; Viehland, D., Magnetoelectric Assisted 180° Magnetization Switching for Electric Field Addressable Writing in Magnetoresistive Random-Access Memory. *ACS Nano* **2014,** *8* (8).

87. Eerenstein, W.; Wiora, M.; Prieto, J. L.; Scott, J. F.; Mathur, N. D., Giant sharp and persistent converse magnetoelectric effects in multiferroic epitaxial heterostructures. *Nature Materials* **2007,** *6* (5), 348-351.

88. Thiele, C.; Doerr, K.; Bilani, O.; Roedel, J.; Schultz, L., Influence of strain on the magnetization and magnetoelectric effect in La(0.7)A(0.3)MnO(3)/PMN-PT(001) (A=Sr,Ca). *Physical Review B* **2007,** *75* (5).

89. Czeschka, F. D.; Geprägs, S.; Opel, M.; Goennenwein, S. T. B.; Gross, R., Giant magnetic anisotropy changes in Sr2CrReO6 thin films on BaTiO3. *Applied Physics Letters* **2009,** *95* (6), -.

90. Wu, T.; Bur, A.; Zhao, P.; Mohanchandra, K. P.; Wong, K.; Wang, K. L.; Lynch, C. S.; Carman, G. P., Giant electric-field-induced reversible and permanent magnetization reorientation on magnetoelectric Ni/(011) [Pb(Mg1/3Nb2/3)O3](1−x)–[PbTiO3]x heterostructure. *Applied Physics Letters* **2011,** *98* (1), -.

91. Zhang, Y.; Wang, Z.; Wang, Y.; Luo, C.; Li, J.; Viehland, D., Electric-field induced strain modulation of magnetization in Fe-Ga/Pb(Mg1/3Nb2/3)-PbTiO3 magnetoelectric heterostructures. *Journal of Applied Physics* **2014,** *115* (8), 084101.

92. Pertsev, N. A., Giant magnetoelectric effect via strain-induced spin reorientation transitions in ferromagnetic films. *Phys. Rev. B* **2008,** *78* (21), 212102.

93. Wu, T.; Bur, A.; Wong, K.; Hockel, J. L.; Hsu, C.-J.; Kim, H. K. D.; Wang, K. L.; Carman, G. P., Electric-poling-induced magnetic anisotropy and electric-field-

induced magnetization reorientation in magnetoelectric Ni/(011) $[Pb(Mg_{1/3}Nb_{2/3})O_3]_{(1-x)}$-$[PbTiO_3]_x$ heterostructure. *J. Appl. Phys.* **2011,** *109* (7), 07D732.

94. Thiele, C.; Dorr, K.; Fahler, S.; Schultz, L.; Meyer, D. C.; Levin, A. A.; Paufler, P., Voltage-controlled epitaxial strain in $La_{0.7}Sr_{0.3}MnO_3$/$Pb(Mg_{1/3}Nb_{2/3})O_3$-$PbTiO_3$(001) films. *Appl. Phys. Lett.* **2005,** *87* (26), 262502.
95. Wang, Z.; Wang, Y.; Ge, W.; Li, J.; Viehland, D., Volatile and nonvolatile magnetic easy-axis rotation in epitaxial ferromagnetic thin films on ferroelectric single crystal substrates. *Applied Physics Letters* **2013,** *103* (13), -.
96. Noheda, B.; Cox, D. E.; Shirane, G.; Gao, J.; Ye, Z. G., Phase diagram of the ferroelectric relaxor (1-x)PbMg1/3Nb2/3O3-xPbTiO3. *Physical Review B* **2002,** *66* (5).
97. Cao, H.; Li, J. F.; Viehland, D.; Xu, G. Y., Fragile phase stability in (1-x)PbMg1/3Nb2/3O3-xPbTiO3 crystals: A comparison of 001 and 110 field-cooled phase diagrams. *Physical Review B* **2006,** *73* (18).
98. Guo, Y.; Luo, H.; Chen, K.; Xu, H.; Zhang, X.; Yin, Z., Effect of composition and poling field on the properties and ferroelectric phase-stability of Pb(Mg1/3Nb2/3)O3–PbTiO3 crystals. *Journal of Applied Physics* **2002,** *92* (10), 6134-6138.
99. Viehland, D.; Li, J. F., Anhysteretic field-induced rhombhohedral to orthorhombic transformation in 〈110〉 -oriented 0.7Pb(Mg1/3Nb2/3)O3‐0.3PbTiO3 crystals. *Journal of Applied Physics* **2002,** *92* (12), 7690-7692.
100. Lu, Y.; Jeong, D. Y.; Cheng, Z. Y.; Zhang, Q. M.; Luo, H. S.; Yin, Z. W.; Viehland, D., Phase transitional behavior and piezoelectric properties of the orthorhombic phase of $Pb(Mg_{1/3}Nb_{2/3})O_3$-$PbTiO_3$ single crystals. *Applied Physics Letters* **2001,** *78* (20), 3109-3111.
101. Wang, Z.; Wang, Y.; Luo, H.; Li, J.; Viehland, D., Crafting the strain state in epitaxial thin films: A case study of CoFe2O4 films on Pb(Mg,Nb)O3-PbTiO3. *Physical Review B* **2014,** *90* (13), 134103.
102. Zhao, X.; Wang, J.; Chan, H. L. W.; Choy, C. L.; Luo, H., Effect of bias field on the dielectric properties of 0.7Pb(Mg1/3Nb2/3)O-3-0.3PbTiO(3) single crystals

with different orientations. *Applied Physics a-Materials Science & Processing* **2005,** *80* (3), 653-658.

103. Guo, Y. P.; Luo, H. S.; Ling, D.; Xu, H. Q.; He, T. H.; Yin, Z. W., The phase transition sequence and the location of the morphotropic phase boundary region in (1-x) Pb(Mg1/3Nb2/3)O-3 -xPbTiO(3) single crystal. *Journal of Physics-Condensed Matter* **2003,** *15* (2), L77-L82.

104. Shvartsman, V. V.; Kholkin, A. L., Domain structure of 0.8Pb(Mg1/3Nb2/3)O-3-0.2PbTiO(3) studied by piezoresponse force microscopy. *Physical Review B* **2004,** *69* (1).

105. Fusil, S.; Garcia, V.; Barthelemy, A.; Bibes, M., Magnetoelectric Devices for Spintronics. *Annual Review of Materials Research, Vol 44* **2014,** *44*, 91-116.

106. Yang, J. J.; Zhao, Y. G.; Tian, H. F.; Luo, L. B.; Zhang, H. Y.; He, Y. J.; Luo, H. S., Electric field manipulation of magnetization at room temperature in multiferroic $CoFe_2O_4$/$Pb(Mg_{1/3}Nb_{2/3})_{0.7}Ti_{0.3}O_3$ heterostructures. *Appl. Phys. Lett.* **2009,** *94* (21), 212504.

107. Gepraegs, S.; Brandlmaier, A.; Opel, M.; Gross, R.; Goennenwein, S. T. B., Electric field controlled manipulation of the magnetization in Ni/BaTiO3 hybrid structures. *Applied Physics Letters* **2010,** *96* (14).

108. Sahoo, S.; Polisetty, S.; Duan, C.-G.; Jaswal, S. S.; Tsymbal, E. Y.; Binek, C., Ferroelectric control of magnetism in BaTiO3/Fe heterostructures via interface strain coupling. *Physical Review B* **2007,** *76* (9).

109. Luo, L. H.; Wang, H. X.; Tang, Y. X.; Zhao, X. Y.; Feng, Z. Y.; Lin, D.; Luo, H. S., Ultrahigh transverse strain and piezoelectric behavior in (1-x)$Pb(Mg_{1/3}Nb_{2/3})O_3$-x$PbTiO_3$ crystals. *Journal of Applied Physics* **2006,** *99* (2), 024104.

110. Fitchorov, T.; Chen, Y.; Hu, B.; Gillette, S. M.; Geiler, A.; Vittoria, C.; Harris, V. G., Tunable fringe magnetic fields induced by converse magnetoelectric coupling in a FeGa/PMN-PT multiferroic heterostructure. *Journal of Applied Physics* **2011,** *110* (12).

111. Weiler, M.; Brandlmaier, A.; Gepraegs, S.; Althammer, M.; Opel, M.; Bihler, C.; Huebl, H.; Brandt, M. S.; Gross, R.; Goennenwein, S. T. B., Voltage controlled

inversion of magnetic anisotropy in a ferromagnetic thin film at room temperature. *New Journal of Physics* **2009,** *11*.

112. Morrish, A. H., *The physical principles of magnetism*. Wiley: 1965.

113. Kellogg, R. A.; Russell, A. M.; Lograsso, T. A.; Flatau, A. B.; Clark, A. E.; Wun-Fogle, M., Tensile properties of magnetostrictive iron–gallium alloys. *Acta Materialia* **2004,** *52* (17), 5043-5050.

114. Peng, J.; Chen, J. Z.; Lu, H. S.; He, T. H.; Xu, H. Q.; Lin, D., Shear-mode piezoelectric properties of 0.69Pb(Mg1/3Nb2/3)O-3-0.31PbTiO(3) single crystals. *Solid State Communications* **2004,** *130* (1-2), 53-57.

115. Li, F.; Zhang, S.; Xu, Z.; Wei, X.; Shrout, T. R., Critical Property in Relaxor-PbTiO3 Single Crystals - Shear Piezoelectric Response. *Advanced Functional Materials* **2011,** *21* (11), 2118-2128.

116. Luo, H. S.; Xu, G. S.; Xu, H. Q.; Wang, P. C.; Yin, Z. W., Compositional homogeneity and electrical properties of lead magnesium niobate titanate single crystals grown by a modified Bridgman technique. *Japanese Journal of Applied Physics Part 1-Regular Papers Short Notes & Review Papers* **2000,** *39* (9B), 5581-5585.